REPORT DOCUMENTATION PAGE

Form Approved
OMB No. 0704-0188

The public reporting burden for this collection of information is estimated to average 1 hour per response, including the time for reviewing instructions, searching existing data sources, gathering and maintaining the data needed, and completing and reviewing the collection of information. Send comments regarding this burden estimate or any other aspect of this collection of information, including suggestions for reducing the burden, to Department of Defense, Washington Headquarters Services, Directorate for Information Operations and Reports (0704-0188), 1215 Jefferson Davis Highway, Suite 1204, Arlington, VA 22202-4302. Respondents should be aware that notwithstanding any other provision of law, no person shall be subject to any penalty for failing to comply with a collection of information if it does not display a currently valid OMB control number.
PLEASE DO NOT RETURN YOUR FORM TO THE ABOVE ADDRESS.

1. REPORT DATE *(DD-MM-YYYY)*	2. REPORT TYPE	3. DATES COVERED *(From - To)*
24/May/2001	DISSERTATION	

4. TITLE AND SUBTITLE
AN IMPROVED STREAMLINE CURVATURE APPROACH FOR OFF DESIGN ANALYSIS OF TRANSONIC COMPRESSION SYSTEMS

5a. CONTRACT NUMBER

5b. GRANT NUMBER

5c. PROGRAM ELEMENT NUMBER

6. AUTHOR(S)
MAJ BOYER KEITH M

5d. PROJECT NUMBER

5e. TASK NUMBER

5f. WORK UNIT NUMBER

7. PERFORMING ORGANIZATION NAME(S) AND ADDRESS(ES)
VIRGINIA POLYTECHNICAL INSTITUTE

8. PERFORMING ORGANIZATION REPORT NUMBER
CI01-77

9. SPONSORING/MONITORING AGENCY NAME(S) AND ADDRESS(ES)
THE DEPARTMENT OF THE AIR FORCE
AFIT/CIA, BLDG 125
2950 P STREET
WPAFB OH 45433

10. SPONSOR/MONITOR'S ACRONYM(S)

11. SPONSOR/MONITOR'S REPORT NUMBER(S)

12. DISTRIBUTION/AVAILABILITY STATEMENT
Unlimited distribution
In Accordance With AFI 35-205/AFIT Sup 1

13. SUPPLEMENTARY NOTES

14. ABSTRACT

20010723 067

15. SUBJECT TERMS

16. SECURITY CLASSIFICATION OF:			17. LIMITATION OF ABSTRACT	18. NUMBER OF PAGES	19a. NAME OF RESPONSIBLE PERSON
a. REPORT	b. ABSTRACT	c. THIS PAGE		167	19b. TELEPHONE NUMBER *(Include area code)*

Standard Form 298 (Rev. 8/98)
Prescribed by ANSI Std. Z39.18

An Improved Streamline Curvature Approach for Off-Design Analysis of Transonic Compression Systems
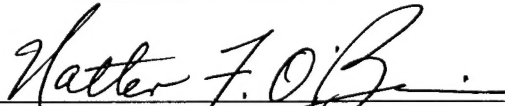
by

Keith M. Boyer

Dissertation submitted to the Faculty of the
Virginia Polytechnic Institute and State University
in partial fulfillment of the requirements for the Degree of
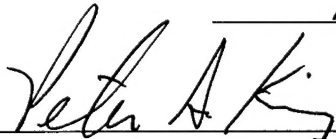
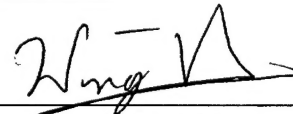**Doctor of Philosophy**

in

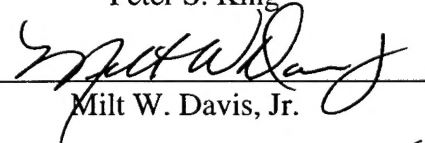**Mechanical Engineering**

Graduate Committee

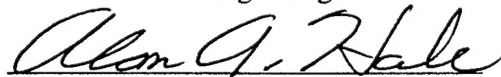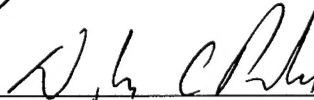Walter F. O'Brien, Chairman

Peter S. King

Wing F. Ng

Milt W. Davis, Jr.

Alan A. Hale

Douglas C. Rabe

9 April 2001

Blacksburg, Virginia

Keywords: Compressor, Fan, Transonic, Off-design, Streamline Curvature, Throughflow, Shock Loss, Distortion

An Improved Streamline Curvature Approach for Off-Design Analysis of Transonic Compression Systems

by

Keith M. Boyer

Committee Chairman: Walter F. O'Brien

Department of Mechanical Engineering

Abstract

A streamline curvature (SLC) throughflow numerical model was assessed and modified to better approximate the flow fields of highly transonic fans typical of military fighter applications. Specifically, improvements in total pressure loss modeling were implemented to ensure accurate and reliable off-design performance prediction. The assessment was made relative to the modeling of key transonic flow field phenomena, and provided the basis for improvements, central to which was the incorporation of a physics-based shock loss model. The new model accounts for shock geometry changes, with shock loss estimated as a function of inlet relative Mach number, blade section loading (flow turning), solidity, leading edge radius, and suction surface profile. Other improvements included incorporation of loading effects on the tip secondary loss model, use of radial blockage factors to model tip leakage effects, and an improved estimate of the blade section incidence at which minimum loss occurs.

Data from a single-stage, isolated rotor and a two-stage, advanced-design (low aspect ratio, high solidity) fan provided the basis for experimental comparisons. The two-stage fan was the primary vehicle used to verify the present work. Results from a three-dimensional, steady, Reynolds-averaged Navier-Stokes model of the first rotor of the two-stage fan were also used to compare with predicted performance from the improved SLC representation.

In general, the effects of important flow phenomena relative to off-design performance of the fan were adequately captured. These effects included shock loss, secondary flow, and spanwise mixing. Most notably, the importance of properly accounting for shock geometry and loss changes with operating conditions was clearly demonstrated. The majority of the increased total pressure loss with loading across the important first-stage tip region was shown to be the result of increased shock loss, even at part-speed. Overall and spanwise comparisons demonstrated that the improved model gives reasonable performance trends and generally accurate results, indicating that the physical understanding of the blade effects and the flow physics that underlie the loss model improvements are correct and realistic. The new model is unique in its treatment of shock losses, and is considered a significant improvement for fundamentally based, accurate throughflow numerical approximations.

The specific SLC model used here is employed in a novel numerical approach – the Turbine Engine Analysis Compressor Code (TEACC). With implementation of the improved SLC model and additional recommendations presented within this report, the TEACC method offers increased potential for accurate analysis of complex, engine-inlet integration issues, such as time-variant inlet distortion.

Dedication

This dissertation is dedicated to the three most important people in my life – my wife and two daughters. I met the former Joyce Marie Thibodeau in January 1982 while stationed at Loring AFB in Caribou, Maine. After a long courtship, we were married on September 3, 1982. She is truly the love-of-my-life and my soulmate. Jennifer Marie, born October 18, 1984, and Kelly Michelle, September 16, 1988, are our pride and joy. All three ladies have shown incredible dedication and support to me as they have endured several duty-related separations and the bulk of ten moves in my 22-year (and still going) Air Force career. Thank you all ladies. Next to the three of you, all my other accomplishments pale in comparison. I thank God daily for you.

Acknowledgements

"Never mistake knowledge for wisdom. One helps you make a living;
the other helps you make a life."
Carey

There are several people deserving acknowledgement for their help in the successful completion of this work. In addition to serving as advisors, all the members of my committee have been my mentors and role models. In my dealings with them, they have always treated me as a peer – for this, I am grateful. In particular, Walter O'Brien and Milt Davis are recognized for their advice and guidance in helping to shape my technical career over these past 14 years. Also, special thanks to Peter King. Since Peter was closest in proximity to me (within shouting distance), he was often my initial sounding board, providing sound and accurate advice.

The co-sponsors of this research deserve recognition. Doug Rabe of the Air Force Research Laboratory at Wright-Patterson Air Force Base (AFB), Ohio, and Jere Matty and Major Dan Benedict at the Arnold Engineering Development Center (AEDC), Tennessee, were especially helpful in securing funds to support research-related travel. Also, special thanks to Carl Williams, Doug and the Compressor Research Facility team for their support in providing and interpreting the data obtained from the two-stage fan used in this research. Thanks to General Electric Aircraft Engines for information pertaining to the design of the two-stage fan.

A special thanks to Chunill Hah of the NASA Glenn Research Center for providing the CFD results used in this work. Chunill was very receptive to the idea of including his results, and very responsive to all of my requests. The research is much more complete with the inclusion of the CFD solutions.

Many people at the AEDC deserve recognition. For two summers – 1999 and 2000 – I spent an extended time there at Arnold AFB in Tullahoma, Tennessee. I am very grateful to Milt

v

Table of Contents

List of Figures

ix

List of Tables

List of Symbols/Abbreviations

Symbol	Definition
3-D or 3D	three-dimensional
A^*	critical flow passage area
A_B	blade passage entrance area
A_J	blade passage exit area
a/c	blade/vane location of maximum camber
BC	boundary condition
c	blade/vane chord length
C_{ar}	constant in Equation (4-1)
CDA	controlled diffusion airfoil
CFD	computational fluid dynamics
CRF	Compressor Research Facility
D	diameter
DCA	double circular arc
deg	degrees
DNS	direct numerical simulation
e	specific total energy (internal and kinetic)
EGV	exit guide vanes
HCF	high cycle fatigue
ft	feet
i	incidence angle (degrees)
IGV	inlet guide vanes

in	inches
JSF	Joint Strike Fighter
k	turbulent kinetic energy
lbm	pound mass
LE	leading edge
LER	leading edge radius
LES	large eddy simulation
LSI	length-scale of interest
M	Mach number
m	meridional direction
$\dot{m}$	mass flow rate (lbm/s)
MA	isentropic Mach wave angle (degrees)
MCA	multiple circular arc
MLH	Miller, Lewis, and Hartmann
Nc	corrected speed
NC	near choke
NOL	nominal operating line
NS	near stall
P or p	static pressure
P_0, P_t, or PT	total pressure (psia)
PE	peak efficiency
PR	total pressure ratio
PS	pressure side (of blade)

psia	pounds per square inch absolute
R	Rankine
r or R	radius (inches) or radial direction
r_c	radius of curvature
R1	rotor one (of two-stage CRF fan)
R2	rotor two (of two-stage CRF fan)
RANS	Reynolds-averaged Navier-Stokes
Re	Reynolds number ($= V\ell/\nu$)
rev	revolution
rpm	rotations per minute
S_{Fx}, S_{Fy}, S_{Fz}	source term forces in x, y, z directions (Chapter 7)
S_m	source term bleed flow rate (Chapter 7)
S_{SW}	source term shaft work rate (Chapter 7)
s	blade/vane spacing or specific entropy
sec or s	seconds
S1	stator one (of two-stage CRF fan)
S2	stator two (of two-stage CRF fan)
SA	shock wave angle (degrees)
SAE	Society of Automotive Engineers
SLC	streamline curvature
SLCC	streamline curvature code
SS	suction side (of blade)
Stn	measurement station plane

T_0, T_t, or TT	total temperature
t/c	blade/vane thickness to chord ratio
TE	trailing edge
TEACC	turbine engine analysis compressor code
TLNS	thin-layer Navier-Stokes
TR	total temperature ratio
U	tangential velocity (ft/s)
u, v, w	x, y, z components of velocity (Chapter 7)
$\hat{u}$	specific internal energy
V	absolute velocity (ft/s)
V/STOL	vertical short take-off landing
W	relative velocity (ft/s) or loss bucket "width" (Equation A-11)
Wc	corrected mass flow rate (lbm/s)
WOD	wide-open discharge (= near choke)
x or z	axial direction (along compressor centerline)
x, y, z	Cartesian coordinates (Chapter 7)
x_o	location of shock vertex (Moeckel hyperbola)
Greek	**Definition**
α	absolute flow angle (degrees)
β or B	relative flow angle (degrees)
γ	ratio of specific heats or blade/vane stagger angle (degrees)
δ or d	deviation angle (degrees)
δ^*	boundary layer displacement thickness

ε	turbulent kinetic energy dissipation rate or wedge angle (degrees)
η	angle between sonic line and vertical (degrees)
θ	camber angle (degrees) or circumferential direction
κ	blade/vane metal angle (degrees)
λ	unblocked area parameter = 1-blockage (Appendix A)
μ	isentropic Mach wave angle (degrees)
ν	kinematic viscosity
ρ	density
σ	solidity (= chord/spacing)
φ	flow coefficient (= V_z/U) or streamline slope
ψ	shock wave angle (degrees) or loss coefficient
ω, ϖ, or w	average relative total pressure loss coefficient or rotational speed (rad/s)
Subscripts	**Definition**
1	upstream of blade row
1s	upstream of first passage shock
2	downstream of blade row
2s or B''	downstream of first passage shock
3	upstream of second passage shock positioned at trailing edge
add	additional
avg	average
bl	blade or boundary layer
blkg or bl	blockage factor (blocked area/cross-section area)
corr	corrected

elev	elevated
h	hub
i, e	inlet, exit control volume faces (Chapter 7)
l, r	left, right control volume faces (Chapter 7)
m	meridional
max	maximum
min or mn	minimum
m	Mach number
mod	modified (present modifications)
norm	normal
org	original (unmodified)
ref	low-speed reference condition
rel	relative
s	sonic point on Moeckel hyperbola
sb	sonic point on body (blade leading edge)
t, b	top, bottom control volume faces (Chapter 7)
tan	tangential
va	axial velocity ratio

1. Introduction/Motivation

1.1 Introduction

Accurate and robust turbomachinery off-design performance prediction remains elusive. Representation of transonic compression systems, most notably fans, is especially difficult, due in large part to highly three-dimensional blade design and the resulting flow field. Complex shock structure and subsequent interactions (with blade boundary layers, endwalls, etc.) provide additional complications.

Surely, turbomachinery design has benefited greatly from advancements in computational power and efficiency. In fact, in a 1999 "Special Issue on Turbomachinery Design," Journal of Mechanical Engineering Science, Denton and Dawes state: "Computational fluid dynamics (CFD) probably plays a greater part in the aerodynamic design of turbomachinery than it does in any other engineering application." However, practical limitations in terms of computational requirements, as well as limitations of turbulence and transition modeling, make it difficult to use CFD to analyze complex off-design issues. For example, CFD analyses have only recently been used to explore the complex flow fields resulting from inlet distortion through modern, multistage fans. The time-accurate investigation by Hah, et al., 1998, which included unsteady circumferential and radial variations of inlet total pressure, is one of the most complete in the open literature. Even so, Hah's calculation was limited to two blade passages with boundary conditions just upstream and downstream of the first rotor of a two-stage fan. In 1999, Rabe, et al., extended the analysis to the full annulus.

As discussed below, improvements to traditional numerical approaches are needed. The present work examines a proven engineering method, the streamline curvature throughflow approach, with the expressed purpose of improving its use relative to off-design, system analysis.

1

1.2 Motivation/Relevance

As noted recently by Denton and Dawes, 1999, and Adamczyk, 1999, throughflow methods, of which streamline curvature (SLC) is the dominant numerical approach, are the most important tool for turbomachinery design. Traditionally, the use of SLC is during the preliminary design phase (i.e., Jennions, 1994; discussed further in Section 2.1). While the primary emphasis of the present research is the development of a reliable and robust *off-design analysis* tool, the improved method could be applied to the more traditional design of a preliminary blade shape.

In general, the application of streamline curvature to transonic fans has been limited. The SLC methods do *not* typically include accurate fundamentally based off-design loss (and deviation) models (Bloch, et al., 1996). The present work seeks to provide an improved throughflow numerical approach specifically for the design and analysis of *modern fan systems*. Additionally, the choice of the specific SLC solver used here was based on its use in a novel numerical approach developed to investigate the issues discussed below.

Figure 1 - 1 demonstrates the changes in fan design philosophy driven by the need for increased pressure rise in fewer stages. Note the significant radial variation evident in the F119 fan flowpath (Figure 1 - 1a) relative to the TF30 (Figure 1 - 1b) used by Mazzawy and Banks, 1976, 1977 in their numerical distortion studies. Highly three-dimensional flows through low aspect ratio (span/chord), high solidity (chord/spacing) blading are characteristic of modern military fan designs.

Recent developments, motivated primarily by fighter/bomber applications, have stimulated interest in reexamining the procedures currently used to assess engine-inlet integration, most notably related to inlet distortion. Current procedures are largely based on

2

Note differences in　　a.　F119-PW-100 Turbofan
fan sections

b.　TF30-P-3 Turbofan (from Mazzawy and Banks, 1976)
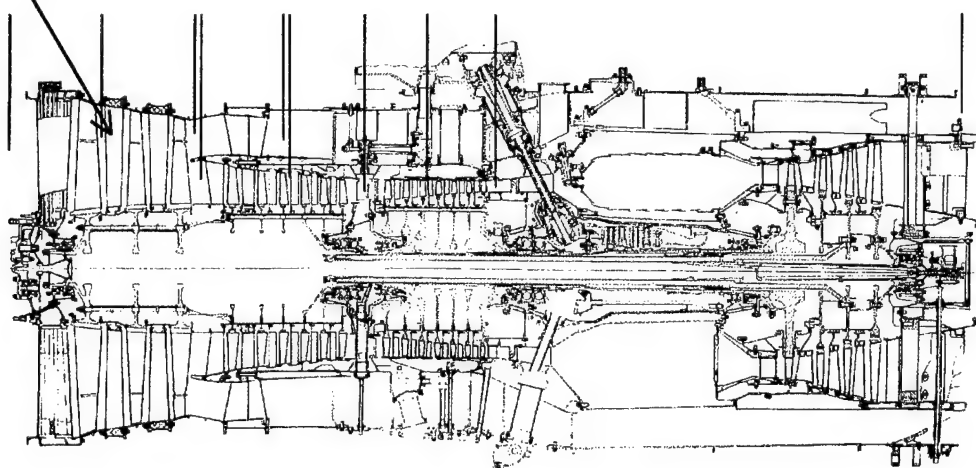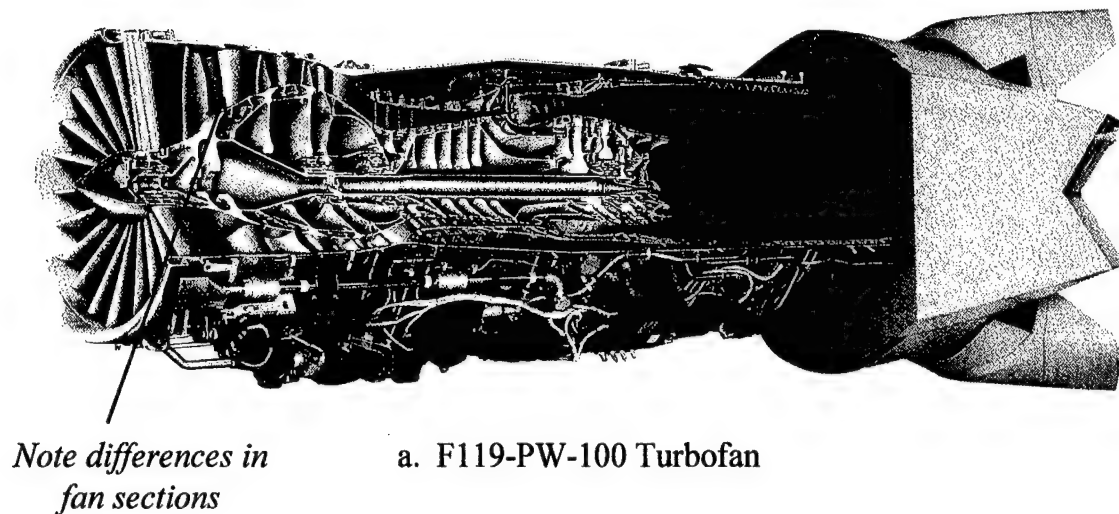
Figure 1 - 1　Cross-sections of F119 and TF30 turbofan engines

those recommended by the Society of Automotive Engineers (SAE) S-16 Committee dealing

with inlet total pressure, total temperature, planar waves, and most recently, swirl (flow

angularity) related to serpentine inlet ducts (see Bibliography for document listing). Of these,

steady-state, inlet total pressure distortion testing using screens remains the dominant approach.

These procedures do not adequately simulate complex, in-flight, flow patterns, evidenced by the

establishment of the fighter engine High Cycle Fatigue (HCF) initiative started in December

1994. One of the key issues being addressed by this government, industry, academia consortium is how to characterize and simulate distortion-induced, unsteady pressure blade loadings (AFRL-PR-WP-TM-1998-2148, 1999).

The use of S-shaped inlet ducts and other stealth-driven design requirements have further complicated the engine-inlet integration issue. Advanced military systems have experienced distortion levels exceeding the current operational experience. Consequences from these unprecedented levels are evidenced into the second stage of modern, military fans. Fighter supermaneuvers and the hover and V/STOL (vertical short take-off landing) requirements of the Joint Strike Fighter (JSF) have also contributed to the need to reassess the engine distortion problem. Properly assessing the situation requires a complementary blend of fan/compressor component tests, engine ground and flight tests, and *numerical experiments* (simulations).

1.3 Scope of Present Research

The present research focused on the development of an existing streamline curvature (SLC) throughflow approach applied to both a single transonic rotor and a state-of-the-art two-stage fan typical of advanced military applications. Here, the SLC method was used in "analysis mode," in which all blade angles were known. The specific SLCC (streamline curvature code) used in the present work was the same as that used by Hale, et al., 1994, 1998, 1999, in the development and application of their Turbine Engine Analysis Compressor Code (TEACC). The TEACC was developed specifically as an efficient alternative to three-dimensional, fully viscous, turbomachinery CFD approaches to investigate complex engine-inlet integration issues.

Fundamentally, the goal of the research was the development of an improved design and analysis tool (numerical approximation) for understanding important flow phenomena in modern fan systems subjected to *off-design operating conditions*. Specific objectives included:

4

- Improve the general applicability of an existing SLCC.

    ➢ Assess models/correlations relative to modern, transonic designs.

    ➢ Incorporate physics-based models, when possible, for improved representation.

- Demonstrate improvements with application to a single rotor and two-stage fan.

- Validate results with those from a Reynolds-averaged Navier-Stokes (RANS) approach.

- Recommend improvements to the TEACC approach involving incorporation of the improved numerical approximation and other lessons learned from the present work.

2. Background/Literature Review

As presented in Section 1.3, streamline curvature (SLC) throughflow approaches remain an important tool for turbomachinery design and analysis. Since the method is well established and documented, only a brief review is provided here, with emphasis on recent developments. The focus of this chapter is to frame the present work by: (a) reviewing higher-order numerical approximations (i.e., fully viscous CFD), and (b) highlighting relevant flow field characteristics of transonic machines. The following subject areas are reviewed:

- Streamline curvature method

- Computational fluid dynamics (CFD)

- Features of transonic fan flow fields

- Unsteady effects on fan performance

In all cases, references are given which provide excellent detail of previous works within each area. The relevant key features are briefly emphasized here. The approach and expected contribution of the present work is discussed in the last section of this chapter.

2.1 Streamline Curvature Method

A description of the SLC method, including assumptions, governing equation, and closure relations, is provided in Appendix A. Further discussion regarding the approach, as well as an assessment of the specific code used in the present work, is provided in Chapter 3. The focus of this section then is on recent developments and previous application to off-design analyses.

Throughflow calculations can be used in *design* (or inverse) mode to determine blade inlet and exit angles and velocity variation from a specified spanwise work distribution, or in *analysis* (or direct) mode when blade angles are specified and flow angles, work, and velocity

6

distributions are predicted. The traditional use of streamline curvature approaches, as most often

discussed in the literature, is during the preliminary design phase. One such example is provided

in Figure 2 - 1. The throughflow solver (SLC) provides a preliminary blade shape, continually

refined through solutions from higher-order and secondary flow models (Figure 2 - 1).

One way to calculate a 3-D flow field is to solve two sets of equations, one dealing with

axisymmetric flow in the meridional plane, commonly referred to as the "S2" surface, and the

other with blade-to-blade flow on a stream surface of revolution, the "S1" plane (see Figure 2 -

2). The most common numerical approach for solution along the S1 and S2 surfaces is the

streamline curvature (SLC) method (Denton and Dawes, 1999; Novak and Hearsey, 1977).
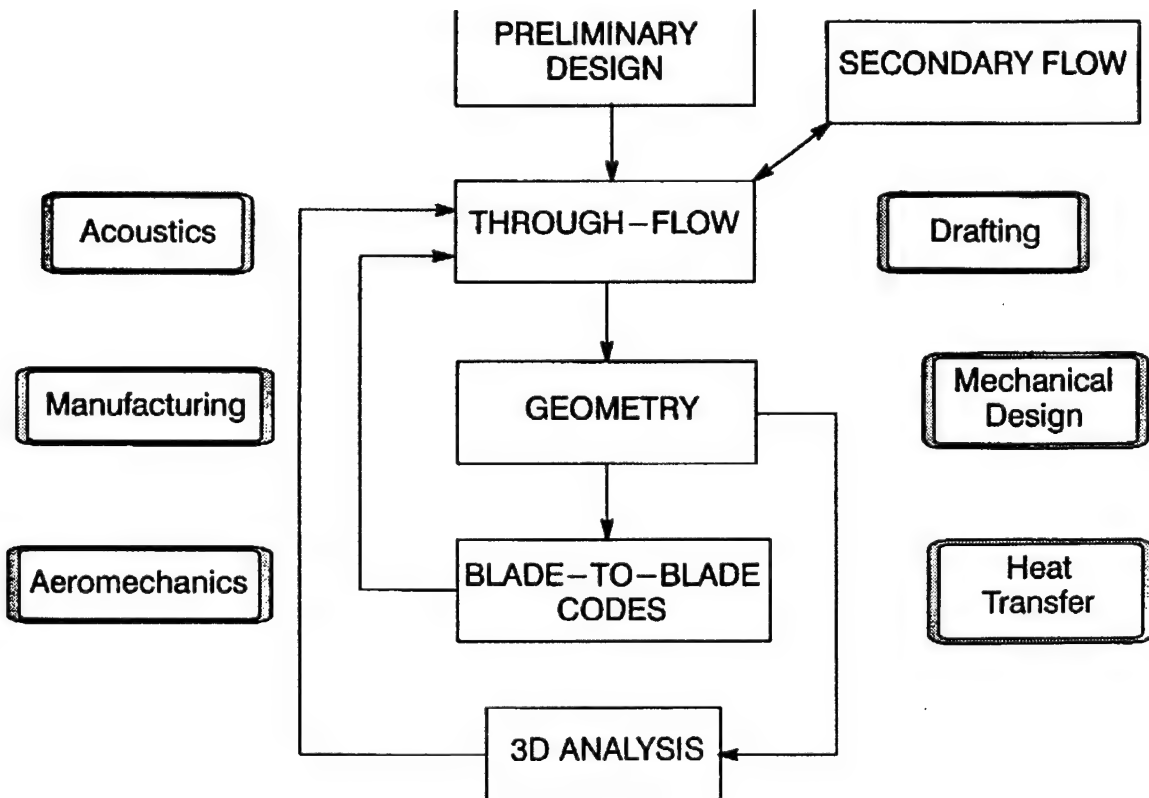
Figure 2 - 1 Turbomachinery aerodynamic design process (Jennions, 1994)

Figure 2 - 2 Illustration of S1 and S2 surfaces (Novak, 1967)

The traditional SLC formulation for the governing momentum equation(s) is a first-order velocity gradient representation, one in the radial and one in the tangential direction (see Equation (A-5) in Appendix A). The present work was concerned with improvements to a SLC approach for off-design analysis along an axisymmetric S2 surface.

It is generally accepted that any streamline curvature solution technique will yield satisfactory flow solutions as long as the deviation, losses, and blockages are accurately predicted. Figure 2 - 3 provides a schematic of blade section geometry and flow characteristics. Accurate prediction of the deviation angle, δ, is essential to predict the correct flow turning and resulting blade work distribution. Clearly, blockage can change the distribution of flow through a blade row – some accounting for its effect is needed. In addition to the profile loss ("wake" and implied boundary layer in Figure 2 - 3), the effects of other loss sources must be included for accurate performance estimation. Excellent recent reviews of loss mechanisms in

8

Figure 2 - 3 Blade section geometry and flow parameter nomenclature (NASA SP-36, 1965)

turbomachines and their representation are provided by AGARD-CP-571, 1996, Bloch, 1996, and Denton, 1993. For the present work, deviation, loss and blockage are discussed further in Chapter 3.

Recently, Denton and Dawes, 1999, reviewed the streamline curvature approach, suggesting that "little has changed" since the review of Hirsch and Denton in 1981 (AGARD Working Group 12 – WG12). This is due in large part to the focus on (and success of) full CFD methods made possible by advancements in computational power (discussed further in Section 2.2). Two recommendations from WG12 apply to the present work (Cetin, et al. 1987):

- Reliable correlations will continue to be needed, as it is not likely that throughflow calculations in multistage machines will be replaced by fully viscous calculations in the near future.

- General trends regarding the influence of parameters of interest (like Mach number) are of particular interest, especially for off-design conditions.

9

Cetin, et al., 1987, furthered the work of WG12 by reviewing loss and deviation correlations relative to transonic axial compressors. Among their conclusions was the need for a consistent endwall boundary layer and secondary loss calculation method and spanwise loss mixing procedures for more accurate predictions. Other recommendations made by Cetin are assessed later in this report relative to present findings. The remainder of this section provides a brief discussion on recent advances and analysis applications of SLC methods relative to the present work.

Throughflow calculations still rely heavily on empirical estimates of loss, deviation, and blockage in compressor endwall regions. To compute these explicitly (in the endwall regions), Dunham, 1995, developed an analytically based endwall model using both annulus wall boundary layer theory and secondary flow theory. He incorporated the model into a streamline curvature program and applied it to low-speed and high-speed multistage compressors to predict overall performance and radial distributions for both on- and off-design conditions (Dunham, 1995, 1996). Figure 2 - 4 provides an example of Dunham's results from a four-stage, high-speed compressor (C147). He attributed the performance differences to excessively thick predicted casing boundary layers in the 3rd and 4th stages, which gave rise to exaggerated deviation estimates in the throughflow and hence an enthalpy rise that was too low. Further, Dunham's model cannot handle endwall corner stall, the prediction of which remains elusive.

Konig, et al., 1996, suggested improvements to blade profile loss and deviation angle models for advanced transonic compressors, including precompression blades (discussed more in Section 2.3). They used measured data sets from eight cascades with various supersonic blade shapes to produce a "modified two-shock model." One result for a precompression profile is shown in Figure 2 - 5. Of particular interest is the parallel alignment of the curves for the
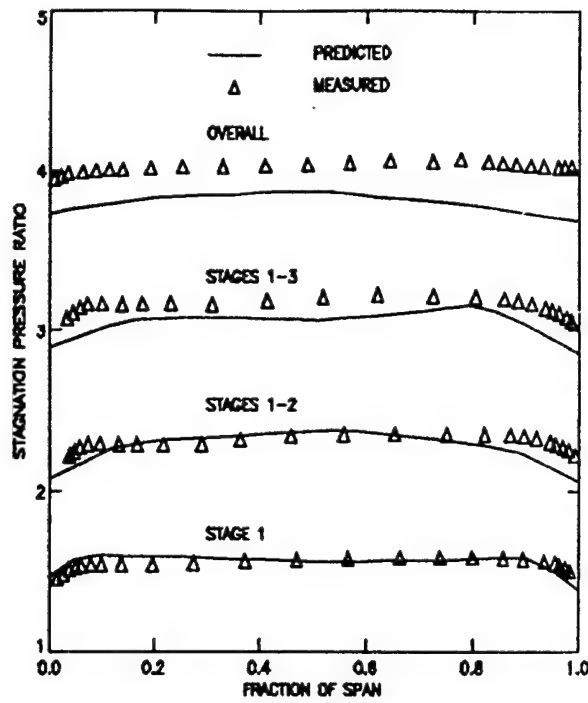
Fig. 6(a)   C147: Pressure ratio
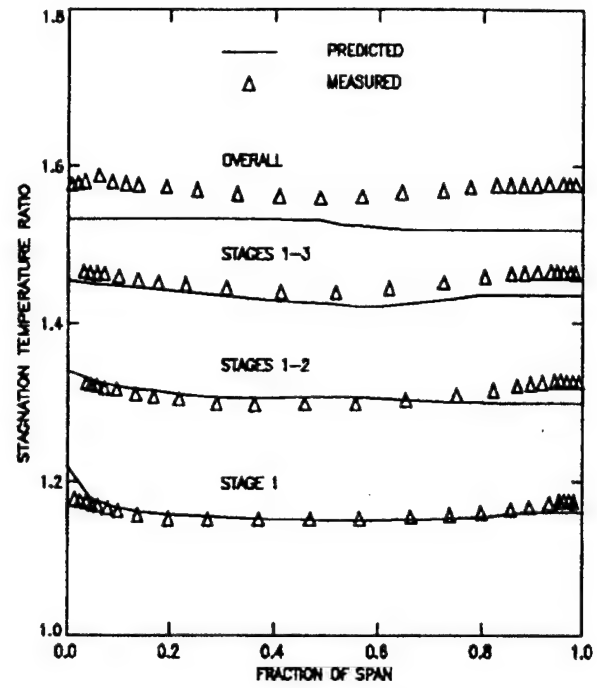
Fig. 6(b)   C147: Temperature ratio

Figure 2 - 4 Radial performance comparison of C147 compressor (Dunham, 1995)
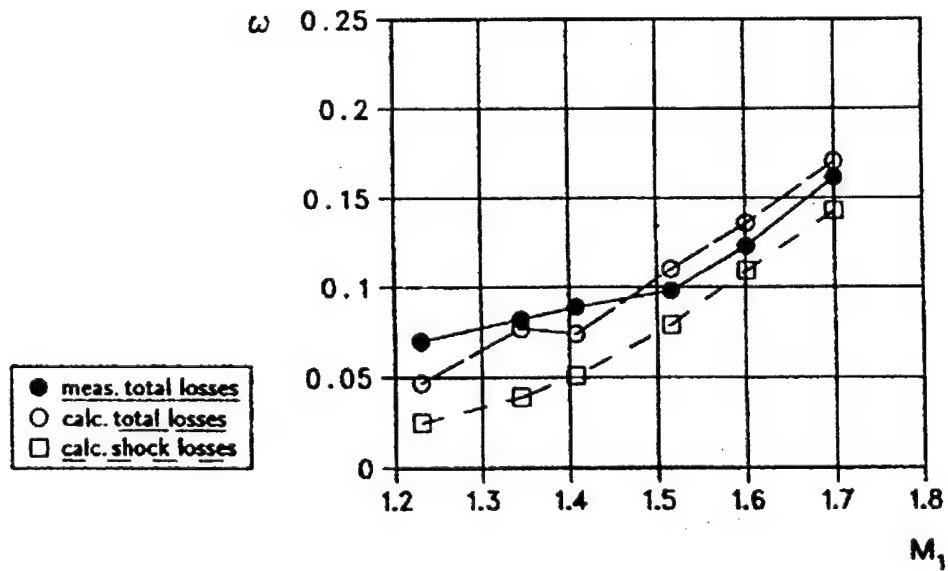
Figure 2 - 5 Calculated and measured losses of precompression airfoil (Konig, et al., 1996)

11

calculated shock losses and measured total losses at high Mach number, indicating that profile losses are relatively independent of Mach number.

Bloch, et al., 1996, 1999, developed a physics-based shock loss model for supersonic compressor cascades of arbitrary shape over the entire operating range. Like Konig, they showed that shock loss is much more sensitive to inlet Mach number than is profile loss. Further, they concluded that the dramatic increase in overall loss with increasing flow angle (demonstrated in Figure 2 - 6) results from increasing shock loss, much of this due to a detached bow shock. Note the nearly parallel alignment of the curves for the calculated shock losses and measured total losses, as well as a CFD prediction for nearly constant profile loss in Figure 2 - 6. Because the Bloch representation was so complete – including influence of operating conditions, estimation of choking incidence, detached bow shock model – it was selected as the basis for the present shock loss model improvements (Chapter 4).
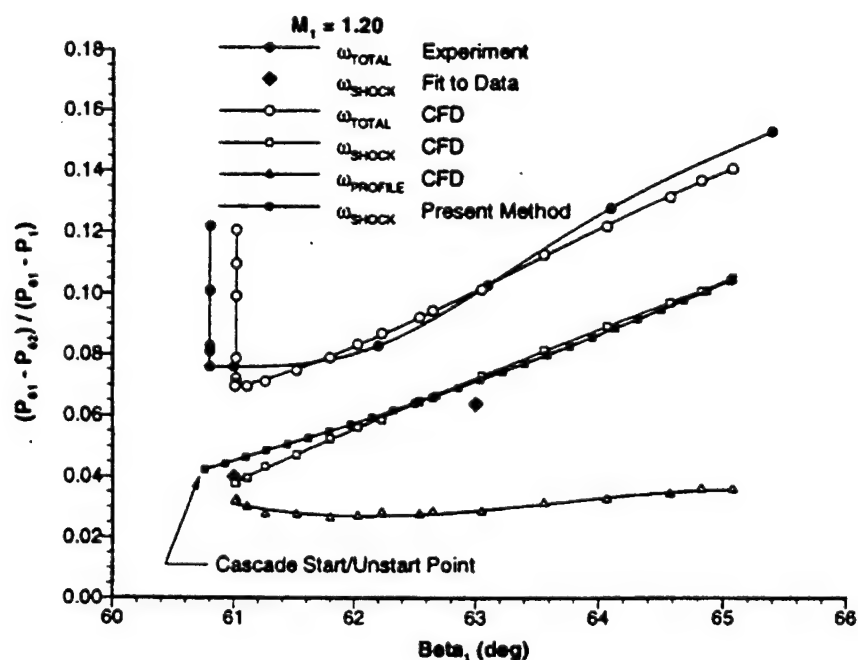
Figure 2 - 6 Loss comparison of the L030-6 cascade with M_1=1.20 (Bloch, et al., 1999)

Perhaps the most sophisticated development of throughflow methods is the approach presented by Gallimore, 1997. He extended an axisymmetric *viscous* model (Howard and Gallimore, 1993) by including a novel approach using tangential blade forces to calculate the extra loss and deviation associated with tip clearance and endwall flows. He combined this with the standard approach of using 2-D blade performance predictions for loss and deviation away from the annulus walls. As illustrated in Figure 2 - 7 for an eight-stage intermediate compressor, Gallimore produced realistic results of accuracy comparable to those from viscous CFD calculations.

(a) Inlet total pressure

(b) Inlet total temperature
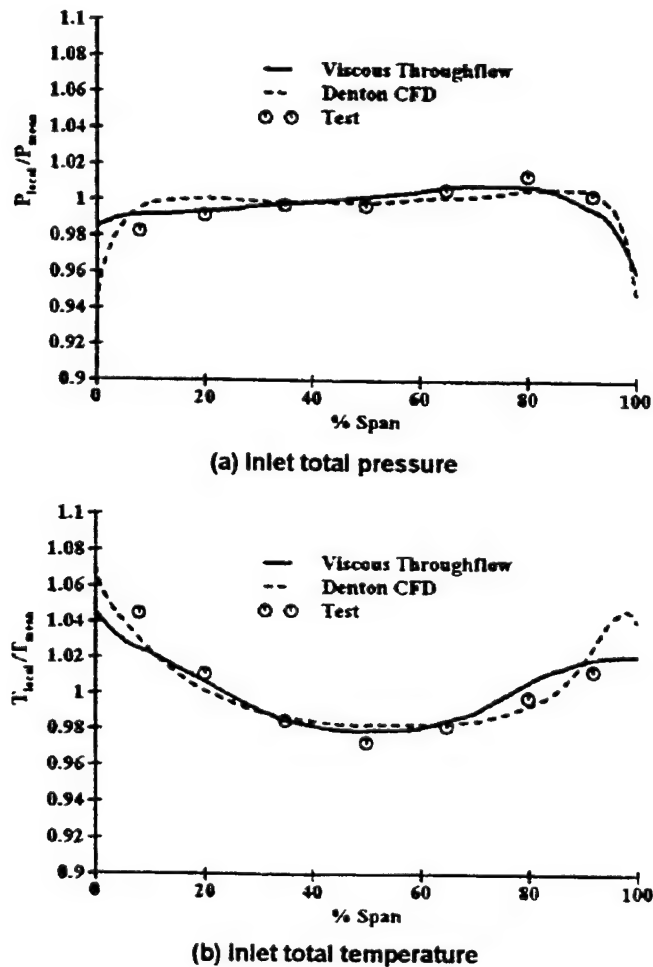
Figure 2 - 7 High-speed compressor stator 8 profiles (Gallimore, 1997)

13
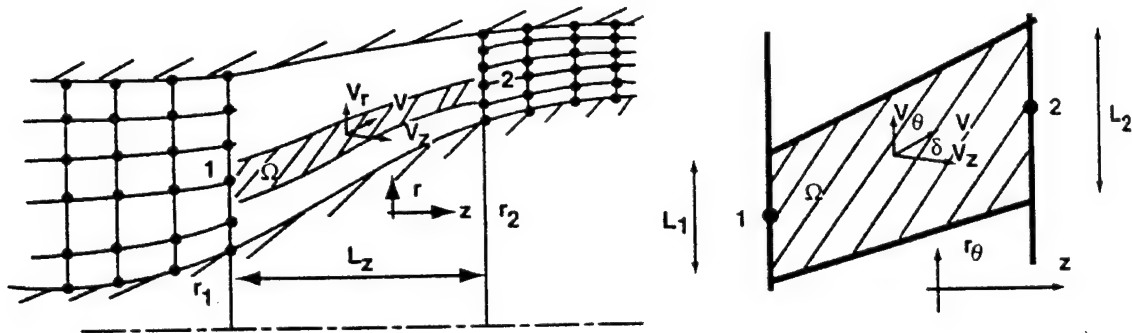
Figure 2 - 8 Modeling of the blade rows in the physical plane (Billet, et al., 1988)

Finally, as an example of novel use of a SLC model, Hale, et al., 1994 developed a 3-D, unsteady, compressible numerical approximation which has been used to study inlet distortion effects on various compression systems (Hale and O'Brien, 1998; Hale, et al., 1999; Davis, et al., 2001). They used a fixed grid to solve the 3-D Euler equations throughout the computational domain, with turbomachinery source terms provided by application of a streamline curvature code across each blade row (Figure 2 - 8). The work extended that of Billet, et al., 1988, by applying the computational grid into and through the blade row, and allowing time-*dependent* radial variation of the streamlines through the bladed region. As mentioned in Section 1.3, the choice of the specific SLC code used in the present work was largely based on potential future applications of the Turbine Engine Analysis Compressor Code (TEACC), discussed in detail in Chapter 7.

2.2 Computational Fluid Dynamics

Recent advancements in computer "power" (memory and speed) and improvements in turbulence modeling have brought computational fluid dynamics (CFD) to the forefront of turbomachinery design and analysis. The development, improvement, and application of turbomachinery CFD dominate the literature. Today, 3-D Euler, quasi-3-D viscous, and 3-D full

14

Navier-Stokes analyses are integral parts of turbomachinery design procedures for all engine manufacturers. As noted by Adamczyk, 1999, "today fan rotors are designed using viscous 3D CFD models…using these models the blade geometry is tailored to control shock location, boundary layer growth and end-wall blockage."

Due to its dominance in the turbomachinery literature, it is appropriate to highlight the CFD approach and contrast it to the chosen numerical approximation. This section provides a brief overview of the CFD method, with particular emphasis on application/potential application to compression system off-design analyses.

2.2.1 Highlights of Turbomachinery CFD

The complexity of the turbomachinery flow field limits CFD simulations to Reynolds-averaged Navier-Stokes (RANS) approximations. The flow field of a transonic fan over its entire operating range is particularly troublesome; it contains all the flow aspects most difficult to represent – boundary layer transition and separation, shock-boundary layer interactions, and large flow unsteadiness. Multistage configurations further the complexity as "neither in the stator nor rotor frame of reference is the deterministic flow steady in time" (Adamczyk, 1999). Direct Numerical Simulations (DNS) and Large-Eddy Simulations (LES) are not currently practical for the fan/compressor flow field.

The DNS explicitly solves for the instantaneous flow field and requires extremely fine gridding to resolve the smallest length scales – on the order of $Re_l^{9/4}$ (Metais, 1996). For a blade chord Reynolds number of 500,000 (a minimum design goal; see Hill and Peterson, 1992, p. 315), a DNS solution would require on the order of 10^{12} grid points per blade passage. Even the relatively coarse grid of the LES (which explicitly solves down to "large" length-scale eddies

and "models" the energy exchanges with small scales) poses a large computational requirement when applied to turbomachinery problems.

Thus, state-of-the-art turbomachinery CFD involves solution of the RANS equations and hence, some modeling of the physics. The Reynolds-averaging process - the decomposition of the instantaneous flow field into mean and fluctuating components and subsequent temporal averaging - introduces more unknowns than available equations for solution. Key modeling aspects are associated with this so-called "turbulent closure problem." To obtain mathematical closure, the Reynolds stress terms must be related to mean flow properties either empirically or through a flow model which allows calculation of this relationship (eddy "viscosity," mixing length, transport equations). As noted by Simpson, 2000, "all the efforts of experimental turbulent shear flow research are aimed at this central problem..." This closure issue is no different than that required of "lower-order" models. For example, throughflow methods using the semi-actuator disk approach (like SLC) require loss and flow angle relationships (empirically or through analytical models).

AGARD Working Group 26 analyzed predictions from a wide range of 3-D RANS codes applied to two different single blade row cases – NASA Rotor 37 is most relevant here. As discussed in AGARD-AR-355, 1998, edited by J. Dunham, only geometric data were provided to research workers who then obtained flow solutions at design speed and 92.5% and 98% of the choked flow. As pointed out by Dunham, all the important types of steady-flow RANS solvers, including a wide range of grids and turbulence models, were represented. Figure 2 - 9, taken from the AGARD report, shows the variation in predicted radial total pressure at the exit of Rotor 37. The total temperature profiles showed similar variation. Some limited information about the solvers, as well as the general type of turbulence model, are provided in the figure. It

16
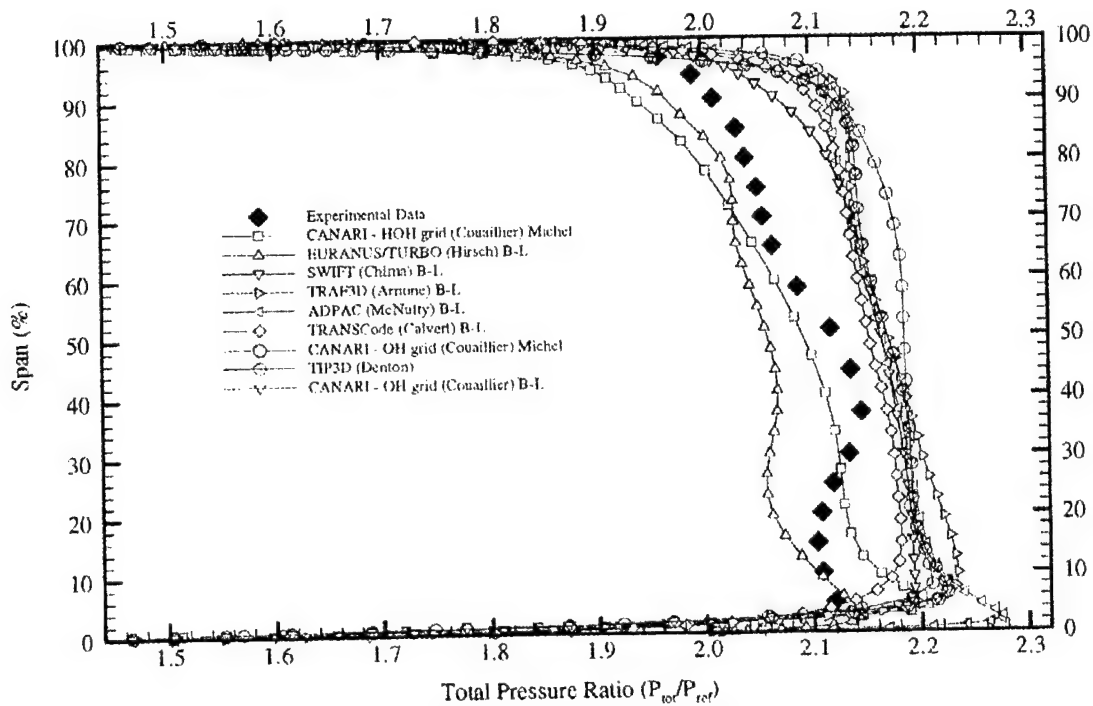
(a) algebraic / mixing length turbulence models
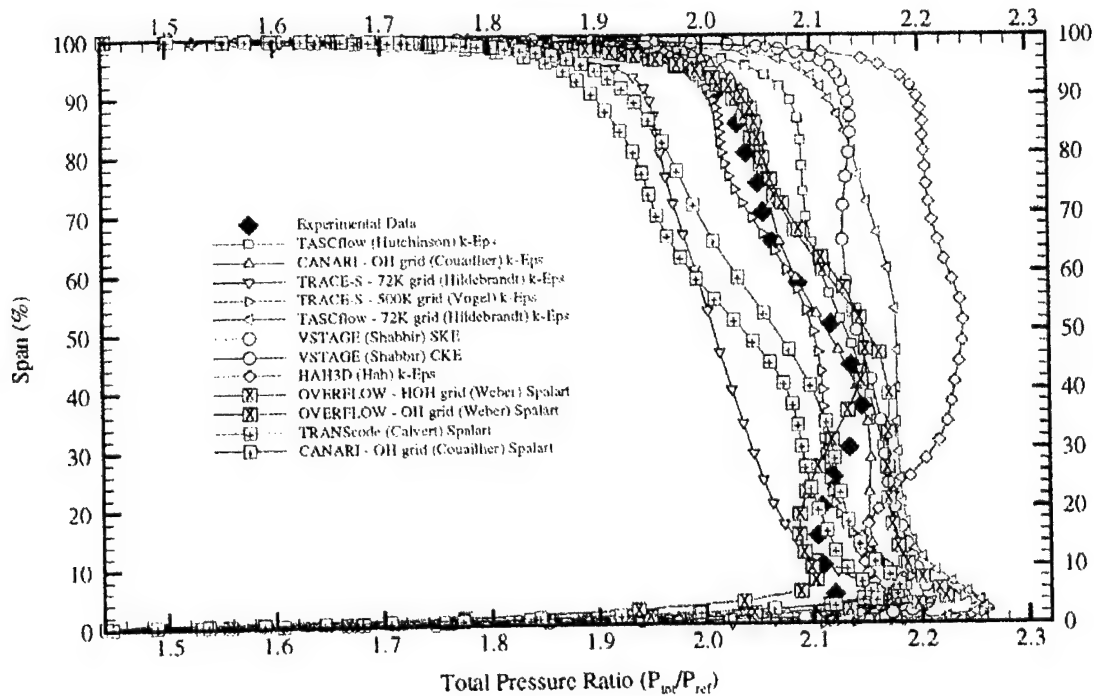
(b) turbulent transport models

Figure 2 - 9 Rotor 37 total pressure ratio (AGARD-AR-355, 1998)

17

is quite apparent that solution accuracy, even for this relatively simple case, is highly dependent on the choice of grid and turbulence model.

There are many recent references providing excellent summaries of the current state of turbomachinery CFD (see for example, Denton and Dawes, 1999; AGARD-AR-355, 1998; and Dorney and Sharma, 1997). These references and others (Adamczyk, 1999; Koch, 1996) were used in the development of Table 2 - 1 to provide a broad assessment of the current state of turbomachinery CFD. Only very recently have these codes been applied to investigate complex off-design issues – like inlet distortion effects – and there limited to a few blade passages or single fan rotor row (Hah, et al., 1998; Rabe, et al., 1999).

The use of RANS codes requires extensive computational resources. A viscous calculation with shock waves and tip leakage typically requires about 300,000 grid points (Denton and Dawes, 1999), although as many as 500,000 points may be needed (AGARD-AR-355, 1998), *per blade passage*. In a recent multistage application, Rhie, et al., 1998, used approximately 1.5 million grid points to represent three stages (seven blade rows), taking advantage of the axisymmetric assumption (i.e., one modeled passage per blade row). They reported about 40 hours for convergence using 21 SUN-SPARC10 workstations. Hah, et al., 1998, reported about 20 single-CPU hours on a CRAY C-90 to obtain a converged unsteady solution using approximately 700,000 grid points over two blade passages (Figure 2 - 10). It should be noted that the rotor shown in Figure 2 - 10 is the first rotor of the two-stage fan modeled in the present work.

2.2.2 Why Not CFD

It is apparent from the discussion of the previous section that turbomachinery CFD, while tremendously successful, is not without its limitations. The choice of whether or not to use a 3-D

Table 2 - 1 Current state of turbomachinery CFD

NUMERICAL TECHNIQUE	DESCRIPTION/STRENGTHS	LIMITATIONS	APPLICABILITY	MATURITY

FCBR	- Predict *unsteady* flow phenomena in compressor stages
	- Multiple blade rows solved simultaneously
		- Large computing resources
		  - Limits number of flow passages
		  - Limits simulations largely to clean inlet
		- Transition & turbulence models
			- Analyze specific cases where unsteady effects suspected to cause problems	Limited practical use/widespread use in a few years

SCBR	- Steady solution for each blade row
	- Effects of adjacent blade rows included through mixed out steady BCs
	- Can include unsteady effects by incorporating deterministic stresses
		- Large computing resources
		  - Limits number of flow passages
		  - Limits simulations largely to clean inlet
		- Transition & turbulence models
			- Design/Off-Design
			- Optimize blading & flowpath contours
				Widespread use/routine use in a few years

SSBR LCBR	- Each blade row solved in isolation - With LCBR, unsteady BCs specified & periodically updated to account for interaction mechanisms	- No interaction mechanisms included, or for LCBR must be known & specified (i.e., upstream wake profile) - BCs obtained from throughflow calculation - Transition & turbulence models	- Design - Analysis, prediction of tip leakage & secondary flows	Current routine use
Euler	- Multiple blade rows solved simultaneously - Includes unsteady potential-flow & shock interaction effects from adjacent blade rows - Reasonable computing resources	- Requires loss, deviation, blockage correlations or experimental data to account for viscous effects - Questionable applicability to new designs (specially if correlations not physics based)	- Design - Analysis	Current routine use

Key: FCBR – Fully Coupled Blade Row (unsteady)   SSBR – Steady Single Blade Row
              SCBR – Steady Coupled Blade Row   LCBR – Loosely Coupled Blade Row
              (NOTE: The four abbreviations above refer to techniques that solve the Navier-Stokes equations; terminology taken from Dorney and Sharma, 1997)

BCs – Boundary conditions at inlet and exit

100 circum. x 46
span x 152
stream.
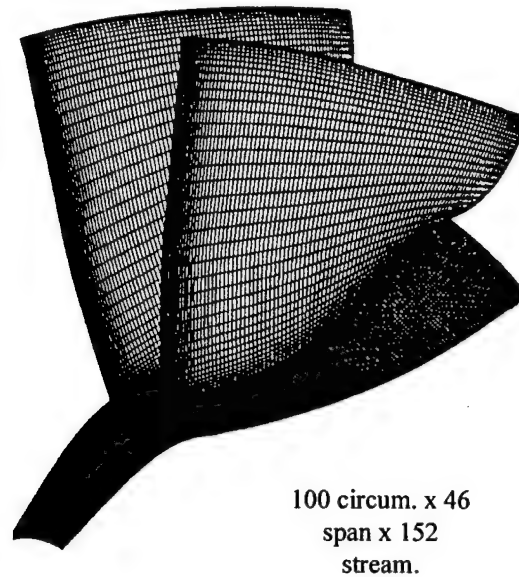
Figure 2 - 10 Typical computational grid (Hah, et al., 1998)

CFD approximation (instead of other representations requiring more modeling) essentially comes

down to a tradeoff between increased flow resolution and computer resources (CPU time,

memory size, and cost), as well as consideration of "length-scale of interest (LSI)." Adamczyk,

1999, points out further that the consideration must include "…costs of supporting the empirical

data base required to underpin the model" (note this is true of all computational models).

To a large extent, the LSI of the flow problem under consideration dictates the choice of

computational model. If flow passage details are desired – tip vortex-boundary layer

interactions, shock unsteadiness, hub-casing boundary layer/vortex dynamics – then the LSI is

perhaps orders of magnitude smaller than the boundary layer thickness (i.e., the Kolmogorov

scale – Tennekes and Lumley, 1972), and full CFD is the obvious choice. As already pointed out

in this and the previous chapter, for complex, off-design flow analysis through multistage

configurations, practical application of 3-D unsteady CFD methods is at best, difficult. Thus,

simpler methods with improved, physics-based modeling must continue to be developed. Of

course, the *effects* of any key phenomena not physically modeled (i.e., viscous effects in an Euler solver) must be included in whatever engineering approximation is employed. This inevitably requires the use of empiricism, directly through correlations or indirectly through the development of models to relate unknown quantities to known quantities. Compounding the problem is the fact that all key phenomena may not necessarily be known a priori. The remaining sections of this chapter review the key features of compression system transonic flow fields. This review is intended to highlight features which must be modeled and discuss the implications (quantitatively, when possible) of those that are not.

2.3 Features of Transonic Fan Flow Fields

Key flow field features relative to transonic fans for military application are discussed in this section. These features include highly 3-D flow fields, complex shock systems, and strong interactions between the shock, boundary layer, and secondary flows (like the tip-leakage vortex). The goal is to provide a basic understanding so that proper assessment of the chosen numerical approach can be performed.

As suggested by Figure 1 - 1 and Figure 2 - 11, the flow fields of modern military aircraft fan designs are complex and highly three-dimensional. The flowpath hub contour shown in Figure 1 - 1a suggests significant radial velocity components, especially at the fan entrance and through the first two stages. Secondary flows and their interactions are another major source of flow complexity (Figure 2 - 11). Indeed, Denton and Dawes, 1999, suggest the prediction of blade surface and endwall corner separations to be one of the most challenging tasks of 3-D, viscous solvers, largely due to the obvious dependence on turbulence model. Additionally, the use of blade twist, sweep (viewed from the meridional plane) and lean (observed looking axially through the machine) contributes to the 3-D flow effects. Clearly, consideration of these 3-D

21
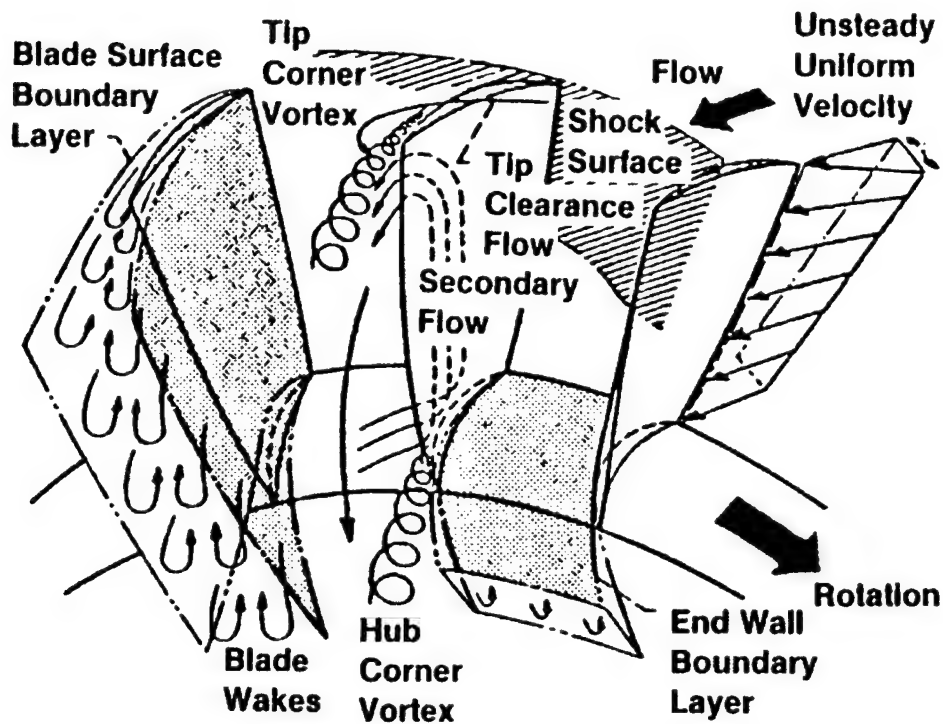
Figure 2 - 11 Complex flow phenomena in compressors (Wisler, 1987)

effects is needed in any approximation expected to provide reasonable fidelity in its performance

simulations of modern fans.

A significant consideration in the design of transonic fan blades is the control of shock

location and strength to minimize aerodynamic losses without limiting flow. As discussed by

Wisler, 1987, custom-tailored airfoil shapes are required to "minimize shock losses and to

provide desired radial flow components." Copenhaver, et al., 1993 provide details of 3-D flow

phenomena in a transonic stage, Rotor 4. As discussed, Rotor 4 was designed specifically (as

part of a parametric design investigation involving seven rotors) to better understand the effect of

blade suction surface shape on shock strength.

Figure 2 - 12 shows features of the tip section geometry typical of a transonic fan. The

shape of the suction surface is key as it: (a) influences the Mach number just ahead of the leading
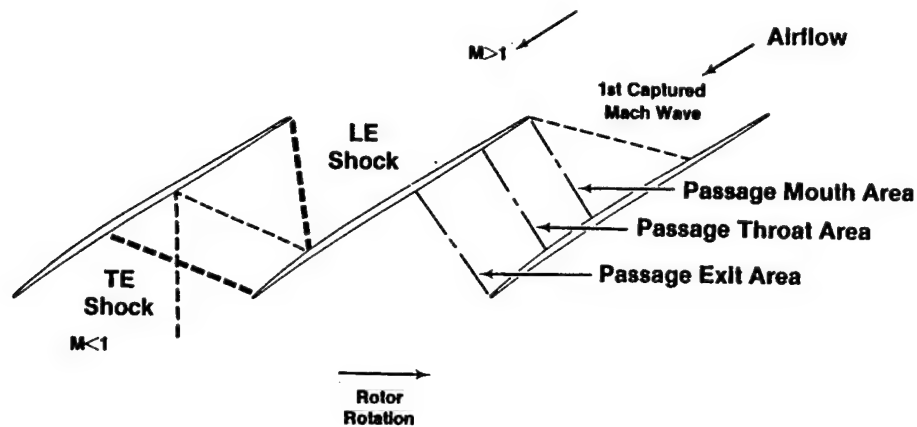
Figure 2 - 12 Fan tip section geomentry (Wisler, 1987)

edge passage shock, and (b) sets the maximum flow rate (Parker and Simonson, 1982). As noted by Wisler, 1987, the cascade passage area distribution is chosen to provide larger-than-critical area ratios; thus, maximum flow is determined by the first captured Mach wave, location determined by the forward suction surface (induction surface). This maximum flow condition is often referred to as leading edge choke, or in cascade parlance, "unique incidence" (note that "unique" incidence is really a misnomer; here, "choking" incidence will be used).

The flow induction surface and fan operating condition (incoming relative Mach number at the airfoil leading edge) set the average Mach number just ahead of the leading edge passage shock. A "traditional" convex suction surface results in a series of Prandtl-Meyer expansion waves as the flow accelerates around the leading edge (see Figure 2 - 13a). Increasing the average suction surface angle (relative to the incoming flow) ahead of the shock reduces the average Mach number, and presumably reduces the shock losses. Common for modern transonic fan tip sections is a concave induction surface, the so-called "precompression" airfoil. Figure 2 - 13b shows one example taken from Tweedt, et al., 1988. Note the difference between Figures 2-13a and 2-13b - the Mach waves associated with a precompression section coalesce in the flow

23

Neutral Characteristic

Bow shock

Expansion waves

Passage Shock

M_1

β_1

B

A

First Captured Mach Wave
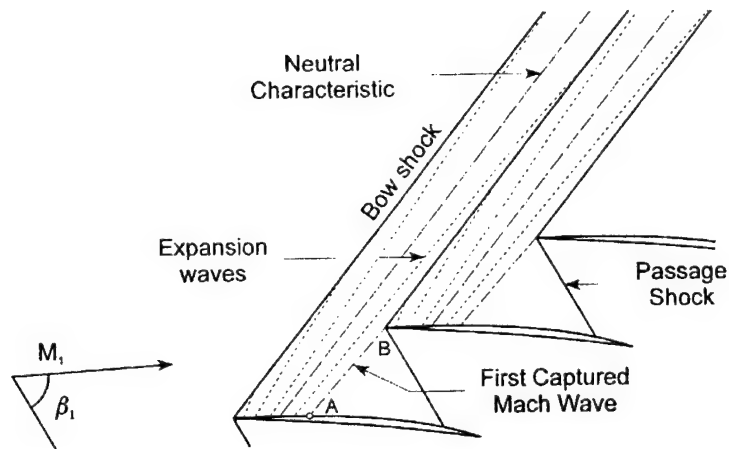
a. Convex or "traditional" induction surface (Bloch, 1996)

$M_1 = 1.61$

$M_{max} = 1.68$

$M_{LE} = 1.76$ $M_{min} = 1.53$
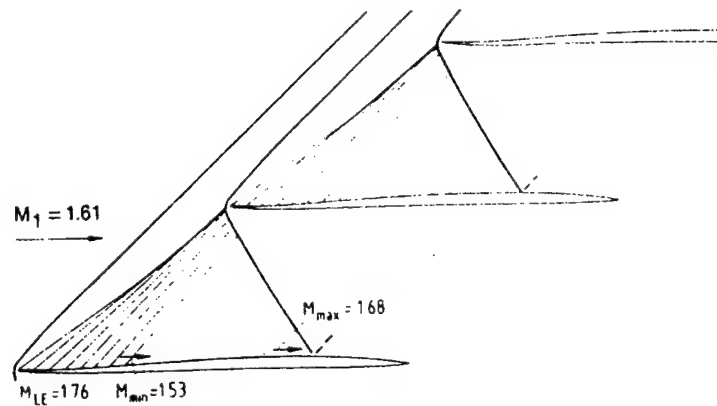
b. Concave or "precompression" induction surface (Tweedt, et al., 1988)

Figure 2 - 13 Approximate wave patterns for traditional and precompression airfoils

induction region forming a weak shock, but strong enough to cause a significant reduction in Mach number. It should further be noted that the induction surface, whether concave or convex, is shaped to deviate only slightly from the direction of the undisturbed flow (Wisler, 1987); thus, an isentropic analysis in this region is appropriate.
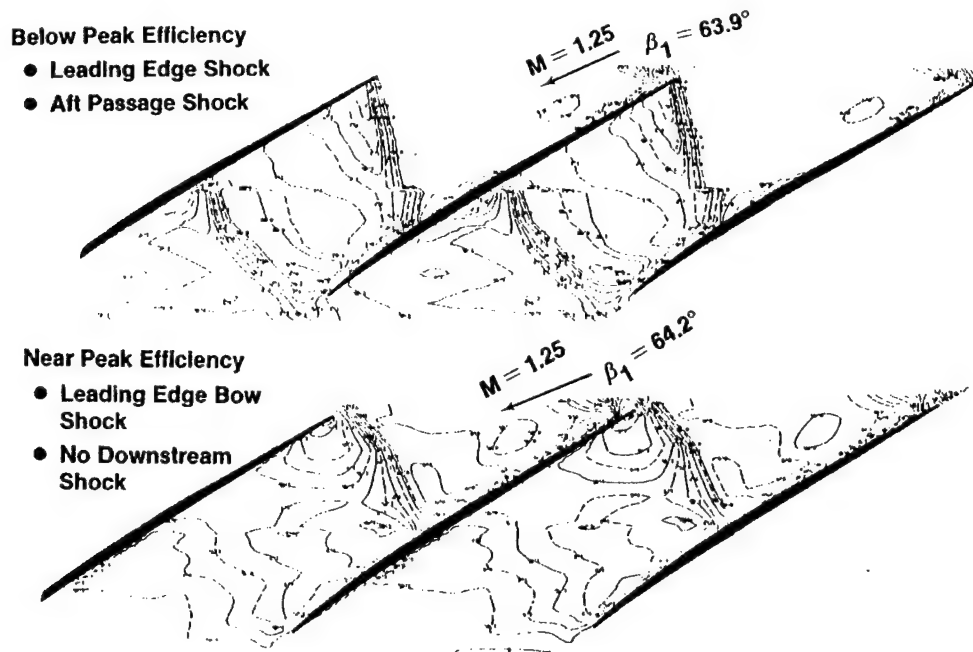
Figure 2 - 14 Shock structure of transonic fans (Wisler, 1987)

The shock structure associated with transonic fans is complicated by the 3-D nature of the flow field and operating range over which the fan must operate. Figure 2 - 14 illustrates some typical features – leading edge oblique shock, aft passage normal shock below peak efficiency, and a near-normal, detached bow shock near peak efficiency (and higher) loading conditions. Note that throughout this report, *loading* refers to flow *turning*. For high tip-speed fans (inlet relative Mach numbers greater than 1.4), the trend seems to be to design for an oblique leading edge shock through higher loading conditions (near and at peak efficiency). This is illustrated in Figure 2 - 15, taken from three different investigations – Bloch, et al., 1996; Adamczyk, et al., 1991; and Chima and Strasizar, 1983 (figure from Bloch, et al., 1996). This trend seems reasonable given the continued need to reduce losses (discussed further in Chapter 4).

Other flow field considerations in transonic fans include the interrelationship between the rotor tip-clearance vortex structure and passage shock, high Mach number stator flow, most notably in the hub region, and strong shock – boundary layer interaction. Copenhaver, et al.,

25
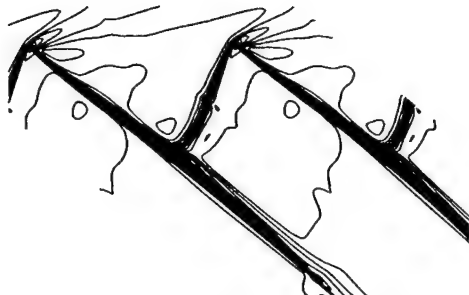
Figure 4. Mach Number Contours Near Stall in a Transonic Fan.
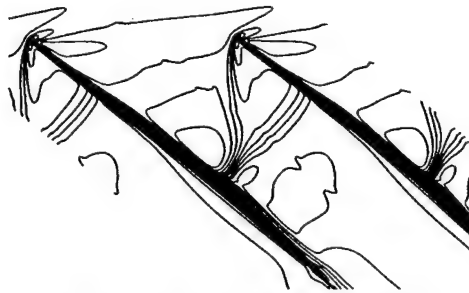
Figure 5. Mach Number Contours Near Peak Efficiency in a Transonic Fan.
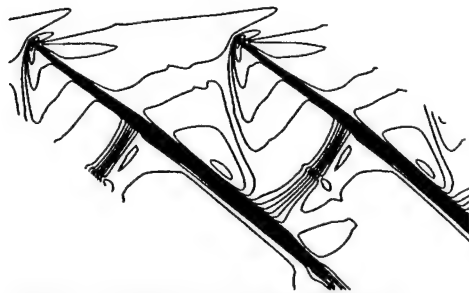
Figure 6. Mach Number Contours for Back Pressure Slightly Below the Maximum Choked Value.
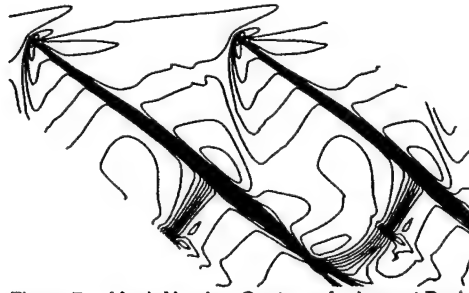
Figure 7. Mach Number Contours for Lowest Back Pressure Operating Point.

a. from Bloch, et al., 1996

SIMULATION   EXPERIMENT
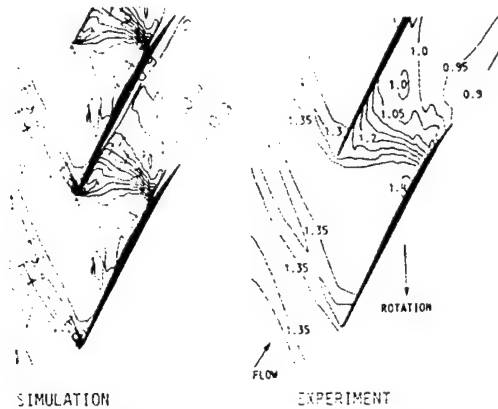
Mach contours at near peak efficiency

A) NINETY PERCENT SPAN FROM HUB

b. from Adamczyk, et al., 1991
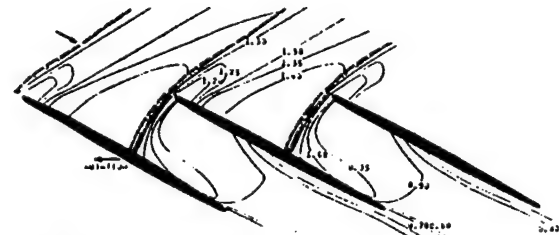
a) Near-Stall Condition
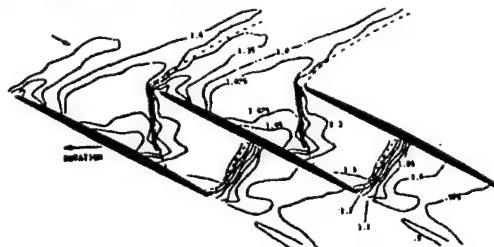
b) Maximum Flow Condition

Figure 8. Measured Shock Structure for 15% Rotor Immersion (Chima and Strasizar, 1983).

c. from Bloch, et al., 1996

Figure 2 - 15 Shock structure of high tip-speed fans ($M_{1rel} > 1.4$)

1993 demonstrated that interactions among the passage shock, tip-leakage vortex, and the boundary layers directly influenced the overall efficiency and operating range of a transonic, high-performance stage. As discussed in Section 2.1, Dunham, 1995, provides an example of the importance of accurate endwall modeling in the compressor flow field. Unsteady effects, discussed in the next section can also significantly contribute to the flow structure.

The shock – boundary layer interaction is a well-known important phenomenon discussed in the literature, as well as most textbooks on gas dynamics (see for example, Chapter 13 of Liepmann and Roshko, 1967). The presence of a boundary layer (on a blade and/or endwall) alters the boundary condition for a shock, and, the large pressure gradients due to the shock strongly alter the boundary layer flow. The effects from these interactions can include boundary layer separation, and a spreading of the pressure rise across the shock over a considerable length; i.e., the shock is felt upstream. Rabe, et al., 1987, used laser anemometry to characterize the shock wave endwall boundary layer interactions in the first rotor of the same two-stage fan used in the present work (see Section 5.1). They demonstrated that the separation between the endwall boundary layer and core flow around the rotor leading edge appeared to be the result of a shear layer where the passage shock and all ordered flow seemed to end abruptly.

2.4 Unsteady Effects on Fan Performance

There are many excellent recent reviews on the subject of unsteady flows – for example, VKI LS 1996-05 and AGARD-CP-571, 1996. For the purpose of the present work, the objective of this section is to provide sufficient background to assess the impact of omitting unsteady effects. Where possible, a quantitative assessment is provided.

It is useful to consider unsteadiness related to length scale, as presented in the Foreword section of VKI LS 1996-05. At the "microscopic" scale (order of blade thickness) are wakes,

vortices and their interactions with adjacent blade/vane rows. Fan and Lakshminarayana, 1994, showed typical increases of about 10% in time-averaged loss coefficient over that for steady flow, dependent on axial gap and the wake-passing frequency.

Shock unsteadiness also falls in the microscopic category. Ng and Epstein, 1985, were the first to propose a "moving shock hypothesis" to account for measured blade-to-blade (core flow) fluctuations at a frequency of three to four times blade passing. They used a simple mixing calculation to show that this high frequency unsteadiness contributed on the order of one percent of the rotor loss. Hah, et al., 1998, showed that the interaction between oscillating passage shock and blade boundary layer and resultant vortex shedding were the dominant flow structures when the transonic fan studied encountered a strong circumferentially non-uniform distortion. The passage shock moved by as much as 20% of the chord during the distortion period, increasing the effective blockage in the outer 40% of the blade span, producing an overall rotor efficiency decrease of one percent with the inlet total pressure distortion.

At the "medium" scale (on the order of blade chord) are rotating stall and potential-flow effects. Potential flow interactions result from variations in pressure fields (the velocity potential) associated with the relative motion between blades and vanes in adjacent rows. The effects of these interactions are typically significant when axial spacing between adjacent rows is small or flow Mach number is high (Dorney and Sharma, 1997), both of which are true for modern transonic fans. Finally, the "macroscopic" scale deals with time-variant flows at the level of the total compressor, such as surge.

Another aspect of time-variant flows is blade unsteady response, important for accurate stall prediction. This remains an area of fruitful research, especially when applied to distorted inlet flow fields. Common techniques to account for this unsteady response include first-order

lags on the quasi-steady compressor characteristics or forces (Mazzawy and Banks, 1976, 1977; Davis and O'Brien, 1991), critical angle concept (Reid, 1969; Longley and Greitzer, 1992), and the so-called "reduced frequency" parameter (Mikolajczak and Pfeffer, 1974). All these typically rely extensively on empiricism or are overly simplified.

Recently reported (Boller and O'Brien, 1999; Howard, 1999; and Schwartz, 1999) and currently ongoing investigations (Small, 2001) build upon the work of Sexton and O'Brien, 1981, and Cousins and O'Brien, 1985, in establishing the use of a frequency response function (FRF) to characterize unsteady blade response. Specifically, these recent studies seek to predict dynamic stage performance through definition of a "generalized" FRF determined from time-varying flow characteristics in the rotating reference frame when a compressor is subjected to inlet distortion. While still largely empirically-derived, this approach offers higher fidelity than previous ones because it captures the effects of all potentially relevant time scales – boundary layer response, distortion period, and blade passage residence time.

2.5 Approach of Present Work

Physics-based improvements to "simplified" (other than 3-D, viscous CFD) numerical approaches are needed. The brief literature review presented here (and to some degree in Chapter 1) has pointed out that:

- reliable and robust, off-design analysis of compression systems is still very difficult.
- although limited by loss, deviation, and blockage representation, novel approaches which use the streamline curvature method (like Billet, et al., 1988, and Hale and O'Brien, 1998) offer potential for accurate, rapid, off-design analyses.
- despite its impressive advances, turbomachinery CFD has its own limitations, most notably in computational requirements and turbulence and transition modeling.

In the present work, the goal was an improved design and analysis numerical tool for understanding important phenomena in a modern fan system subjected to off-design operating conditions. Solutions were sought that retained essential global features of the flow which: (a) might point to areas requiring more local representation, or (b) could be used to provide more accurate boundary conditions for a fully 3-D, unsteady RANS code (i.e., at the inlet and exit of a blade row). The SLC code (SLCC) was specifically chosen because of its use in the TEACC discussed in Sections 1.3 and 2.1. With the improved SLCC and additional modifications (presented in Chapter 7), the TEACC method offers potential for analyzing the types of problems discussed in Chapter 1.

The approach outlined below was followed:

- An existing SLC computational approach was modified to improve the representation of key phenomena relative to transonic fans. This was manifested predominantly through an improved, physics-based shock loss model, discussed in detail in Chapter 4. Chapter 3 provides an extensive assessment of the specific streamline curvature method used here. Modifications other than the shock model are presented in this chapter.

- The improvements were verified through application to a single blade row – NASA Rotor 1B – and to a two-stage, highly transonic fan with design M_{1rel} of about 1.7 (Chapters 5 and 6). Measured data from Rotor 1B, and both data and results from a steady, 3-D, RANS code for the two-stage machine provided the basis for comparison to the SLCC predictions. A sensitivity study was included to quantify the accuracy of loss, deviation, and blockage prediction needed to achieve a desired level of performance estimation.

- Recommendations were made regarding improvements to the TEACC methodology initially proposed by Hale, et al., 1994. These included incorporation of the improved SLCC, as well

as other recommendations based upon lessons learned from the present investigation (Chapter 7).

Conclusions and overall recommendations are provided in Chapters 8 and 9, respectively.

3. Modeling Approach and Assessment

3.1 Streamline Curvature Approach

Essentially, with the streamline curvature (SLC) approach applied to the S2 surface (Figure 2 - 2), blade rows are represented as a series of radially segmented semi-actuator disks. Hale and O'Brien 1998, described the solution as "axisymmetric flow with swirl." Primary output includes prediction of the radial distribution of meridional velocity and streamline location. This well-established technique is described in some detail in Appendix A.

As was discussed in Section 2.1, streamline curvature techniques yield satisfactory flow solutions as long as the deviation, losses, and blockages are accurately predicted. The SLCC used here was originally developed by Hearsey (Hearsey, 1994). It uses empirical, 1960s, cascade data to determine low-speed, minimum-loss "reference" deviation and loss, then "corrects" these values for various real-flow effects, including those from annulus wall boundary layer, spanwise mixing, and secondary flows (see Appendix A). Fundamentally, this breakdown of deviation and loss into different components is a sound and proven engineering approach – Howell, 1945, is a classic example (Horlock, 1982), while Denton, 1993, provides a more recent illustration. This approach, however, poses a problem when an application is outside the database used to develop the empirical/semi-empirical correlations. Such was the case for the present investigation.

Because the blade section profiles and flow field of the present application are significantly different from the NACA 65-series profiles (NASA-SP-36, 1965) used to develop the correlations, the reference conditions used as the basis for deviation and loss determination were suspect. Consequently, a detailed assessment was performed on the loss and deviation correlation methods used by the streamline curvature approach described in Appendix A.

32

Results from the assessment led to: (a) the selection of various SLCC parameters based on physical arguments, and (b) physics-based improvements to selected models/correlations. The net effect was an improved, more physics-based, engineering representation of a modern fan. Because of its impact to the present application, improvement of the shock loss model is described in detail in Chapter 4. Assessments of the deviation, loss, and blockage "models" of the present approach are provided in the next three sections.

3.2 Deviation Assessment

Hearsey's method for determining the exit flow deviation angle (Appendix A) was assessed relative to that recommended by Cetin, et al., 1987. Because of the complexities involved with separating individual deviation (and loss) sources, their approach considered deviation as a whole. For the following reasons, it was decided to remain with the Hearsey's approach:

- Cetin, et al. recommended a modification to Carter's rule to account for underestimation of the deviation at design conditions. They attributed the required correction to transonic and 3-D effects. The Hearsey method already used a modified Carter rule and included provisions for transonic and 3-D effects.

- The off-design deviation correlation they recommended (Creveling and Carmody, 1968) contained minimal data at supersonic relative Mach numbers – only data up to $M_{1rel} = 1.10$ were included. A detailed assessment of off-design deviation estimation for highly transonic bladings is needed, which is beyond the scope of the present work.

The original equation for determining deviation angle (and the one used for the present work), Equation (A-10), is repeated below for convenience:

$$\delta = \delta_{ref} + \delta_{3D} + \delta_M + \delta_{va} + \delta_i \qquad (A-10)$$

The low-speed, minimum-loss reference deviation is discussed in Appendix A. The deviation due to 3-D effects, δ_{3D}, attempts to account for the complex interactions of secondary flows with endwall boundary layers and tip leakage flows. Essentially, use of this deviation component applies the curves shown in Figure 3 - 1. The negative deviation increments in the tip sections can be attributed to the dominance of tip leakage flows. In general, the jet of high-velocity fluid that is directed into the suction surface-endwall corner tends to re-energize the boundary layer sufficiently to prevent separation. This is not the case in the high-turning hub region, where cross-passage secondary flow and interaction with annulus boundary layer often lead to suction surface corner separation (note that the bowed stator concept was developed specifically to address this issue – see Weingold, et al., 1995). Denton, 1993, discusses all these effects in detail.

(a) NACA 65–(A_{10})-series blades.
(b) Double-circular-arc blades.
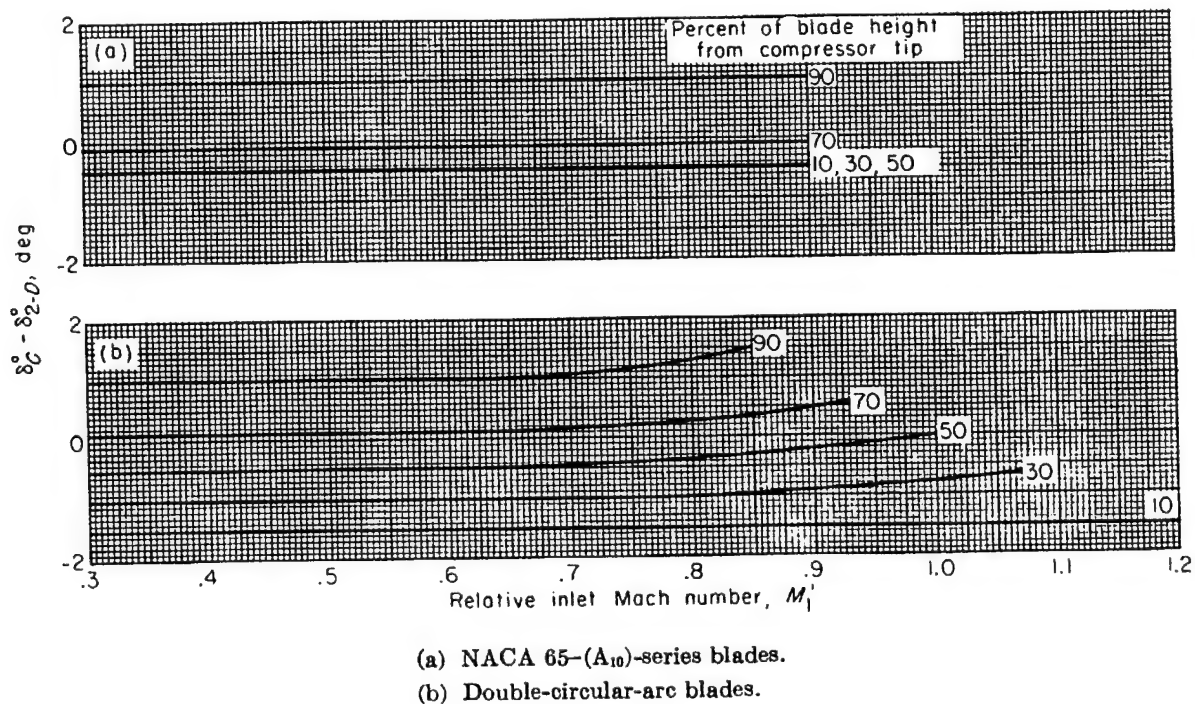
Figure 3 - 1 Deduced variation of average rotor deviation angle minus low-speed 2-D-cascade rule deviation angle at compressor reference incidence angle with relative inlet Mach number (NASA SP-36, 1965)

The deviation component due to increased Mach number, δ_M, was not used in the present investigation. Results from recent studies show that profile loss of highly transonic blades remains relatively constant (discussed in Section 2.1). This suggests that δ_M is relatively unimportant, most likely due to the dominance of tip leakage flow (discussed in the previous paragraph) over increased shock – blade boundary layer interactions (tending to increase deviation).

The deviation due to axial velocity ratio, δ_{va}, was used and is easily understood. If streamtube contraction occurs through a blade row, the meridional velocity increase tends to energize the boundary layer and prevent separation. As described by Hearsey, 1994, the following simple expression was used (with limits of +/-5 degrees):

$$\delta_{va} = 10(1 - \frac{V_{m2}}{V_{m1}}).$$
(3 - 1)

The last deviation component, δ_i, deviation due to actual incidence, is most suspect because it is based solely on correlations developed from NACA 65-series data. The method essentially uses a four-piece curve to describe the variation of deviation as a function of incidence (see Hearsey, 1994). As previously mentioned, a detailed study of this relationship is needed for transonic designs.

Table 3 - 1 provides an example of the magnitudes of the various deviation components at 15 radial locations along the rotor span. They were obtained from a simulation at peak efficiency flow condition at 98.6% Nc (design corrected speed) across the first rotor of the two-stage fan (Chapter 5) modeled in the present work. Tip relative Mach number at this condition was about 1.66. The "r1" and "r2" represent the LE and TE radial streamline location across

Table 3 - 1 Sample SLCC output showing deviation angle (d) components

r1	r2	Vratio	i	lref	lmn	dref	d3d	dm	dva	di	dadd	dtotal
4.618	8.612	1.238	-4.039	6.425	9.976	8.069	1.638	0.000	-2.377	-0.859	2.592	9.063
6.006	9.054	1.129	0.090	4.172	8.435	7.807	1.732	0.000	-1.292	-0.518	-1.594	6.136
7.048	9.473	1.043	2.246	2.918	7.526	7.109	1.749	0.000	-0.432	-0.092	-2.686	5.647
7.910	9.869	1.005	3.534	2.197	6.785	6.258	1.683	0.000	-0.051	0.249	-1.792	6.347
8.658	10.239	0.971	4.422	1.877	6.047	5.416	1.682	0.000	0.295	0.614	-2.140	5.867
9.327	10.592	0.935	5.132	1.764	5.276	4.568	1.676	0.000	0.653	0.959	-2.913	4.944
9.936	10.932	0.905	5.611	1.736	4.575	3.856	1.589	0.000	0.948	1.223	-3.691	3.924
10.501	11.262	0.879	5.876	1.723	4.031	3.334	1.442	0.000	1.213	1.397	-4.234	3.152
11.029	11.585	0.860	6.120	1.727	3.605	2.907	1.266	0.000	1.398	1.563	-4.779	2.356
11.527	11.901	0.838	6.251	1.720	3.248	2.522	1.031	0.000	1.616	1.676	-5.217	1.628
12.001	12.215	0.817	6.241	1.692	2.949	2.195	0.656	0.000	1.834	1.714	-5.483	0.917
12.455	12.526	0.807	6.236	1.675	2.730	1.962	0.082	0.000	1.933	1.742	-6.205	-0.485
12.890	12.835	0.796	6.226	1.667	2.544	1.757	-0.676	0.000	2.036	1.759	-6.942	-2.065
13.311	13.146	0.781	6.181	1.660	2.364	1.533	-1.584	0.000	2.194	1.750	-7.588	-3.694
13.719	13.619	0.739	5.953	1.644	2.176	1.280	-3.125	0.000	2.606	1.623	-6.760	-4.376

Radii in inches

All angles in degrees

36

each of fifteen airfoil sections. The meridional velocity ratio, V_{ratio}, actual incidence angle, i, low-speed reference incidence, i_{ref}, and minimum incidence at Mach number, i_{min}, are also provided. It is believed that the negative *total* deviation (*dtotal*) indicated at the tip sections is largely a consequence of not accounting for flow turning caused by oblique shocks represented in the present model. This is discussed further in Chapter 9. Also, it should be noted that user-controlled additional deviation (d_{add}) was required to achieve satisfactory results (explained further in Chapter 5). This was not surprising given the limitations of the deviation correlations/models just described.

3.3 Loss Assessment

For application to highly transonic fans, individual loss components can be broken down into one of three broad categories, as was done by Koch and Smith, 1976:

- Profile loss – includes blade boundary layer and wake

- Shock loss – due to non-isentropic shock process in the primary (or core) flow

- Secondary loss – includes passage secondary flows and endwall interactions between annulus boundary layer and blade rows (tip gap flows and hub vortices)

Losses resulting from the interactions of a shock with the endwall boundary layer are included in the secondary losses. Further, although the losses from shock – blade boundary layer interactions were not explicitly accounted for, it is believed that the model calibration process described in Section 5.3 effectively included these effects.

Recent investigations regarding the loss mechanisms in highly transonic fans ($M_{1rel} > 1.4$) reveal that shock loss dominates and hence sets the shape of the efficiency characteristic. Denton, 1993, substantiates this in his IGTI Scholar Lecture on "Loss Mechanisms in Turbomachines." Further, it appears that in many cases, the *profile* loss remains approximately

37

constant over the working range of highly transonic blade sections. A possible explanation was provided in the previous section. Two recent examples are the work of Bloch, et al., 1999, and Konig, et al., 1996, already discussed in Section 2.1.

Based on the works just discussed and the recent investigation, the relative magnitudes of the profile, shock, and secondary loss were qualitatively assessed relative to each other and are shown schematically in Figure 3 - 2 for an airfoil section near the blade tip. For designs with
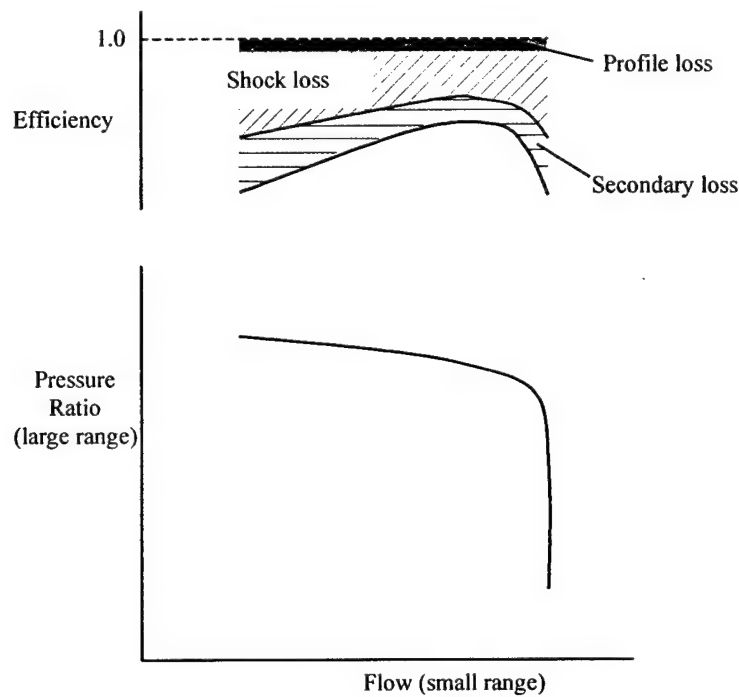
Figure 3 - 2 Approximate loss source distribution in highly transonic compressor blade sections (tip $M_{1rel} > 1.4$)

$M_{1rel} > 1.4$, the shock loss can be an order of magnitude greater than the profile loss. As the tip loads up, both the shock loss and secondary loss increase. As backpressure increases, the shock moves upstream, becoming more normal to the flow and further detached from the leading edge. This is discussed further in Chapter 4. As previously mentioned, the profile loss remains relatively constant.

38

As for the deviation angle assessment, Equation (A-11), is repeated below and each relative total pressure loss coefficient term is discussed.

$$\varpi = \left(\varpi_{min} + \varpi_M + \varpi_{tip} + \varpi_{hub}\right)\left[1 + \left(\frac{i - i_{min}}{W}\right)^2\right] \qquad \text{(A-11)}$$

Profile loss (blade section boundary layer and wake) is contained in the ϖ_{min} term, determined using the method of Koch and Smith, 1976. As discussed in Appendix A, their method is still regarded as one of the most complete, as it accounts for actual momentum thickness and shape factor (boundary layer thickness divided by momentum thickness) assuming a fully turbulent boundary layer. In the present work, a nominal trailing edge thickness of one percent of chord was used.

The ϖ_M term contains an estimate of the shock loss. As has been mentioned, this was a key improvement area, discussed in detail in the next chapter. The original method was based on the "simple flow model" of Miller, Lewis, and Hartmann (MLH), 1961. As shown in Figure 3 - 3, they assumed a single, attached shock, normal to the mean camber line in a blade passage (this provides a consistent approach for locating point B). The shock loss was calculated for the average of the Mach numbers at points A and B (Figure 3 - 3). The Mach number at A was taken as M_{1rel}, while the elevated Mach number at B was determined from Prandtl-Meyer analysis. To estimate the suction surface turning up to B, Hearsey, 1994, assumed a DCA profile and leading edge thickness of 5% of $(t/c)_{max}$. Given: (a) improvements in the design of highly transonic machines, (b) discussion on shock structure and control in Section 2.3, and (c) the need to improve off-design performance estimation, the MLH model was found to be inadequate for the present work.
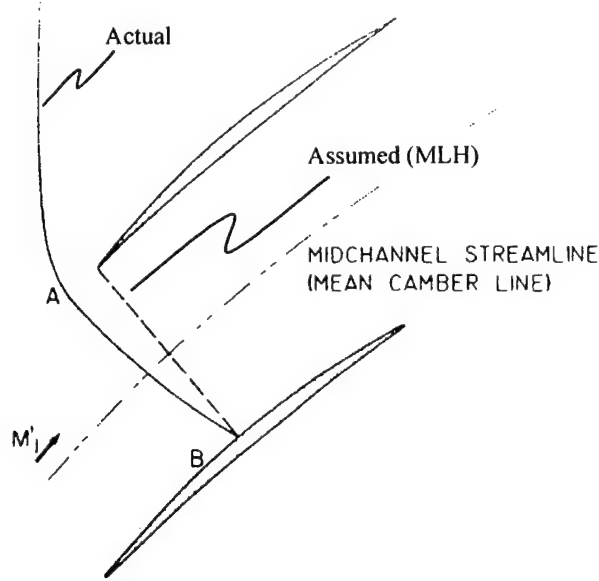
Figure 3 - 3 Passage shock configuration for estimating shock losses (Miller, et al., 1961)

The effects of secondary loss are accounted for in the last two terms (in parentheses) of Equation (A-11). Hearsey, 1994, estimated these using an increment of minimum loss that included the effects of spanwise mixing (cubic term involving radii):

$$if\ r > r_{mid}: \quad \varpi_{tip} = \varpi_{min} TLOSS\left[2.0\frac{r - r_{hub}}{r_{tip} - r_{hub}} - 1.0\right]^3 \quad (3 - 2a)$$

$$if\ r < r_{mid}: \quad \varpi_{hub} = \varpi_{min} HLOSS\left[1.0 - 2.0\frac{r - r_{hub}}{r_{tip} - r_{hub}}\right]^3 \quad (3 - 2b)$$

Parameters TLOSS and HLOSS are user-controlled. While admittedly over-simplified, this approach does allow the influence of secondary effects along the blade span away from the endwalls. Both hub and tip loss increments were used in the calibration of the streamline curvature model to the two-stage machine represented in the present study. That calibration is discussed in Chapter 5.

A well-known feature not included in the ϖ_{tip} determination is the increase in tip loss with loading, demonstrated in Figure 3 - 4, taken from Lakshminarayana, et al., 1985. The figure shows the loss contours very near the trailing edge of a low-speed axial compressor rotor at a design ($\varphi = 0.56$) and a highly loaded ($\varphi = 0.5$) condition. The effects of spanwise mixing are clearly shown. Note that the loss is approximately doubled at the highly loaded condition, Figure 3 – 4b, (relative to the design condition, Figure 3 – 4a) at all tip radii indicated in Figure 3 - 4. For example, at 96% span (indicated by dashed line in Figure 3 - 4), the passage-averaged loss coefficient for the highly loaded condition is approximately $0.12 - 0.13$, while at design, it is closer to 0.07. These data, along with results from the work of Thompson, et al., 1998, were used to develop a tip loss modifier based on loading. The Thompson results were obtained on the same two-stage, high-performance machine used in the present study.
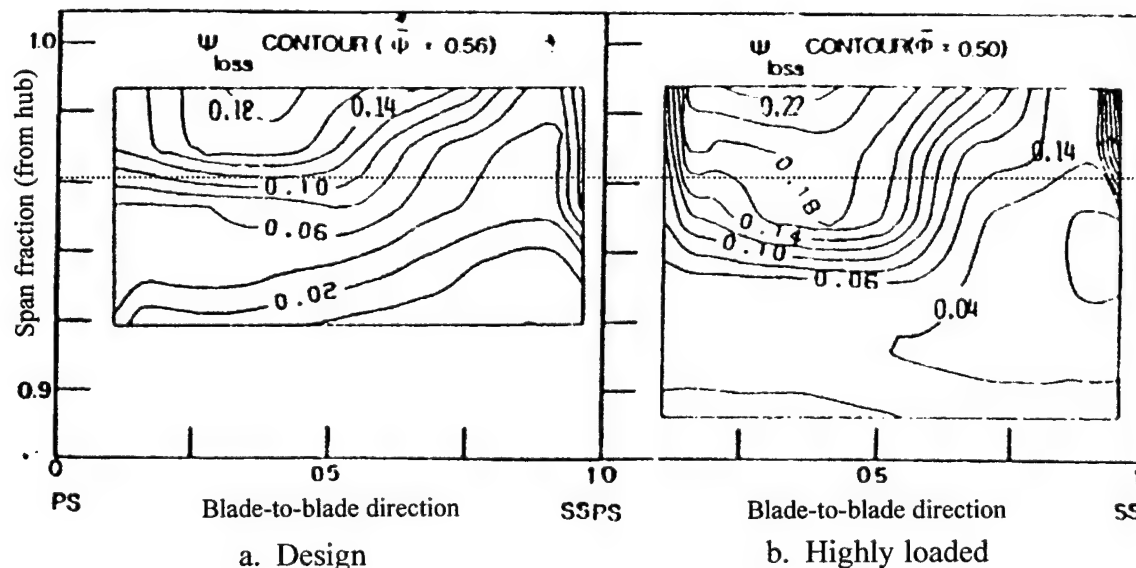
Figure 3 - 4 Contours of tip relative total pressure loss coefficient near rotor trailing edge (Lakshminarayana, et al., 1985)

A simple approach was taken to include the effects of increased loading (turning) on tip losses. As indicated in Equation (3-3), a parabolic increase with incidence angle was used as a modifier to the original tip loss model, Equation (3-2a):

$$\varpi_{tip} = \varpi_{min} TLOSS \left[2.0 \frac{r - r_{hub}}{r_{tip} - r_{hub}} - 1.0 \right]^3 \left[1.0 + \frac{(i - i_{min})^2}{(i_{stall} - i_{min})^2} \right] \qquad (3 - 3)$$

Incidence angle was used because it was easily bounded; i_{stall} and i_{min} are known in the Hearsey method. Further, a SLCC solution check at the peak efficiency and near-stall operating conditions of the two-stage fan showed that at near-stall, tip section incidence was 1-3 degrees higher, while deviation essentially remained constant. This check helped confirm $(i - i_{min})$ as an indicator of increased loading. Using Equation (3-3), tip section loss coefficients approximately doubled (over those predicted by Equation 3-2a) when operating at near-stall versus peak efficiency conditions. Given the evidence regarding tip loading effects, this trend appeared quite reasonable (see Figure 3 - 4).

The increment in loss at actual incidence (off-design) and Mach number was originally accounted for through the parabolic term in brackets in Equation (A-11). The W in (A-11) is a "width" which specifies the working range of the section. This is a common approach taken in streamline curvature methods to achieve a more realistic loss "bucket" shape (see for example, Cetin, et al., 1987). It is well known that the loss characteristic "squeezes" down as Mach number is increased (see Figure 3 - 5). Further, for airfoil profiles common to transonic blades (sharp LE and low camber), the incidence at which minimum loss occurs, i_{min}, increases with increasing Mach number. This is clearly shown in Figure 3 - 5(d) and Figure 3 - 6.

42

(a) C.4 Circular-arc blade. Camber angle, 25°; maximum-thickness ratio, 0.10; solidity, 1.333; blade-chord angle, 42.5° (ref. 40). (b) C.4 Parabolic-ard blade. Camber angle, 25°; maximum-thickness ratio, 0.10; solidity, 1.333; blade-chord angle, 37.6° (ref. 40).

(c) Double-circular-arc blade. Camber angle, 25°; maximum-thickness ratio, 0.105; solidity, 1.333; blade-chord angle, 42.5° (ref. 40). (d) Sharp-nose blade. Camber angle, 27.5°; maximum-thickness ratio, 0.08; solidity, 1.15; blade-chord angle, 30° (ref. 205).

Figure 3 - 5 Effect of inlet Mach number on loss characteristic of cascade blade sections (NASA SP-36, 1965)
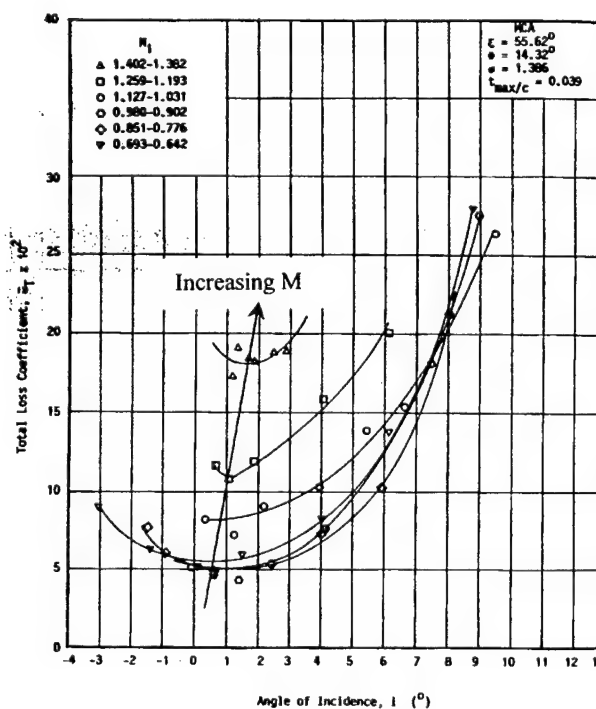
Figure 3 - 6 The variation of total losses with incidence at 10% span (Cetin, et al. 1987)

43

Figure 3 - 7 schematically demonstrates the approach used by Hearsey, 1994. A low-speed range is set by i_{stall} and i_{choke}, both determined as functions of camber and $(t/c)_{max}$. This range is then adjusted based on inlet relative Mach number and incidence to determine the actual width, W.

Two changes were made in off-design loss estimation to make the correlations more generally applicable to modern, transonic designs. First, the decrease in working range with increased Mach number was incorporated in the new shock model discussed in Chapter 4. Thus, for supersonic blade sections, the parabolic term in Equation (A-11) was not used. Second, the increase in i_{min} with Mach number was observed to be too large (as high as 15 degrees), even for subsonic airfoil sections. Dunham, 1996 also noted the poor prediction of minimum loss incidence angle from the SP36 correlations.
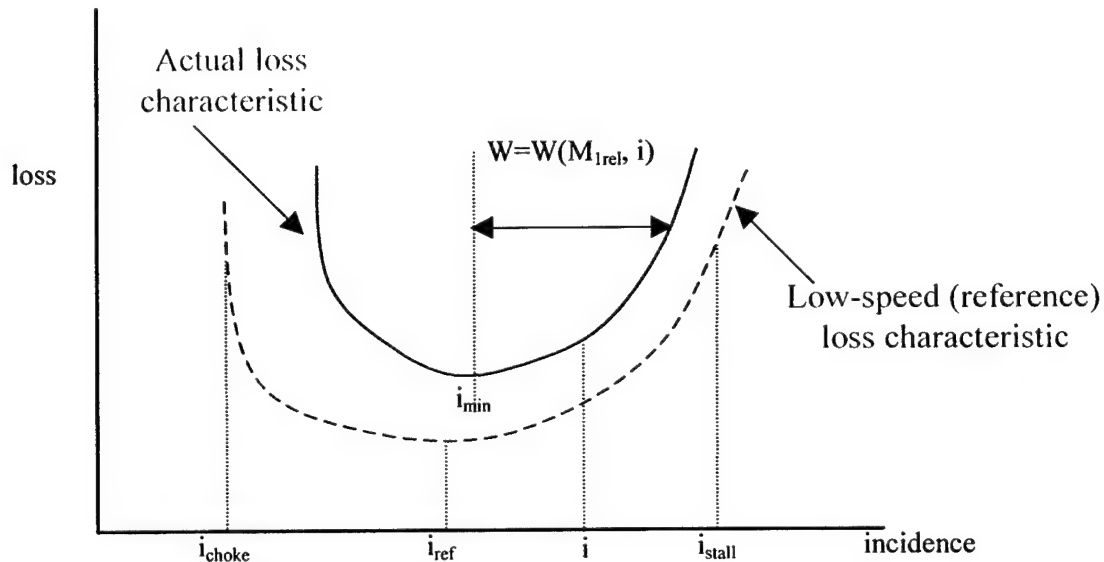
Figure 3 - 7 Hearsey approach for determining actual section loss characteristic

Consequently, a user-controlled factor was applied to the determination of i_{min}:

$$i_{min} = i_{ref} + \theta \, f(M_{1rel}) \, factor \qquad\qquad (3-4)$$

A value of 0.5 for *factor* was found to bring the minimum incidences more in line with observed values. This effectively lowered the section i_{min} values anywhere from 20-40% as determined by Equation (3-4). As an example, Table 3 - 1 (and 3 - 2 to be presented below) provides i_{min} section values for rotor one of the present application obtained with *factor* = 0.5.

Comparison of these minimum incidence values with those indicated in Figures 3-5 and 3-6 is favorable. More applicable to the present work are the results reported by Law and Puterbaugh, 1988, on a high-speed rotor with tip relative Mach numbers of 1.6. At design, blade section incidences at minimum loss on that machine ranged from 5 - 7 degrees, climbing as high as 10 degrees at off-design conditions (80% Nc). Again, these results add credence to the i_{min} predictions shown in Tables 3-1 and 3-2. Finally, as will be seen in Chapter 4, i_{min} is a key parameter in the new shock model – accurate estimation of this parameter is essential.

As with the deviation discussion, Table 3 - 2 is provided as a means to compare relative magnitudes of the various loss coefficient components. The same peak efficiency flow condition was simulated, and the inlet relative Mach number, M_{rel}, Mach number just upstream of the LE shock system, M_{elev}, and i, i_{ref} and i_{min} are also provided. The w_{corr} represents the off-design "correction" term in brackets, Equation (A-11), discussed above. The dominance of the shock loss, w_m, is evident in the outer 50% span. Note that unlike the deviation prediction, no additional loss (w_{add}) was used. The negative increments in the hub sections, w_{hub}, were used to offset unreasonably high loss estimates in this region, discussed further in Section 5.3. It should be further noted that the results presented in both Tables 3-1 and

45

Table 3 - 2 Sample SLCC output showing loss coefficient (w) components

r	Mrel	Melev	i	Iref	imn	wmin	wm	wtip	whub	wcorr	wadd	wtotal
4.618	0.744	0.744	-4.039	6.425	9.976	0.160	0.000	0.000	-0.128	5.122	0.000	0.164
6.006	0.871	1.328	0.090	4.172	8.435	0.129	0.096	0.000	-0.058	1.000	0.000	0.168
7.048	0.977	1.323	2.246	2.918	7.526	0.106	0.082	0.000	-0.024	1.000	0.000	0.164
7.910	1.067	1.352	3.534	2.197	6.785	0.087	0.039	0.000	-0.009	1.000	0.000	0.118
8.658	1.148	1.395	4.422	1.877	6.047	0.071	0.027	0.000	-0.002	1.000	0.000	0.096
9.327	1.220	1.436	5.132	1.764	5.276	0.059	0.031	0.000	0.000	1.000	0.000	0.089
9.936	1.286	1.476	5.611	1.736	4.575	0.050	0.037	0.000	0.000	1.000	0.000	0.087
10.501	1.346	1.515	5.876	1.723	4.031	0.044	0.048	0.000	0.000	1.000	0.000	0.092
11.029	1.402	1.529	6.120	1.727	3.605	0.038	0.060	0.001	0.000	1.000	0.000	0.099
11.527	1.453	1.547	6.251	1.720	3.248	0.033	0.081	0.005	0.000	1.000	0.000	0.120
12.001	1.501	1.568	6.241	1.692	2.949	0.029	0.105	0.014	0.000	1.000	0.000	0.149
12.455	1.546	1.592	6.236	1.675	2.730	0.027	0.130	0.029	0.000	1.000	0.000	0.186
12.890	1.588	1.616	6.226	1.667	2.544	0.025	0.152	0.051	0.000	1.000	0.000	0.229
13.311	1.628	1.641	6.181	1.660	2.364	0.024	0.170	0.083	0.000	1.000	0.000	0.278
13.719	1.665	1.665	5.953	1.644	2.176	0.024	0.181	0.154	0.000	1.000	0.000	0.359

Radii in inches

All angles in degrees

3-2 were generated with all of the new modifications implemented, including the new shock model described in the next chapter.

3.4 Blockage Assessment

Aerodynamic blockages arise from boundary layers, secondary flows, and resulting interactions. For accurate velocity prediction, annular (endwall) and radial blockage should be considered. Results from the present two-stage application indicated that a 10 ft/s error in the estimate for rotor inlet meridional velocity (approximately 1% at design conditions) produced about a 0.3-degree change in incidence angle. This change in incidence manifested itself most significantly as a change in predicted relative total pressure loss coefficient of about 0.007. The impact of this change is demonstrated in Chapter 5.

The SLCC approach used here contained provisions for including effects from both annular and endwall blockage. An estimate for displacement thickness, δ^*, was used to reduce the actual tip casing to account for the mass flow deficit due to endwall boundary layer. The method for determining δ^* up to the first rotor leading edge of the two-stage fan represented here is described in Chapter 5. Through the fan, wall boundary layer blockage estimates were obtained from the fan designers (Steenken, 2000) and used as given inputs.

With the exception of tip leakage vortex effects, no radial blockage estimates were included in the present investigation. The deviation and loss correlations developed from cascade data include the effects of blade metal and boundary layer blockages. However, additional blockage related to secondary flow effects (most notably tip leakage) needed to be included. As shown in the next chapter, the combination of blockages due to annulus wall boundary layer and tip leakage vortex provided for reasonable estimation of the inlet radial velocity profile. Improvements in this area are still needed.

47

3.5 Summary Results from SLCC Assessment

Below is a summary of how the SLCC models and correlations were used/modified in the present investigation. In general, the changes were made to allow for improved applicability to modern, transonic designs:

- With the exception of δ_M, the deviation component due to increased Mach number, all terms of Equation (A-10) were used to estimate the blade section exit flow angle. The deviation model needs substantial improvement.

- All components of Equation (A-11) were included in the loss estimation. The changes implemented include:

  - An improved, physics-based shock loss model for design *and off-design* conditions – see Chapter 4.

  - Incorporation of loading effects on the tip loss (secondary) model – see Equation (3-3).

  - Removal of the off-design "correction factor" – parabolic term of Equation (A-11) – for high-speed blade sections – this due to the improved shock and secondary flow models.

  - Improved estimation of the minimum loss incidence angle (at actual Mach number), i_{min} – see Equation (3-4).

- The modification to the i_{min} calculation indirectly impacted the deviation angle determination through δ_{va}, the deviation due to axial velocity ratio. Generally, this was a small effect.

- A combination of annulus and tip radial blockages were included in the present work to more accurately predict the radial velocity profile at the R1 entrance – see Chapter 5 for details.

4. An Improved Engineering Shock Loss Model

4.1 Why Improve The Shock Loss Model?

As previously presented (Sections 2.3 and 3.3), much of the loss associated with modern transonic fan designs is attributed to the non-isentropic shock process. Recent investigations (Bloch, 1999; Konig, et al., 1996) have shown that the efficiency characteristic of highly transonic blading is predominantly determined by shock loss. This is not surprising given the well-known total pressure loss variation with Mach number across a normal shock, shown in Figure 4 - 1. Denton, 1993, suggests that at inlet relative Mach numbers greater than 1.4 ($M_{1rel} >$ 1.4), shock loss dominates the boundary layer loss (even considering the shock-induced thickening of the boundary layer). He offers the modeling success of Freeman and Cumpsty, 1989, as further evidence of the dominance of shock loss.

Thus, successful engineering representations of transonic fan performance must include an accurate shock loss model. Further, if the representation is to be used for off-design predictions, the shock model must adequately account for changes in shock structure and
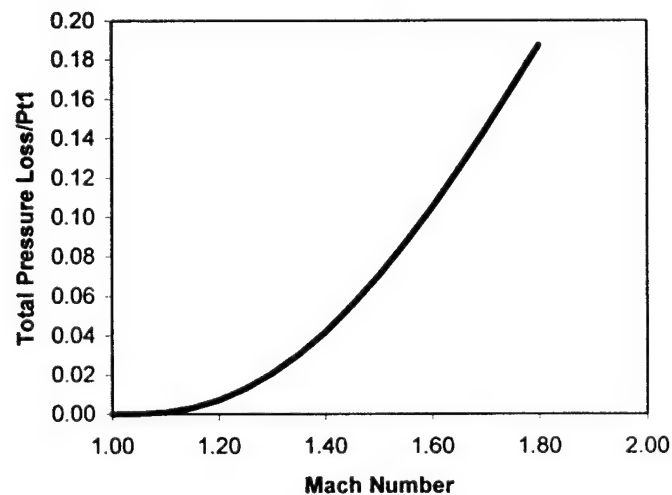
Figure 4 - 1 Variation of total pressure loss across a normal shock wave ($\gamma=1.4$)

49

position with *local blade section* operating condition and shape (see Figures 2-13 – 2-15). This has *not* been the case regarding shock models in the open literature. A simplified model, based on the method of Bloch, 1999, was developed to meet the above criteria.

4.2 Shock Loss Model

The shock loss model is an improved representation of the physical process, developed specifically for off-design performance predictions. The method of Bloch, 1999, 1996 (modified Moeckel, 1949), provided the basis for the present model. Details of the Bloch-Moeckel approach are described in Appendix B – modifications to this approach are the focus of the following two sections. The modifications were made to be consistent with the: (a) "sophistication level" of loss estimation in the SLCC (see review of method in Chapter 3), and (b) proposed TEACC application (Chapter 7) – computational efficiency (low density grid) and minimal geometry specification.

4.2.1 Assumed Shock Structure and Location

Prediction of off-design shock losses for streamline curvature methods requires a priori knowledge of the shock structure and Mach number. Figure 4 - 2 schematically shows the assumed shock structure, consistent with the discussion in Section 2.3. Mach number is known through application of the SLCC. The method of Moeckel, 1949 (modified slightly by Bloch, 1996), was used to determine the shape of the detached leading edge shock and detachment distance. The method requires specification of M_{1rel} and blade leading edge radius (LER), and application of continuity between the shock vertex and sonic point (see Appendix B).

As suggested in Figure 4 - 2, shock structure is assumed to be known at three blade section operating conditions – near-choke (NC), peak efficiency (PE), and near-stall (NS). Note the similarity to the shock systems shown in Figure 2 - 15. The original shock model, discussed

in Section 3.3, is included for comparison. The incidence angles at these conditions are known

through application of the SLCC. A dual-shock structure was assumed at the peak efficiency

(minimum incidence) operating point. At this condition, the leading edge detached shock is at its

maximum obliqueness, followed immediately by a normal passage shock. The remainder of this

section describes the methods used to define the shock structure at the NC and NS conditions.
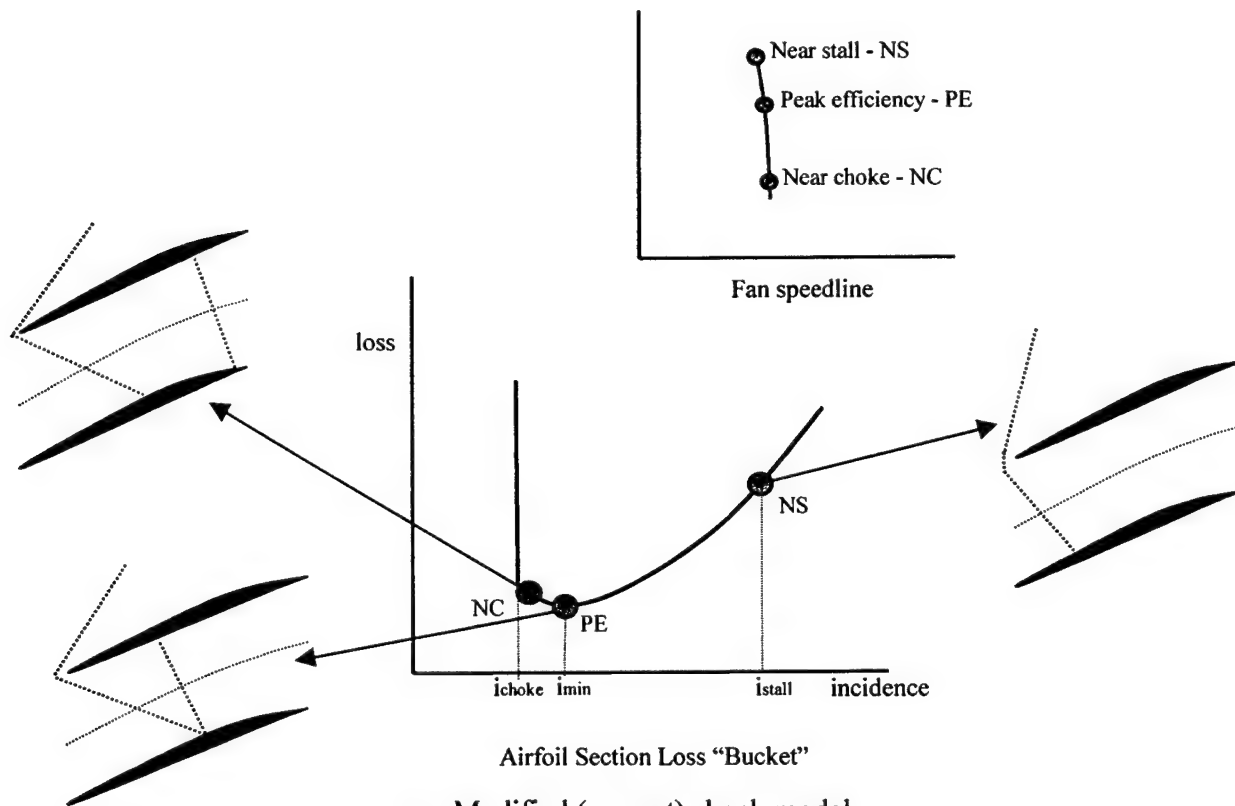
a. Modified (current) shock model
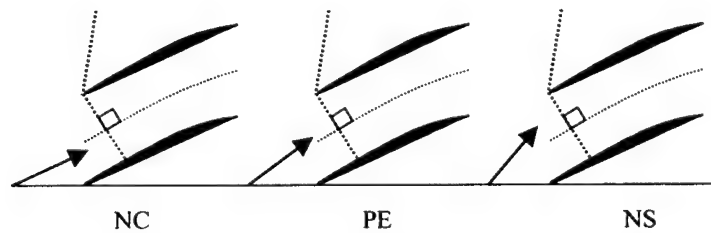
b. Original shock model (Miller, et al., 1961)

Figure 4 - 2 Assumed shock structure at different operating conditions
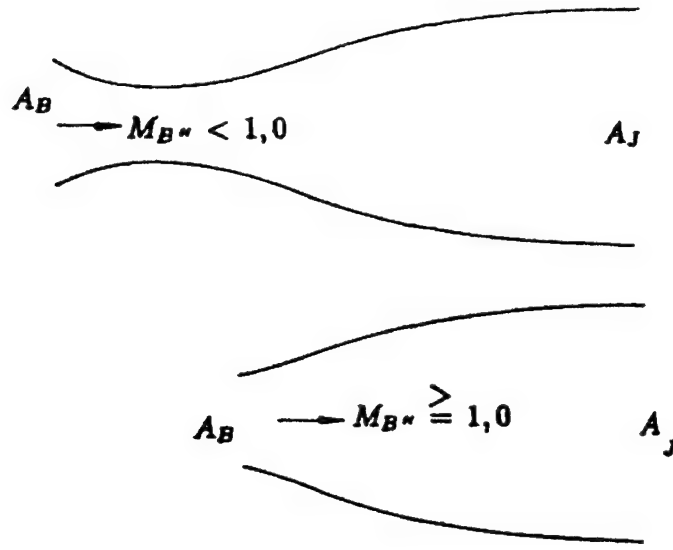
Figure 4 - 3 Assumed blade passage contours downstream of leading edge shock at near-choke operating condition (Konig, et al., 1996)

At near-choke, the method of Konig, et al., 1996 was used to estimate the Mach number directly upstream of the second shock (assumed to be at the trailing edge of the passage). In the method, substitute contours (see Figure 4 - 3) replace the actual flow path in the blade passage. By comparing computational and measurement data obtained on eight cascades with many blade shapes (including MCA, wedge, and precompression), the following exit-to-entrance area ratio equation was established (Konig, et al., 1996):

$$\frac{A_J}{A_B} = 0.499 M_{2s} + 0.501 + C_{ar} \qquad (4 - 1)$$

where: $C_{ar} = 0.0774$ for MCA or wedge sections
$C_{ar} = 0.0351$ for precompression sections

To simplify for the present work, if the Mach number behind the first shock, M_{2s} ($M_{B''}$ in Figure 4 - 3), is subsonic, then the area ratio defined by Equation (4-1) was assumed to be the critical area ratio, A_J/A^* (i.e., $M_{2s} = 1.0$). The $M_{2s} = 1.0$ assumption introduced negligible error,

52

as the existence of the downstream second shock must imply a reacceleration to supersonic velocity. This is explained physically by thickening of the boundary layer through shock-boundary layer interaction. If M_{2s} is supersonic, then from compressible flow theory:

$$\frac{A_B}{A^*} = \frac{1}{M_{2s}}\left[\frac{2}{\gamma+1}\left(1 + \frac{\gamma-1}{2}M_{2s}^2\right)\right]^{\frac{\gamma+1}{2(\gamma-1)}} \tag{4-2}$$

and A_J/A^* equals the product of Equations (4-1) and (4-2). Either way, with the critical area ratio known, Equation (4-2) must be solved iteratively (for A_J/A^*) to obtain M_3, the Mach number just upstream of the second shock when it is positioned at the trailing edge of the passage.

At near-stall conditions, as shown in Figure 4 - 2, the shock structure was assumed to be a single, normal, *detached* shock. While the mechanism for changing from a dual-shock to single shock is understood – the second shock moves upstream due to increasing backpressure, eventually coalescing with the first – the incidence at which this transition takes place is not known (this incidence is referred to as i_{norm}). Surely, the "correct" value for i_{norm} would be a complex function of blade profile design features, operating conditions, and secondary flow interactions. The following simple representation for i_{norm} was used:

$$i_{norm} = i_{stall} - 1.0 \quad \text{(deg)} \tag{4-3}$$

Equation (4-3) merely provides a convenient and consistent way to locate i_{norm}. It is not suggested that this representation is a universal one; the method was chosen to capture the correct physical trend – increased shock strength with increased backpressure.

4.2.2 *Estimation of Shock Loss*

Precise shock loss estimation requires integration of the loss along the predicted shock system to account for Mach number and flow angle variations (see Bloch, 1999). To be

consistent with the general simplifications discussed at the beginning of Section 4.2, shock loss was estimated from single point calculations (with the exception of the bow shock portion). The choice of suitable "averages" was made by considering the flow physics. The chosen Moeckel method for approximating the shock hyperbola made the selection easier.

The angle at the shock sonic point (already known through application of the Moeckel approach) was taken as the "average" shock angle. As Figure 4 - 4 demonstrates, this simple approximation captures the physical trends and appears quite suitable. At elevated Mach numbers, the shock becomes more swept relative to the upstream flow – the average shock angle decreases. Note also the decreased detachment distance at elevated Mach number, as expected. Figure 4 - 4 also indicates the isentropic Mach angle, MA, at the two conditions, providing further evidence of the appropriateness of the choice for SA_{avg}. The angle must be between the Mach angle and 90 degrees.

By comparing results obtained with a normal shock, Figure 4 - 5 helps quantify the impact of using SA_{sonic} as a representative shock angle. At the peak efficiency (minimum loss) condition, the new model provides a predicted shock loss coefficient about 50% lower than a

a. M=1.2, MA=56.4 deg   b. M=1.5, MA=41.8 deg
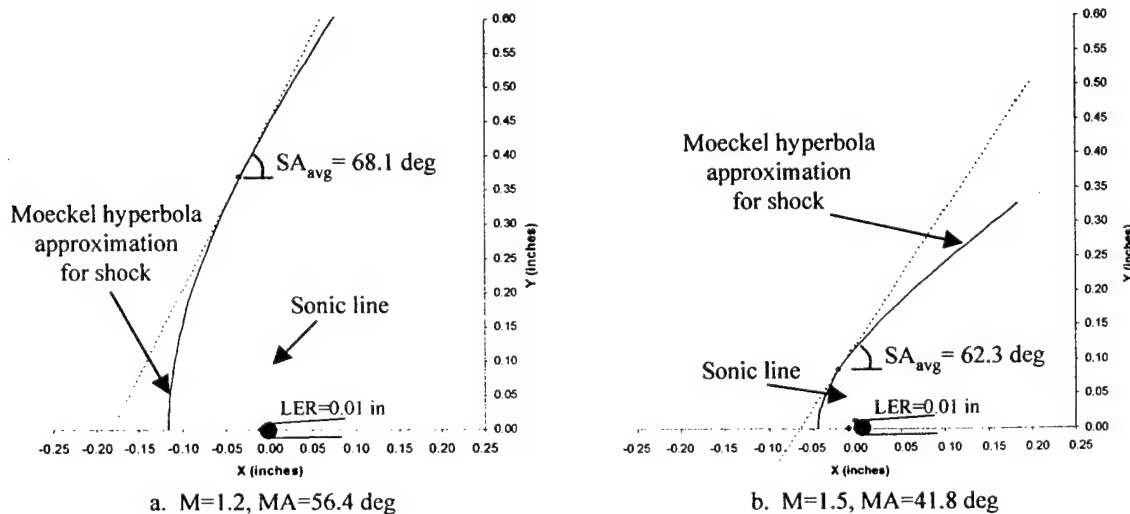
Figure 4 - 4 Use of shock angle at sonic point for loss estimation

a. LER = 0.01 inches (typical)   b. Mach number = 1.5
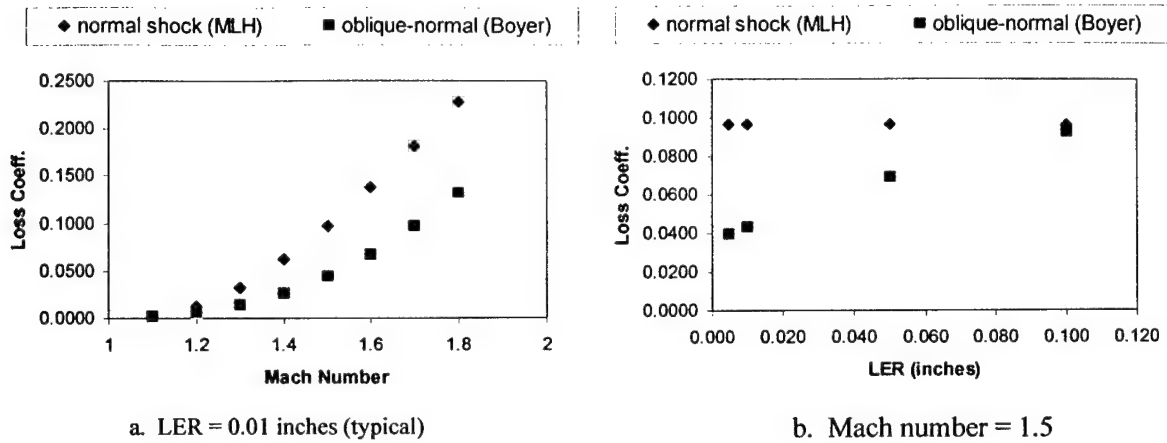
Figure 4 - 5 Impact of new shock loss model relative to normal, attached model (MLH)

normal shock assumption (Figure 4 - 5a). It should be noted that the use of SA_{sonic} effectively

removes blade leading edge radius (LER) as a player in determining the average shock angle;

i.e., for a given inlet Mach number, SA_{sonic} is set (see Equation B-4). This is not overly

restrictive for two reasons: (a) the LE radii of highly transonic airfoil sections are sharp – 0.01

inches is typical – and thus would be of second-order influence on shock shape, and (b) as Figure

4 - 5b indicates, the *effect* of increased LER (at a given M) is captured by including an estimate

for detached bow shock loss. Note that in Figure 4 - 5b, bow shock loss increased from 0.004 at

a LER = 0.01 (about 10% of shock loss) to 0.057 at LER = 0.1 inches (over 60% of shock loss).

The MLH model does not include any detached bow shock effects.

Approximation of the elevated Mach number at the shock entrance, M_{1s}, was obtained

using the existing approach in the SLCC (Miller, et al., 1961), discussed in Section 3.3. This

approach is quite suitable, given that transonic blades are very thin and have low suction surface

camber (in precompression cases, "reverse" camber), resulting in peak suction surface Mach

numbers not much greater than M_{1rel}. For precompression sections, the SLCC was modified to

use $M_{1s} = M_{1rel}$ at the outermost tip section, then smoothly increased (linearly) to an elevated

Mach number as predicted by Prandtl-Meyer analysis where the precompression geometry blends into the more traditional convex suction surface. The effect can be seen in Table 3 - 2 by comparing the M_{rel} and M_{elev} values. As illustrated in Figure 2 - 13b, using M_{1rel} as the entrance shock Mach number is quite consistent with recent observations. Indeed, the reason for choosing a precompression airfoil is to reduce shock losses by effectively reducing the average Mach number at the shock entrance (Tweedt, 1988; Parker and Simonson, 1982).

The remainder of this section discusses the estimation of shock losses in three regions – at i_{min}, and incidence angles greater than and less than i_{min}. Recall that the shock structure is assumed known at three blade section operating conditions – near-choke, peak efficiency, and near-stall (Figure 4 - 2).

At i_{min}, the leading edge shock is at its maximum obliqueness. The average total pressure loss across the first shock is computed from oblique shock theory (John, 1984), evaluated at SA = SA_{sonic}:

$$\frac{P_{02}}{P_{01}} = \left[\frac{(\gamma+1)M_{1s,norm}^2}{(\gamma-1)M_{1s,norm}^2+2}\right]^{\frac{\gamma}{\gamma-1}}\left[\frac{\gamma+1}{2\gamma M_{1s,norm}^2-(\gamma-1)}\right]^{\frac{1}{\gamma-1}} \qquad (4-4)$$

$$where: \quad M_{1s,norm} = M_{1s}\sin(SA)$$

and:

$$M_{2s} = \sqrt{M_{2s,norm}+M_{1s,\tan}}$$

$$where: \quad M_{2s,norm}^2 = \frac{M_{1s,norm}^2+\frac{2}{\gamma-1}}{\frac{2\gamma}{\gamma-1}M_{1s,norm}^2-1} \qquad (4-5)$$

56

If M_{2s} (Mach number directly behind the first shock) > 1.0, then as discussed, a second shock that is normal to the flow was assumed. Equation (4-4) can be used with SA = 90 degrees (for calculating $M_{1s,norm}$) to get the total pressure loss across this passage shock.

As the blade section loading increases ($i > i_{min}$), the passage shock moves upstream subjecting the incoming flow to a stronger shock system, increasing the loss. This effect was modeled through a smooth increase in shock angle from SA_{sonic} at i_{min} to 90 degrees at i_{norm}, given by Equation (4-3). The relationship is given by Equation (4-6) below:

$$SA = SA_{sonic} + \frac{(90 - i_{min})}{(i_{norm} - i_{min})^n}(i - i_{min})^n \qquad (4-6)$$

Figure 4 - 6 demonstrates the impact on the section loss characteristic for two values of the exponent, n, in Equation (4-6). Clearly, the value of this parameter influences the magnitude of shock loss coefficient for a given incidence angle, but regardless of the value, the general shapes (and hence, resulting predicted trends) are reasonable. Comparison of these loss characteristics with those from Cetin, et al., 1987, and Law and Puterbaugh, 1988 led to the chosen value of n = 4. In making the choice, it was assumed that the overall loss characteristic was dictated by the shock loss, consistent with the discussion presented throughout this report.

For operation at incidence angles greater than i_{min}, detached bow shock loss (due to LE bluntness) was included in the loss estimation. Bow shock loss was estimated using the method of Bloch, 1996, applied to the Moeckel hyperbola (see Equation B-9). The spatial increment for integration was chosen as the arbitrarily small value:

$$dy = \frac{y_{sonic}}{10} \qquad (4-7)$$

and the integration was stopped when:
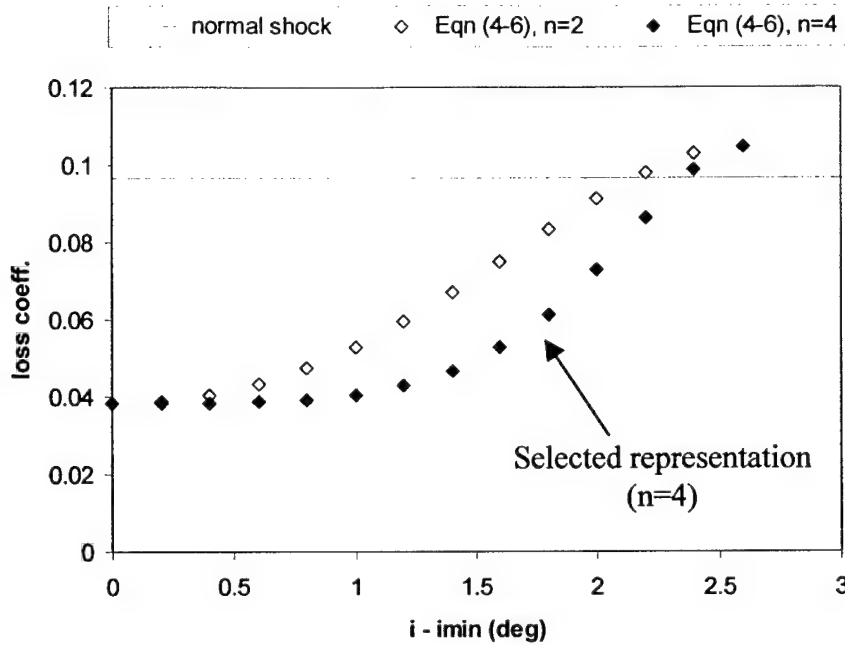
Figure 4 - 6 Impact of exponent "n," Equation (4-6), on blade section loss characteristic

$$(1.0 - \frac{P_{02}}{P_{01}}) \leq 0.0005 \qquad (4 - 8)$$

Values for y_{sonic}, the distance from the blade mean camber line to the sonic point on the

shock, ranged from about 0.2 (inches) at M=1.3 to 0.06 at M=1.7 for a LER of 0.01 inches.

These numerical integration criteria were selected to ensure that they did not bias the loss

estimation accuracy. For example, according to the analysis presented in Section 5.4, the upper

bound of integration suggested by Equation (4-8) should limit any inaccuracies in overall

efficiency prediction to less than 0.1%, well within the accuracy that resulted from overall loss

estimation. It should be noted that loss models available through the open literature do not

generally include increased loss due to bluntness – Koch and Smith, 1976, provide an example of

one that does (note that their shock model is only applicable at design conditions).

Because more of the flow passes through the strong portion of the bow shock as it moves upstream, it seems reasonable that bow shock loss would increase with incidence angle. Using the results of Bloch, 1996, the following representation was developed for the present work to approximate this increased loss:

$$\omega_{bow} = \omega_{bow} + \frac{0.015}{\left(i_{norm} - i_{\min}\right)^3}(i - i_{\min})^3 \qquad (4\text{-}9)$$

With equation (4-9), the *increment* in bow shock loss due to increased incidence when operating at near-stall (from peak efficiency) is approximately 0.015. As will be shown in Section 5.4, this impacts the adiabatic efficiency by about three percent. It should also be noted that the *overall* bow shock loss contributed 10-30% of the total loss at near-stall, dependent on section geometry and loading condition.

With conditions represented by $i < i_{\min}$, the effect of the increased strength of the second shock as it moves downstream (refer to Figure 4 - 2) was approximated by:

$$\omega_M = \omega_{M,\min} + \frac{\omega_{M,choke} - \omega_{M,\min}}{\left(i_{choke} - i_{\min}\right)^4}(i - i_{\min})^4 \qquad (4\text{-}10)$$

Figure 4 - 7 shows the smooth increase in loss coefficient obtained from Equation (4-10). The previous section presented the approach for calculating the Mach number just upstream of the second shock when it was located at the blade passage trailing edge – see Equations (4-1) and (4-2). The choice of four for the exponent in Equation (4-10) was based on a tradeoff between the following two considerations:

(a) the shape of the loss characteristic curves from the data of nine transonic designs (Cetin, et al., 1987; Law and Puterbaugh, 1988).

(b) desired rapid rise in loss with incidence angles less than i_{choke}. By definition, the incidence cannot be less than the choking incidence; however, the SLCC does not represent the physical mechanism for leading edge choke – an approximation was required.
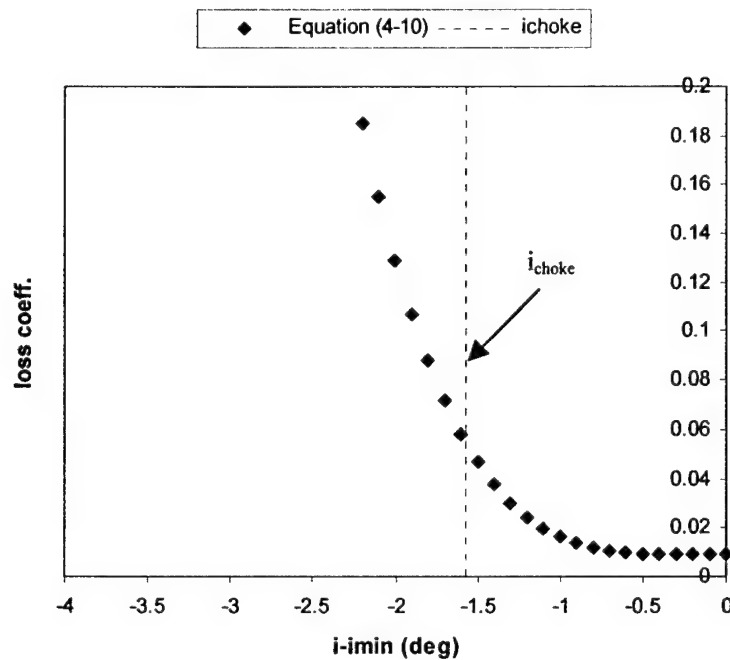
Figure 4 - 7 Blade section loss characteristic for $i < i_{min}$

4.3 Summary of Shock Loss Model

The new shock loss model, while simplified to be consistent with the overall SLC approach, is based on the known flow physics – loss is a function of *local* M_{1rel}, operating condition, solidity, LER, and blade suction surface profile. It was developed specifically with off-design performance prediction in mind. Key features of the model are summarized below.

- Dual-shock system assumed between peak efficiency and choked flow operating conditions that transitions to single, detached, normal shock as stall approached (Figure 4 - 2).

- Basic principles used to determine hyperbolic, detached shock dictated by local blade section Mach number and blade LER (Appendix B). Thus, shock shape and loss vary with radius.

- Numerical integration for detached bow shock loss included for operating conditions between peak efficiency and stall.

- Single point calculation for passage shock system loss at each blade section with:

  ➢ Shock angle at sonic point on Moeckel hyperbola taken as "average."

  ➢ Average elevated Mach number calculated from M_{1rel} and peak suction surface Mach number (for precompression tip sections, M_{1rel} is used).

  ➢ Between peak efficiency and stall, if oblique first shock and supersonic downstream conditions, second normal shock assumed.

4.4 Verification of Improved Engineering Shock Model

Verification focused primarily on answering two fundamental questions:

(a) Do the results make sense relative to the original shock loss model (Miller, et al., 1961)?

(b) Do the results represent known and assumed flow physics? Is the model an improvement?

Primarily due to previous experience, NASA Rotor 1B (Seyler and Gestolow, 1967) was chosen as the initial verification vehicle for the improved shock loss model. Table 4 - 1 summarizes key geometric and design point parameters for this single transonic compressor blade row. Performance was compared with predictions using the SLCC configured with the original and improved shock loss models, as described in the following paragraph.

Test data (Seyler and Gestolow, 1967) at 100% design corrected speed, N_c, provided the basis for comparison. Additional deviation was required by the SLCC in order to match the measured rotor mass-averaged total temperature ratio at each operating condition. The same additional deviation was applied to each of eleven streamlines specified in the simulation. This procedure provided a common basis for loss prediction comparisons between the two shock

61

Table 4 - 1 NASA Rotor 1B Design Parameters

Number blades	44
IGV/EGV	None
Blade section profile	DCA – bottom 60% MCA – top 40%
Inlet hub-to-tip ratio	0.5
Diameter	36.5 inches
Tip solidity	1.3
Tip speed	1400 ft/sec (M_{1rel} approx. 1.4)
Design corrected mass flow	215.5 lbm/sec
Design pressure ratio	1.6
Design efficiency	0.858

models. Both overall and radial performance comparisons were made at operating conditions ranging from choke to stall.

4.4.1   Overall Performance Comparisons

Figure 4 - 8 shows the overall performance comparison at 100 % N_c. As a result of the procedure outlined in the preceding paragraph, the three temperature characteristics overlap. Improvements associated with the present modifications – curves labeled "oblique-normal (Boyer)" – are evident, most notably in the efficiency characteristic. Also shown are the additional deviation curves required to match overall TR at each operating condition.

Figure 4 - 9 compares shock loss from the original and modified (present) models at two different blade sections for operating conditions consistent with Figure 4 - 8. The difference is significant, but not surprising, given the simplified MLH approach. Note the opposite trends predicted by the two methods as the blade sections approach stall. The decreasing trend predicted by the original model is not physical, but expected. As the blade "loads up" (increased incidence), the inlet relative Mach number decreases slightly, as indicated in Figure 4 - 9. With a normal shock assumption, the entropy creation would decrease roughly as the cube of (M^2-1) – Denton, 1993, consistent with the trend evidenced by the original model.
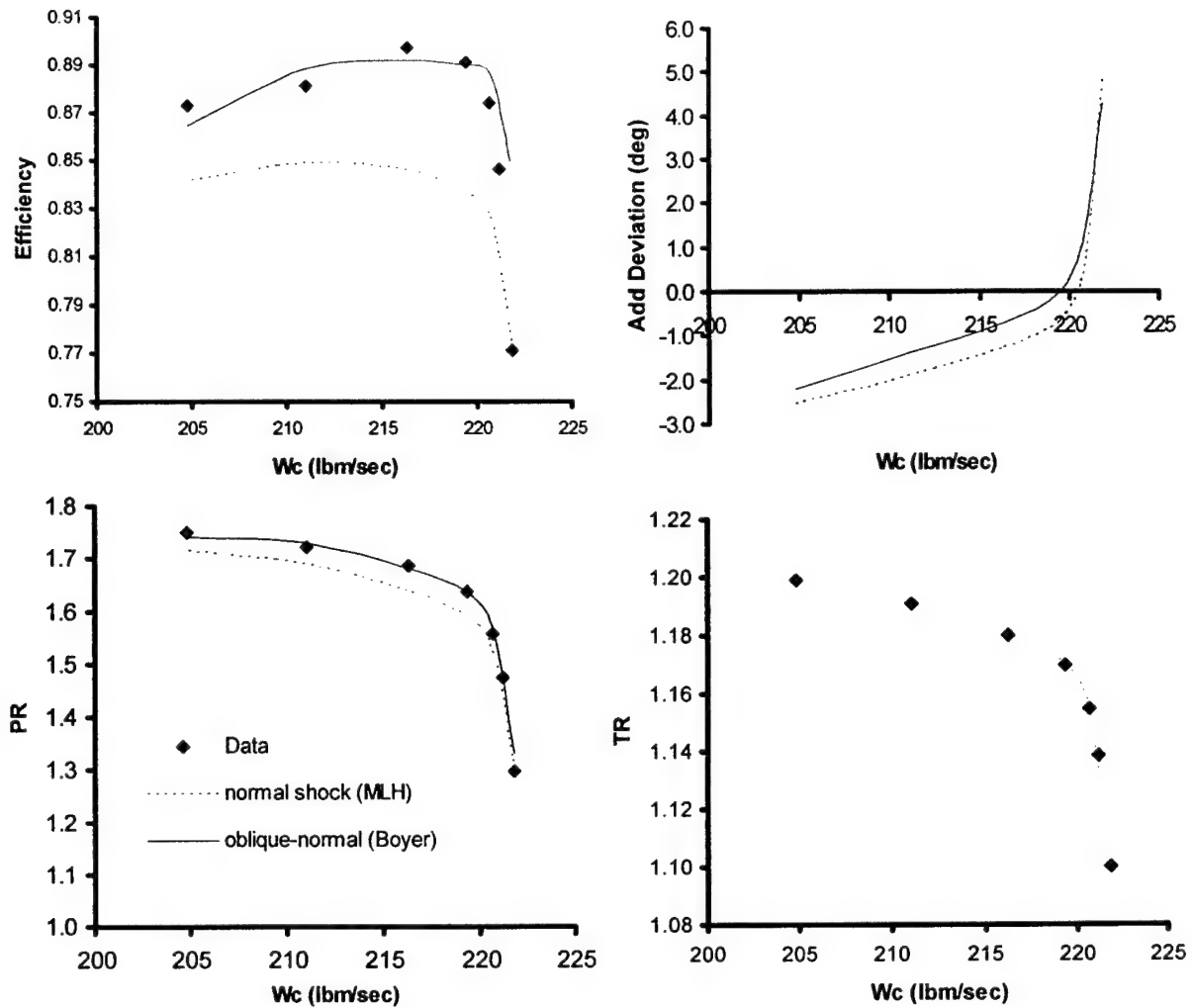
Figure 4 - 8 Rotor 1B overall performance comparison at 100% N_c

With the new model, the shock is at some oblique angle to the flow at low loading conditions, and becomes more normal and further detached as stall is approached, more than offsetting the effect of decreased Mach number. The correct trend is predicted by the new model, which indeed displays the well-known "bucket" shape. Note further that at high incidence angles (i.e., near stall), the new model predicts higher loss than the MLH – this due to the inclusion of bow shock loss due to LE bluntness. Also, as would be expected, both models predict increased shock loss at higher relative Mach numbers closer to the tip (compare loss magnitudes of Figures 4-9a and b).

63
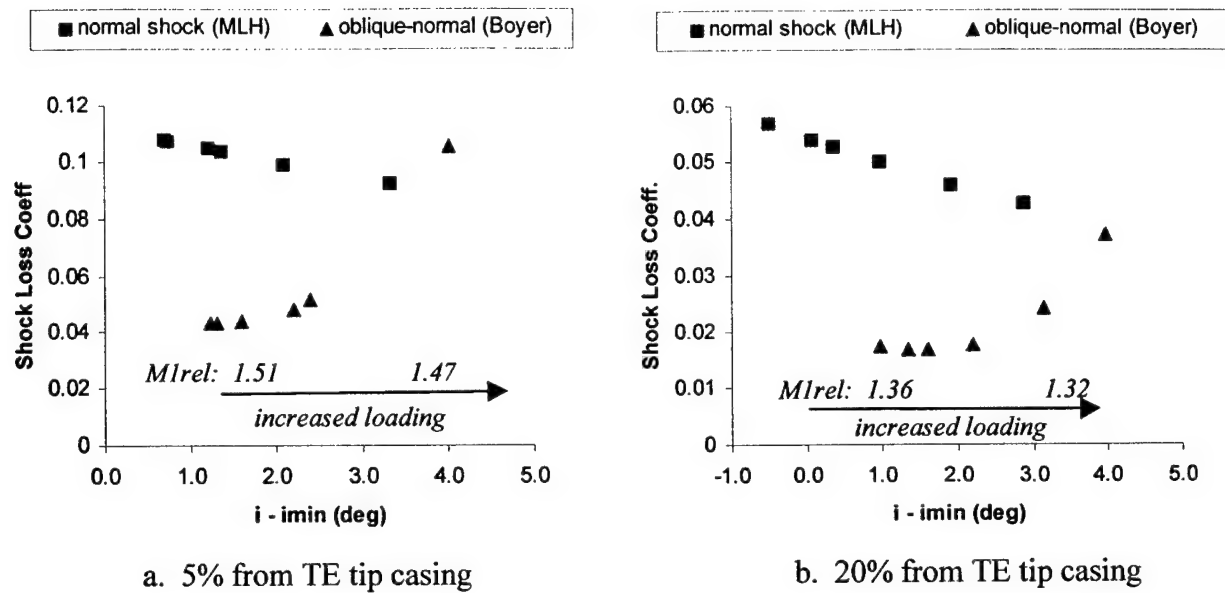
Figure 4 - 9 Blade section shock loss coefficient comparison at different loadings
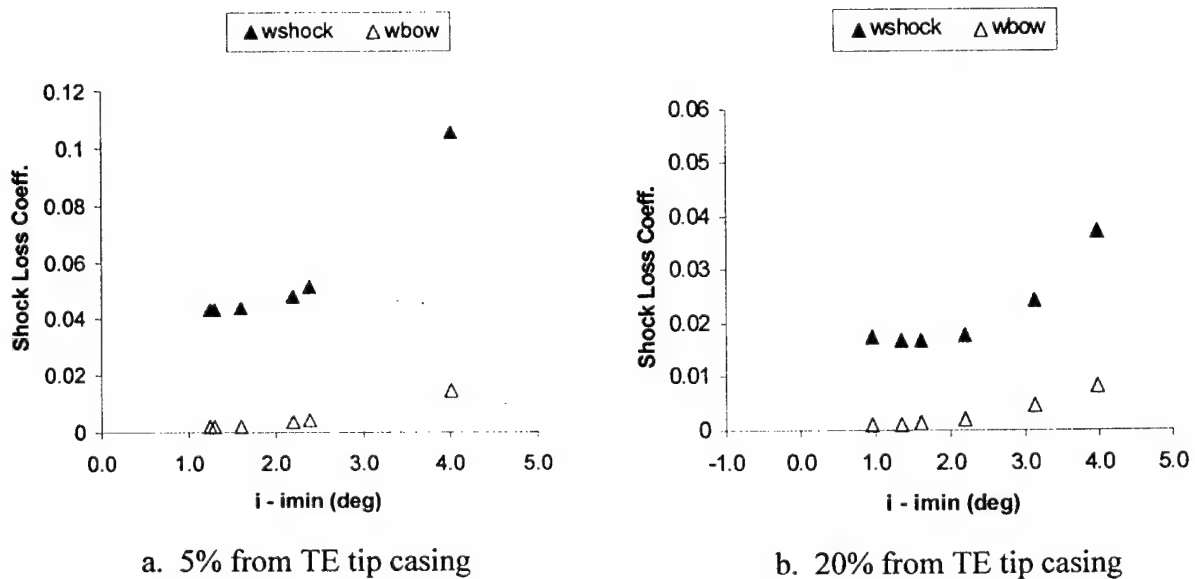
Figure 4 - 10 Prediction of loss attributed to detached bow shock

An evaluation of the detached bow shock portion of the loss characteristic is provided in Figure 4 - 10 (same two blade sections as Figure 4 - 9). The solid triangles represent the entire shock loss; the open symbols, the bow shock portion of that loss. In Figure 4 - 10a, the bow shock accounts for approximately 13% of the shock loss as the section approaches stall, while further down the span from the tip (Figure 4 - 10b), it is responsible for over 20%. Admittedly, the bow shock model is crude and requires additional validation, especially the representation of increased bow shock loss with incidence angle, Equation (4-9); however, the predicted trend is quite reasonable.

The preceding three figures and discussion answer the two verification questions posed at the beginning of this section. Clearly, the new shock model is an improvement and provides results consistent with: (a) expectations relative to the original MLH model, and (b) the known flow physics.

4.4.2 Radial Performance Comparisons

Attention is now turned to radial loss performance predictions of the SLCC and comparison to experimental data. Figure 4 - 11 shows the radial distribution of *total* loss coefficient (profile, shock, and secondary) at peak efficiency and near-stall operating conditions. The improvement with the new shock model over the entire blade span is readily apparent at both operating conditions, but most significantly in the outer regions (r >14 inches). Note that neither prediction does particularly well in the hub region of the blade, tending to over-predict the loss. This region was not a focus area of the present work. While undesirable, the relatively poor hub performance prediction is not surprising, given the limitations of the SLCC correlations discussed in Chapter 3. A somewhat redeeming feature of high-speed machines is that the outer blade span tends to be more loaded than the inner, partly because the designs usually incorporate

65

significant radial sloping in the hub region. In Rotor 1B, 63% of the total flow passes though the outer 50% of the blade, while in Rotor 4 of Law and Puterbaugh, 1988, approximately 75% of the flow passes through the outer 60% of the blade. Further discussion is presented in Sections 5.3 and 5.4.

a. Peak Efficiency   b. Near Stall
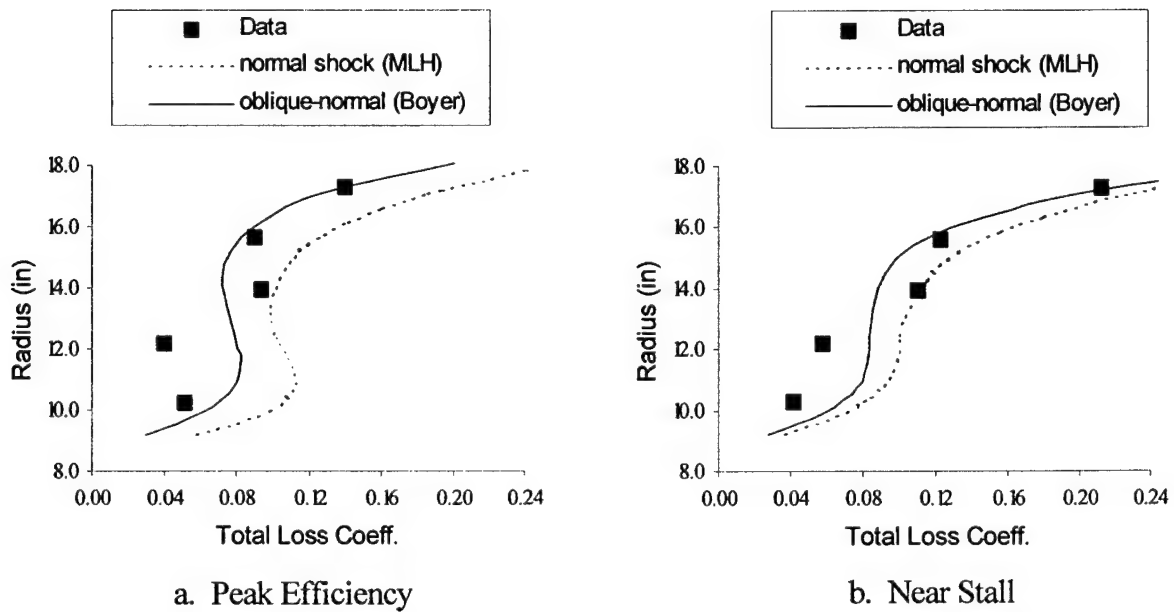
Figure 4 - 11 Rotor 1B radial loss prediction comparisons

5. Model Configuration and Calibration

This chapter provides the methodology used to configure and calibrate the streamline curvature model to represent the two-stage fan. First, a brief description of the fan and test data used in the present work is provided. Then, model configuration requirements are discussed with an emphasis on representing wall boundary layer and tip leakage effects. The model "calibration" methodology is then described. Finally, a model parameter sensitivity study is presented to obtain a quantitative analysis of required loss, deviation, and blockage accuracy.

5.1 Description of Two-Stage Fan

The test article in the present research is a two-stage, highly transonic fan design whose aerodynamic and aeromechanical characteristics are well documented with an extensive database of experimental measurements. Fan configuration has varied throughout the 15 years (and continuing) of experimental programs conducted at the Air Force Research Laboratory's Compressor Research Facility (CRF) – these include IGV/no IGV, swept/unswept, smooth tip casing/casing treatments. Recent investigations have used these data to examine: (a) inlet flow distortion and unsteady pressure loading (Rabe, et al., 1999; Hah, et al., 1998; Rabe, et al., 1995), (b) performance effects of stepped tip gaps (Thompson, et al., 1998), and inlet-distortion generated forced vibration blade response (Manwaring, et al., 1997). These works cite numerous other references based upon data from this fan.

Figure 5 - 1 provides a schematic of the test setup and fan configuration used in the present work – no IGV, unswept rotor blades, and smooth tip casing. Design parameters of the first-stage rotor (R1) are summarized in Table 5 - 1. The R1, shown in Figure 5 - 2, is a state-of-the-art, integrally-bladed disk (blisk), low aspect ratio design.
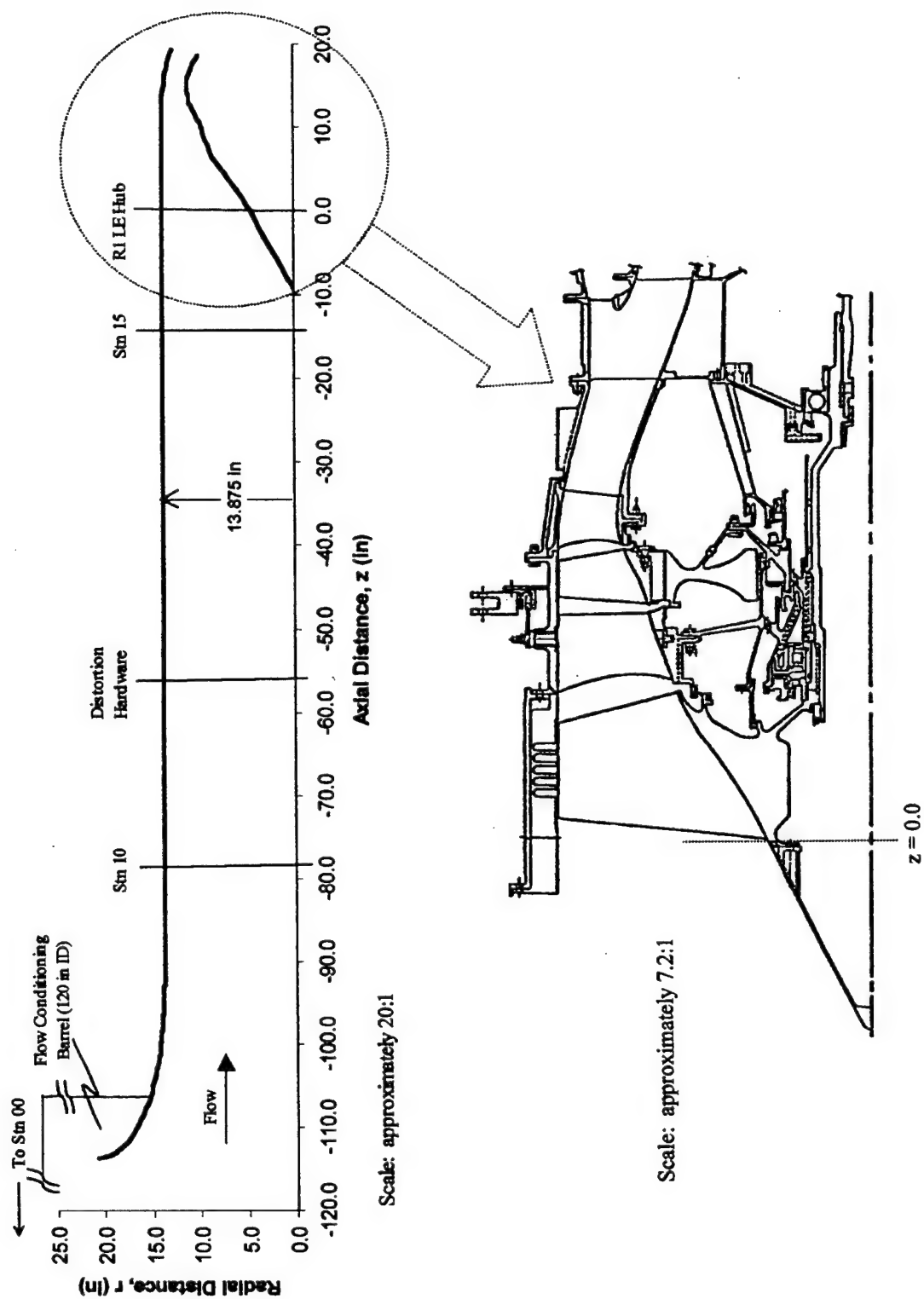
Figure 5 - 1 CRF two-stage fan schematic

68

Table 5 - 1 Design parameters of the first-stage rotor

Parameter	Value
Aspect ratio (average span/hub axial chord)	1.0
Inlet radius ratio	0.33
Tip radius (ft)	1.16
Tip solidity	1.50
Tip $(t/c)_{max}$	0.028
Tip speed (ft/s)	1609
Corrected flow (lbm/s)	158.6
Total pressure ratio	2.50
Adiabatic Efficiency	0.889
Corrected speed (rpm)	13,288

The variable first stage stator (S1) contains 41 vanes in an overlapped, tandem configuration - the forward section is fixed and the aft flap variable. The vanes of the S1 forward section are a bowed, swept design. Rotor two (R2) is a slot bladed disk containing 40 blades with tip solidity and $(t/c)_{max}$ very close to that of R1. Both rotors employ precompression tip section airfoils (see discussion in Section 2.3) over the outer 30-40% span and tailored controlled diffusion airfoils (CDA) throughout the remainder of the blade. A view looking down the stacking axis of R1 is provided in Figure 5 - 3. The precompression tip profile is clearly shown in Figure 5 - 3, as is the hub section which turns the flow approximately 50 degrees. Stator two (S2) contains 60 vanes at fixed stagger and leaned counter to the direction of rotor rotation.
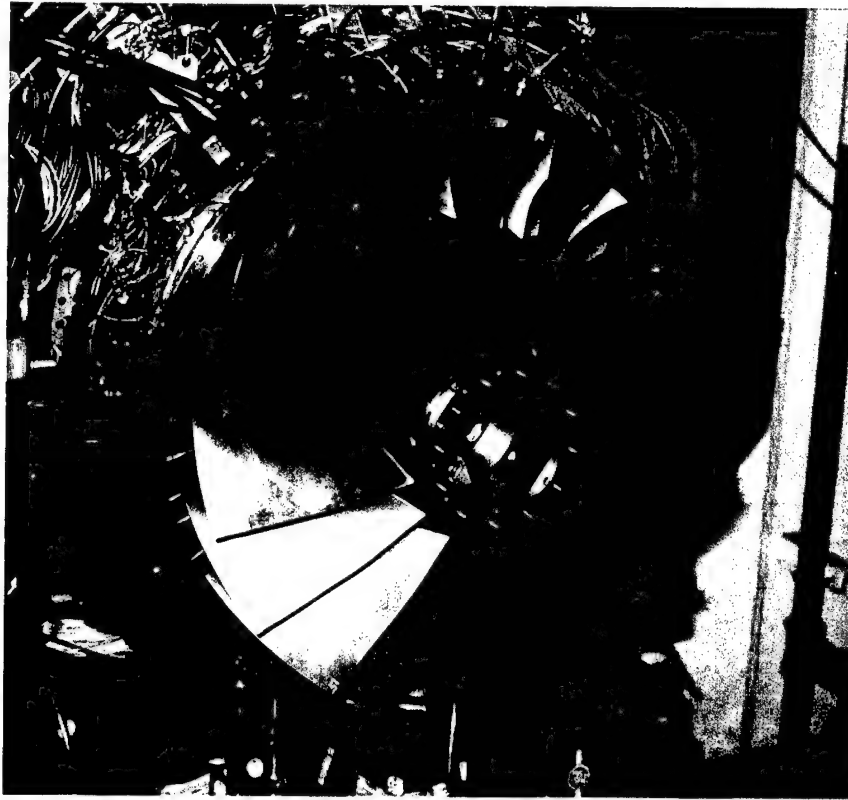
Figure 5 - 2 First rotor of CRF two-stage fan
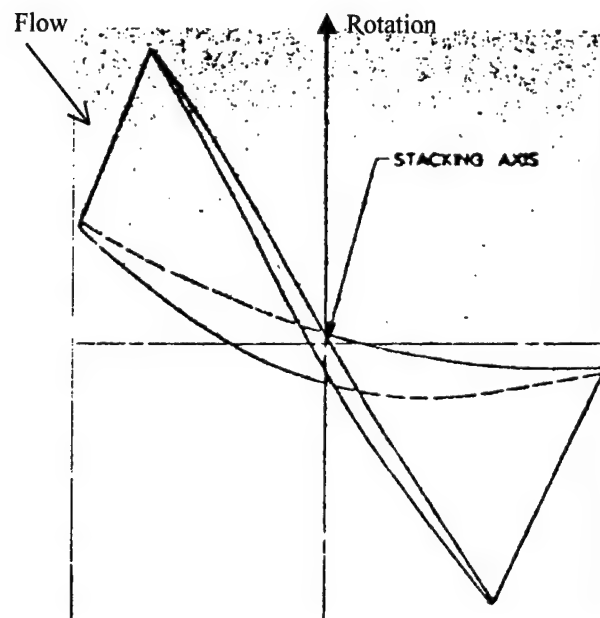
Figure 5 - 3 Radial view of R1 showing hub section and precompression tip profile

70

The fan was extensively instrumented with 600-800 individual measurements taken, depending on the test program objectives. Only the measurements most pertinent to the present work are discussed here – refer to the individual references for additional details. The station references are those used by the Compressor Research Facility.

Inlet total temperature was measured with 49 thermocouples (station 00) located in the CRF flow conditioning barrel about 13.5 feet upstream of the bellmouth inlet (see Figure 5 - 1). The bellmouth inlet (Stn 10) and distortion measurement plane (Stn 15) instrumentation are shown in Figures 5-4 and 5-5, located about 78 and 14.5 inches, respectively, upstream of the R1 hub leading edge (Figure 5 - 1). The TT00 and station 10 measurements were used to calculate bellmouth mass flow rate. The total pressure transducers at station 15 were arranged in a typical pattern to determine distortion, as recommended by SAE AIR 1420 - eight rakes with five radially distributed measurements equally spaced around the circumference. Rotor exit total pressure and temperature measurements were made at the leading edges of both stators. As seen in Figure 5 - 6 (representative of both S1 and S2), three stator vanes were instrumented at seven radial locations, approximately equally spaced around the circumference. Seven arc rakes, each containing 11 total pressure and temperature measurements (Figure 5 - 7), were used to obtain discharge measurements at 7 radial locations about one inch downstream of the stator two trailing edge. The rakes were designed to span two S2 passages to obtain wake-averaged calculations, ideal for the present application. These data, along with station 15 measurements, were used to determine overall machine performance. In all cases, area-averages were used to determine overall performance characteristics. Overall mass flow rate was calculated from venturi measurements located about 98 feet downstream of the fan. Hub and tip casing static pressure measurements were made at numerous axial locations through the fan.

MEASUREMENT		Z (in)
⬡	P static	-77.67
◎	P diff/static	-77.67
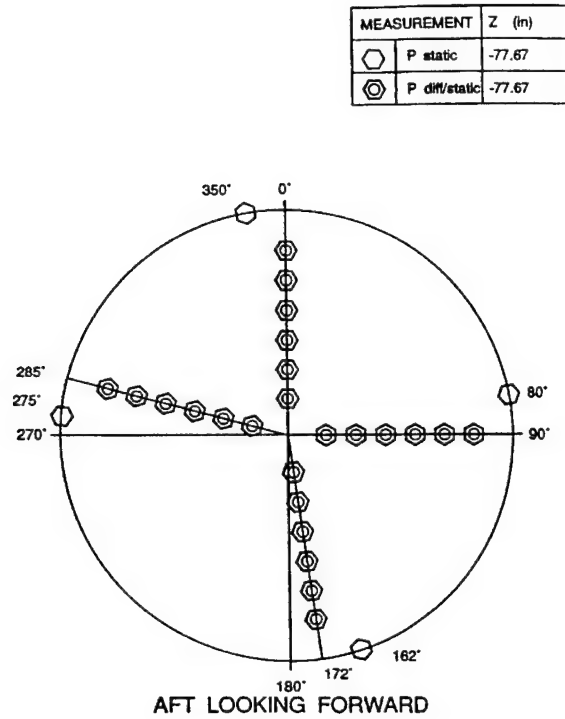
Figure 5 - 4 CRF inlet station 10 instrumentation

MEASUREMENT		Z (in)
◯	P total	-14.47
◯	P static	-14.47
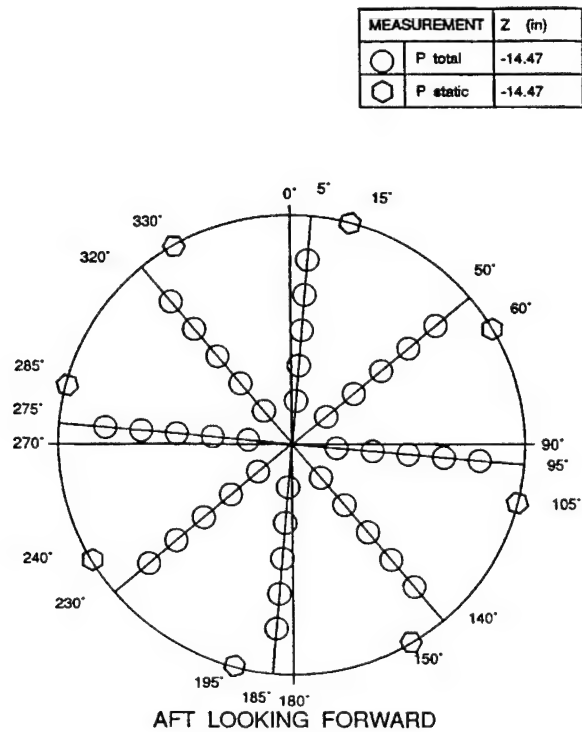
Figure 5 - 5 CRF distortion measurement station 15 instrumentation

72

MEASUREMENT		Z (in)
⊙	P/T total	
⬡	P static	OD: 6.44 ID: 7.00
■	P static - high resp.	6.44

AFT LOOKING FORWARD
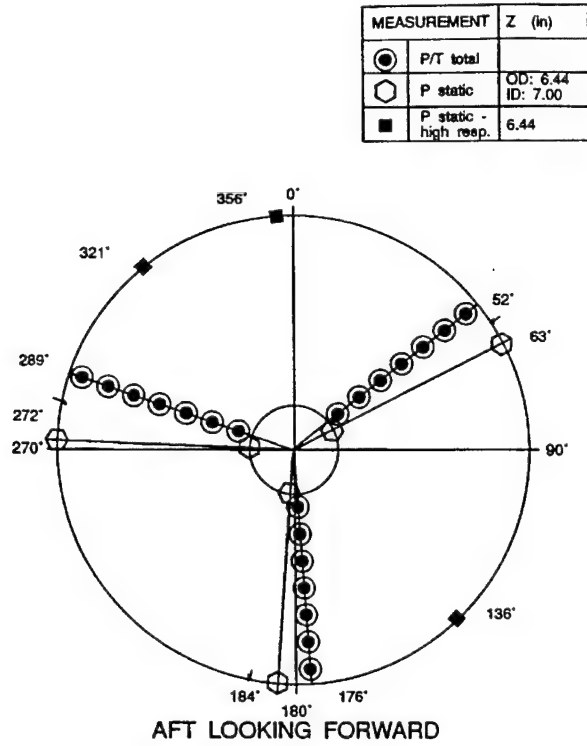
Figure 5 - 6 S1 leading edge instrumentation

MEASUREMENT		Z (in)
⊙	P/T total arc rakes	16.7
⬡	P static	OD: 16.70 ID: 16.32

AFT LOOKING FORWARD

a. discharge instrumentation

b. arc rake schematics
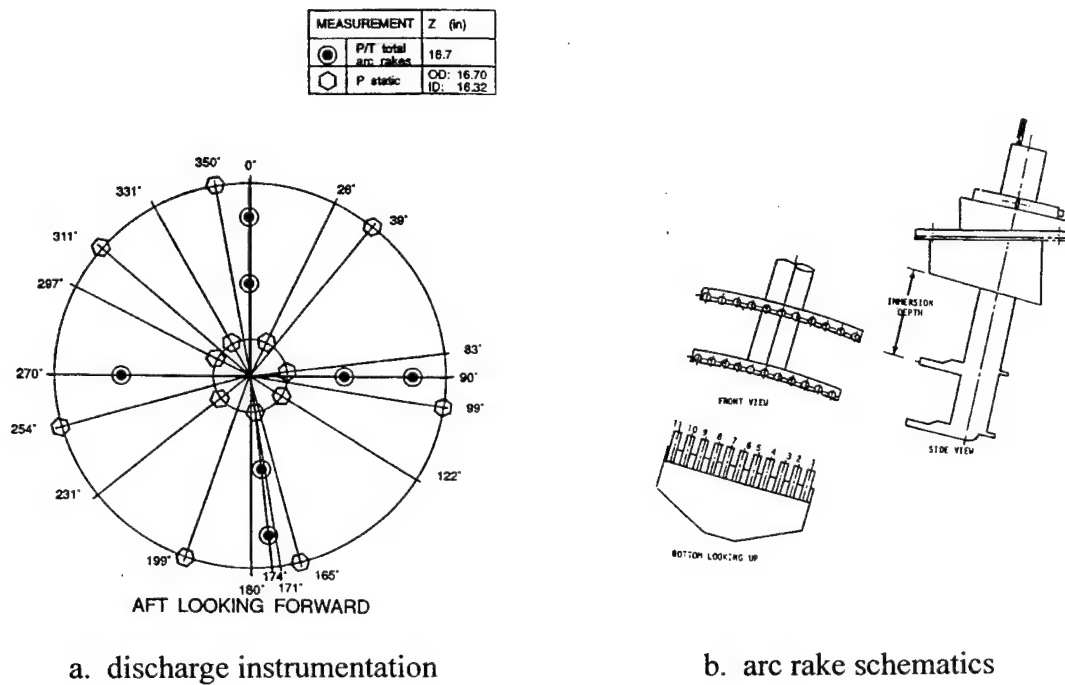
Figure 5 - 7 Fan discharge instrumentation

73

Throughout its test history, this fan has been subjected to a variety of inlet distortion patterns – hub radial, tip radial, 1/rev, 2/rev, 3/rev, 8/rev – all generated by screens. As indicated in Figure 5 - 1, distortion screen hardware was located approximately 56 inches upstream of the R1 hub leading edge. Hardware consisted of a one-inch square mesh backing screen used for mounting the different porosity screens of desired strength and pattern. Depending on the test program, the hardware was rotated – manually or remote automatically – to increase circumferential measurement resolution. The distortion testing is mentioned for reference to future application and because the backing screen, shown in Figure 5 - 8, was in place for most of the "clean inlet" (undistorted) testing.

5.2 Model Configuration

The SLCC "grid" used to represent the CRF fan is shown in Figure 5 - 9. The converged streamlines for the "design" condition (98.6% Nc, peak efficiency) are also indicated. Nineteen axial calculating stations were used to represent the flowpath. About 20 inches of inlet duct
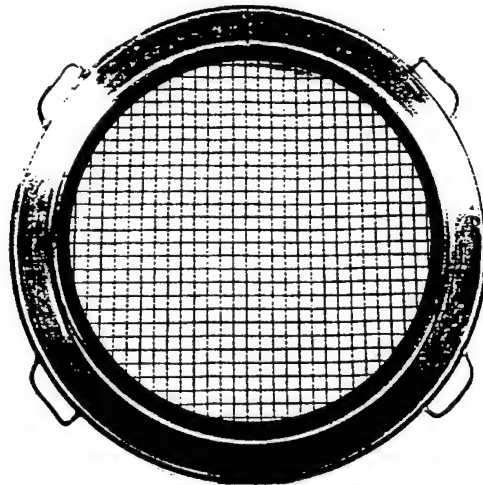
Figure 5 - 8 Distortion plane backing screen
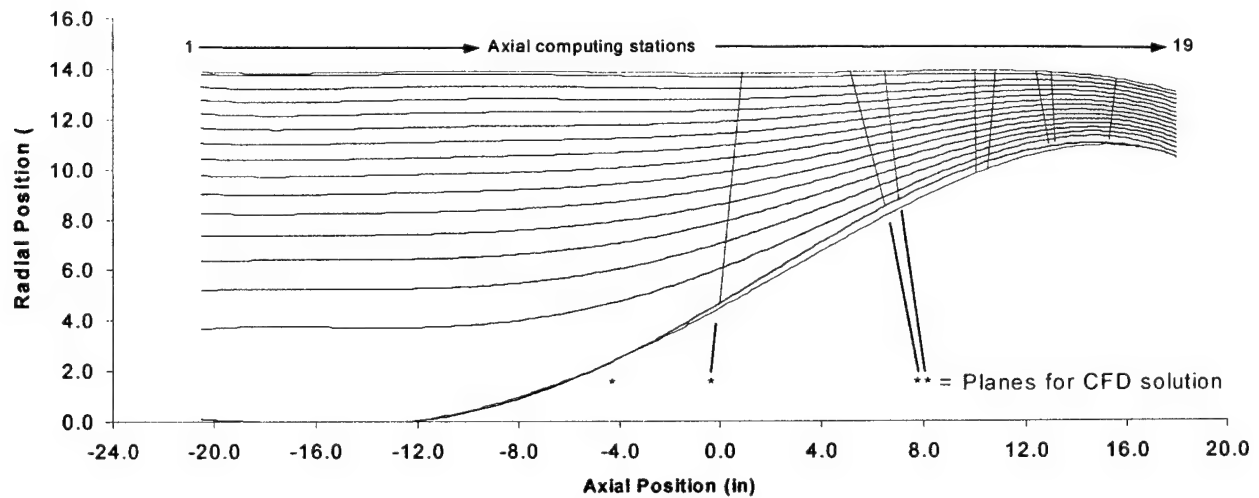
Scale: approximately 7.2:1 (same as Figure 5-1)

Figure 5 - 9 SLCC grid showing streamlines at 98.6% Nc, peak efficiency

upstream of R1 and 4 inches downstream of S2 were modeled. The z = -4.0 inches location

coincided with the inlet plane used in a fully 3-D RANS simulation of the R1 flow passage.

Calculations were performed only at the LE and TE of each blade row. Additional stations

within the row would undoubtedly increase accuracy, but at the expense of more detailed airfoil

geometry specification. Since the SLCC did not allow overlapping stations, the forward and aft

sections of S1 were modeled as one row. Only the S1 TE metal angle was allowed to change

during restagger. The SLCC iterated on 15 streamlines until radial equilibrium was satisfied

(actually 13 as two of the streamlines were defined by the hub and tip casing).

The correlations and models used in the SLCC required certain geometric parameters.

The following inputs were provided by the fan designer (Steenken, 2000) at twelve radial

locations for each of the four blade rows (note that a cubic spline fit was used to interpolate

parameters needed at actual streamline locations):

- Blade leading and trailing edge metal angles
- Mean radius between LE and TE

75

- Solidity (c/s)

- $(t/c)_{max}$

- Location of maximum camber (a/c)

- Lean angles at LE and TE

- Precompression airfoil – specified as % span from tip (rotors only)

Additionally, a single value for blade sweep (angle when viewed in meridional plane) was defined at the LE and TE of each row. The single-value input limited the S1 and S2 leading edge representation (compare Figures 5-1 and 5-9), but was not a significant source of error (relative to the correlations). Also, design annular blockage estimates were provided at the LE and TE of each row.

Finally, as noted in Section 3.4, an estimate for displacement thickness, δ^*, was used to reduce the actual tip casing to account for the mass flow deficit due to endwall boundary layer on the inlet ducting. As seen in Figure 5 - 1, the inlet ducting length was considerable – an accounting of the boundary layer growth was needed. Downstream of R1, displacement thickness estimates provided by the designer were used (Steenken, 2000). The analysis used to obtain the *inlet* δ^* estimate is provided below.

The problem is one of developing pipe flow (or "entrance length"). Most textbooks on boundary layer/viscous flow theory provide rigorous treatment of "fully-developed" flows (velocity does not vary with axial distance), and only briefly mention developing flow. Kays and Crawford, 1980, provide an entry length solution, but it is for laminar boundary layers and not applicable to the conditions of the present investigation.

In analyzing the CRF configuration, a combination of experimental data, CFD, and classic boundary layer theory were used. The following steps highlight the analysis, all performed at the design point, 98.6% Nc, peak efficiency:

- The boundary layer effects from the bellmouth inlet to station 10 were ignored (Figure 5 - 1). *Justification*: Favorable pressure gradient over a relatively small distance. Also, see Figure 5 - 10, which shows a uniform radial velocity profile at station 10 (although a parabolic profile is clearly seen with the magnified velocity scale). The measurements farthest from the centerline are approximately 0.6 inches from the inlet duct walls.
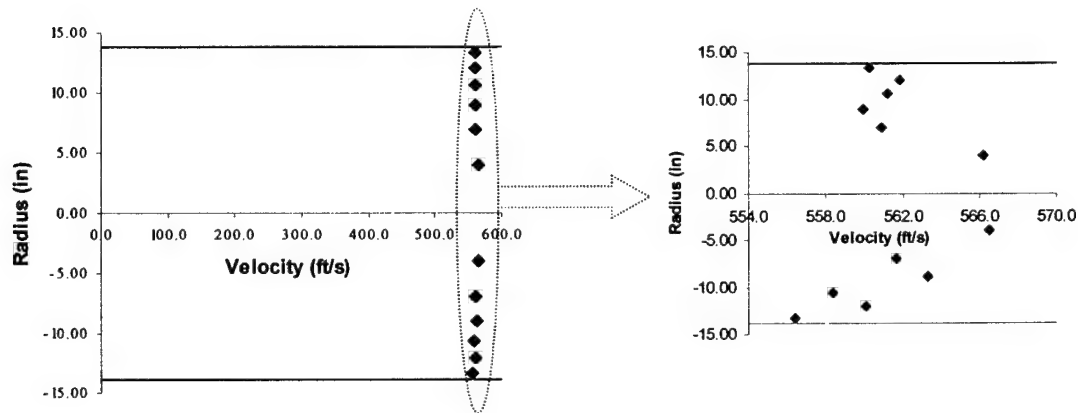
Figure 5 - 10 Design point radial velocity profile at CRF station 10 (z=-78 inches)

- Turbulent boundary layer downstream of station 10.
  Justification: The Re_D is approximately $7x10^6$, based on inlet velocity of 560 ft/s determined from station 10 measurements. This is well above transition Reynolds numbers quoted in any text discussing boundary layer development (see for example White, 1991, p. 218).

- The problem is one of developing pipe flow, turbulent boundary layer.

Justification: Goldstein, 1965, p. 360, presents the result given by Equation (5-1) for determining the entrance length, L_e, required for fully-developed pipe flow, assuming turbulent boundary layer at entry (station 10) using a 1/7 power-law velocity profile.

$$\frac{L_e}{D} = 0.693 \, \mathrm{Re}^{0.25} \tag{5-1}$$

Using Equation (5-1), the entrance length required for fully-developed flow is approximately 36 diameters; the present L/D is only about three.

- Estimate δ* from flat plate turbulent boundary layer momentum integral analysis with a 1/7 power-law velocity profile. This produced a δ*(x) variation of 0.00183x, from the well-known result (see White, p. 430) provided in Equation (5-2).

$$\delta^*(x) = \frac{1}{8}\delta(x) \approx \frac{1}{8}\frac{0.16x}{\mathrm{Re}_x^{1/7}} \tag{5-2}$$

Justification: When the boundary layer is small compared to the pipe radius (i.e., when $x/(\mathrm{Re}_D D) < 0.001$), boundary layer behavior in the entrance length is quite similar to that on a flat plate (Shah, 1978). For the present work, the $x/(\mathrm{Re}_D D)$ is much less than 0.001.

The above analysis produced a δ*(x = 78 in) of approximately 0.14 inches, resulting in an area blockage of about two percent at the R1 leading edge. Since only the first 20 inches of duct were modeled, a blockage of 0.01 was input at the first axial calculating station and grown to 0.02 at R1. Figures 5-11 and 5-12 show the predicted velocity profiles at the leading edge and trailing edge, respectively, of the first rotor. The data points (blue diamonds) shown in Figure 5-11 were obtained from laser measurements as reported by Rabe, 1987. The CFD results show good comparison with these data, and both show the strong influence of the tip leakage vortex upstream and downstream. Three SLCC predictions are shown: (a) no boundary layer, no tip

blockage (slcc-no blkg), (b) boundary layer, but no tip blockage (slcc-bl), and (c) both boundary

layer and tip blockage included (slcc-bl&tip).
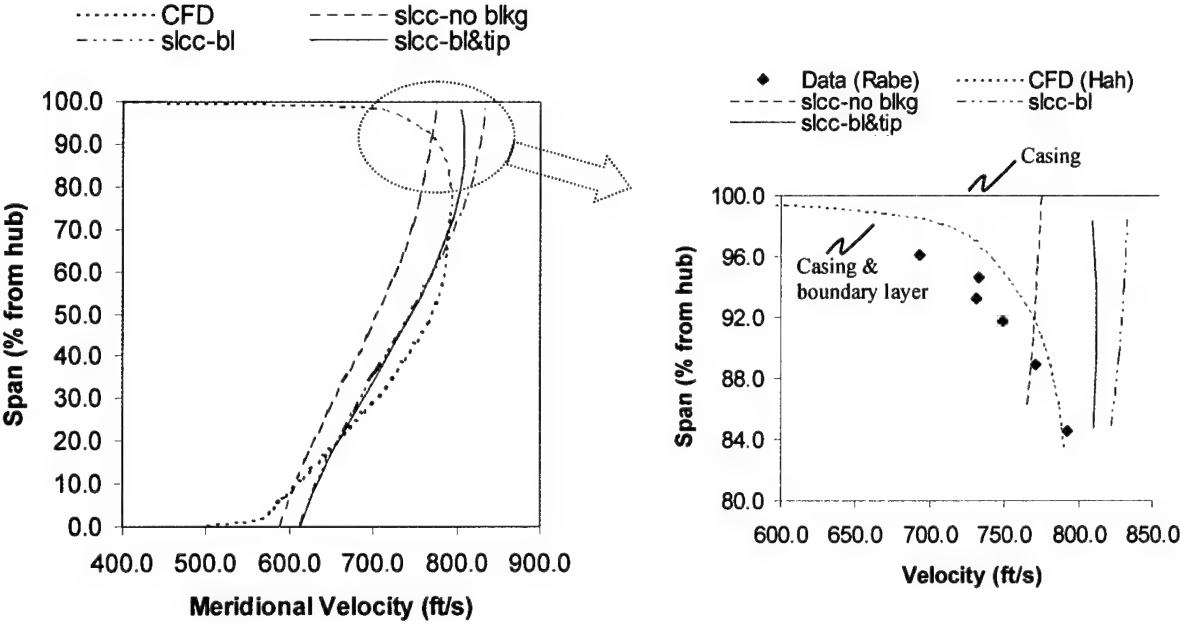
Figure 5 - 11 Measured and predicted design point velocity profiles at the entrance to R1
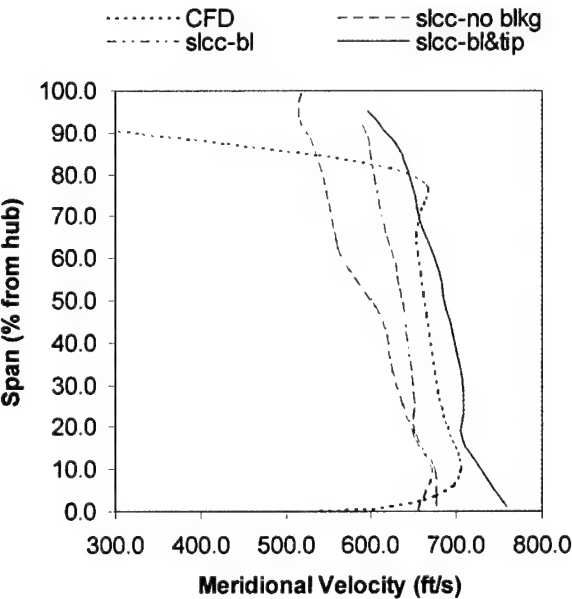
Figure 5 - 12 Predicted design point velocity profiles at the exit of R1

A 60% area reduction *in the outermost streamtube* (1 of 14) was used to account for additional tip leakage blockage effects at the R1 exit. This resulted in approximately 10% total area blockage at the R1 exit plane due to tip endwall boundary layer losses, quite reasonable as discussed by Rabe, 1987. Area reductions of 50% and 25% were used in the tip regions of S1 (variable vane) and R2, respectively.

As expected, the predicted radial velocity distribution improved when blockage effects were included. Looking at the boundary layer profiles (magnified view in Figure 5 - 11), three points should be made:

(a) Although high in its estimate, the full blockage case (slcc-bl&tip) trends with the data and CFD - the maximum velocity is predicted at around 89% span. The inviscid solution approach does not allow for proper diffusion in this very complex tip region (i.e., the full effect of tip leakage is not adequately modeled).

(b) As seen in the full velocity profile (Figure 5 - 11), inclusion of blockage effects provides improved predictions over much of the mid-span, a region of relatively low loss. Accurate estimation of this region is needed for favorable efficiency comparison.

(c) As shown in Figure 5 - 12, accurate prediction of the R1 exit velocity profile relied on both boundary layer and tip blockage effects. The predicted profile resulted in very reasonable incidence angles needed for accurate flow prediction through the first stator.

5.3 Model Calibration

The following paragraphs describe the SLCC calibration procedure, designed to meet the objectives below:

- Capture the trends in both overall and radial performance
- Minimize parameter adjustment needed to achieve reasonable results

- Keep all parameters and properties physical

As previously mentioned, streamline curvature methods generally yield acceptable solutions provided blockage, loss, and deviation are "accurately" predicted (the subject of accuracy is addressed further in Section 5.4). For the present application, blockage estimation was already described in the previous section. Improvements in loss modeling, most notably in the shock loss model demonstrated in Chapter 4, and tip loss model discussed in Chapter 3, were a key focus area of the present work. Consequently, it was expected that the calibration process would predominantly involve deviation estimation. This was precisely the case.

Essentially, the calibration involved iterative adjustment of *radial* deviation at the exit of both rotors, *global* deviation (same amount applied at all sections at each blade row), and the tip loss model factor, TLOSS (see Equation 3-3), at the peak efficiency operating condition at 98.6% Nc. Radial deviation was adjusted at R1 and R2 to capture total temperature performance trends as measured at the S1 and S2 leading edges (i.e., see Figure 5 - 13). Global deviation was adjusted to match the overall, area-averaged, total temperature ratio. The values for the R1 and R2 TLOSS were selected to provide "reasonable" tip loss coefficients based largely on the work of Lakshminarayana, et al., 1985. At operating conditions other than peak efficiency, only global deviation was adjusted (to match overall temperature ratio) – the models and correlations did the rest.

A radial comparison at the design peak efficiency condition is provided in Figure 5 - 13, which shows measured and predicted total pressure and temperature at the S1 and S2 leading edges. The "uncal" curves represent SLCC predictions with no adjustment of radial deviation. It was apparent from these comparisons that capturing the correct trends would require radial

81
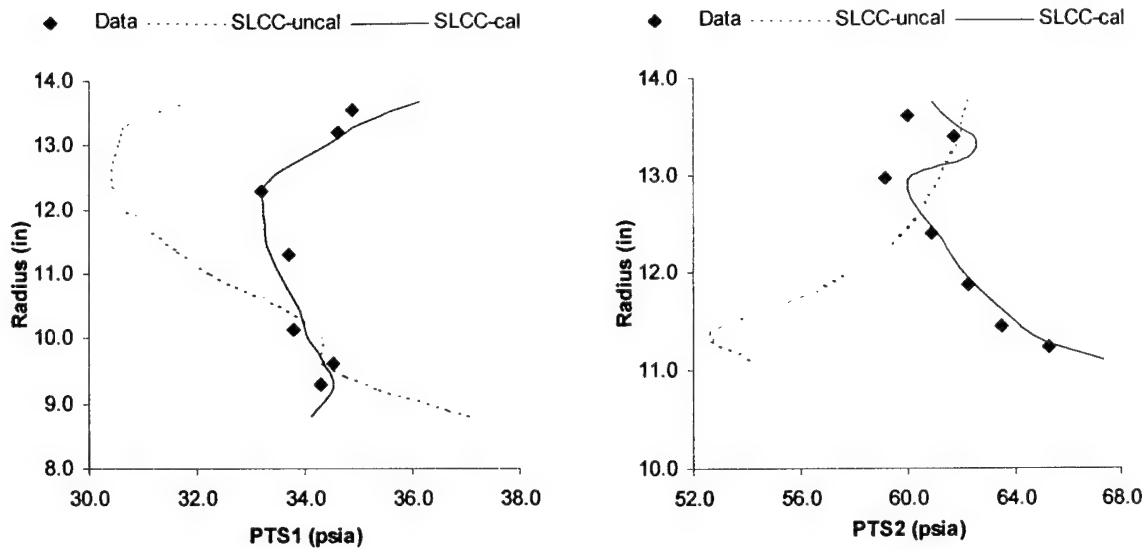
a. Total pressure at S1 and S2 leading edges
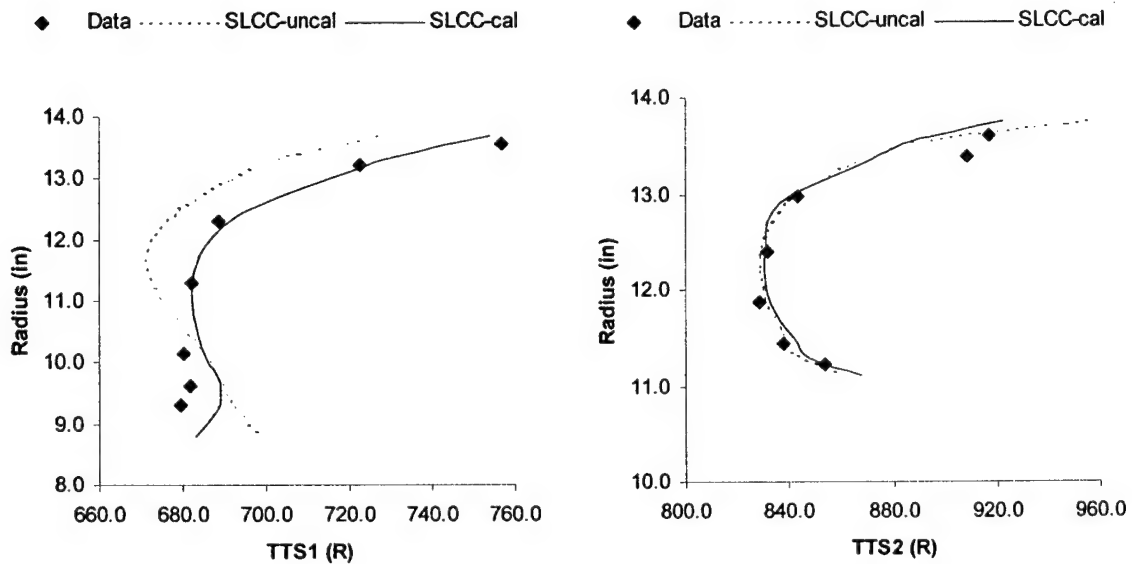
b. Total temperature at S1 and S2 leading edges

Figure 5 - 13 Radial performance comparison at 98.6% Nc, peak efficiency

calibration of the predicted deviation (the "cal" curves). As discussed in Chapter 3, the present

deviation correlation is simply not applicable to these designs. Result details are provided in the

next chapter.

Finally, it should be noted that Equation (3-2b) was used to provide a negative increment in loss coefficient in the hub regions of all four blade rows. This was done to offset unreasonably high estimates of loss in these regions (in excess of 0.5) and thus bring hub performance more in line with measured results. Justification of this procedure was twofold. First, the high-turning, tailored blade profiles in modern hub sections are well outside the correlation database. Second, no attempt was made to improve the hub performance estimation as was done with the tip. As will be shown in the next section, accurate representation of the tip region was more critical than that in the hub. This was precisely why the hub region was not selected as a target area of improvement.

5.4 Parameter Estimation Accuracy

Emphasized throughout this work is the need to capture the correct physical trends for the right reasons; i.e., because the physics are properly represented. Indeed, this must be the case if there is any hope for gaining physical insights into complex problems that cannot be represented any other way than by approximate methods. With this over-riding issue in mind, the discussion in this section seeks to provide a *quantitative* analysis regarding the accuracy of loss, deviation, and blockage estimates – these are the key parameters for all streamline curvature approaches.

With the help of iSIGHT™ (iSIGHT™ Guides, 1998), SLCC model parameters were systematically varied to obtain solution sensitivities. The iSIGHT is a software shell that exercises a simulation code (or codes) allowing for process integration, problem definition (sensitivity, optimization, etc.), and solution monitoring. The sensitivity study was performed for *all operating conditions* examined in the present work. For reference, the fan map given in Figure 5 - 14 shows these conditions. Seven input parameters were varied to explore their effect
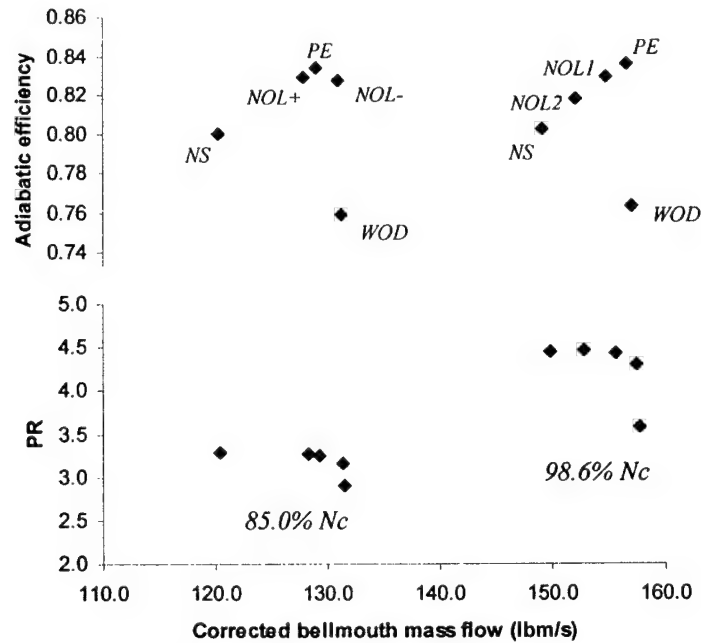
Figure 5 - 14 CRF fan operating conditions used in present investigation

on three global output parameters – the total pressure ratio (PR), the total temperature ratio (TR), and the adiabatic efficiency. A brief description of each of the input parameters is provided below. Figure 5 - 15 schematically indicates the region on the fan impacted by each parameter's perturbation.

- addlos – increment of loss coefficient applied to each section of each blade row

- adddev – increment of deviation angle applied to each section of each blade row

- imnfac – factor impacting prediction of i_{min} applied to each section of each blade row (see Equation 3-4)

- hubloss – factor impacting secondary loss prediction in R1 hub sections (see Equation 3-2b)

- tiploss – factor impacting secondary loss prediction in R1 tip sections (see Equation 3-3)

- tipblkg – factor impacting blockage at R1 trailing edge tip (from combined effects of leakage vortex, boundary layer, and shock interactions)

- blblkg – annulus wall boundary layer blockage (% area reduction) at R1 leading edge

84
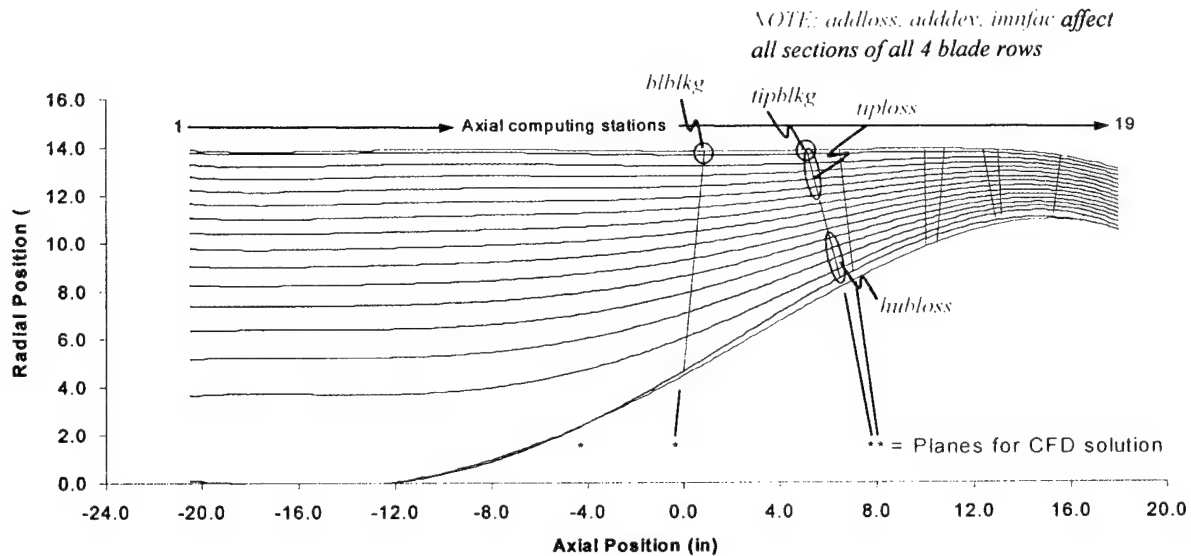
Figure 5 - 15 Fan schematic indicating input parameter region of influence for sensitivity study

The SLCC was calibrated following the procedure just described in Section 5.3, thus providing the baseline values (input and output parameters) for each fan operating condition. Each of the seven input parameters identified above was then individually perturbed from its nominal (baseline) value by approximately *+/- 3% of its maximum value*. This was done to provide a valid basis for comparing each parameter's effect on the selected output parameters. For example, at the design point condition, R1 blade section values for loss coefficient ranged from 0.09 – 0.36 (see Table 3 - 2). Each of these was varied +/-0.01 in magnitude (Table 5 - 2), representing anywhere from an 11% - 3% change from nominal blade section loss coefficient.

Table 5 - 2 provides an example of the sensitivity analysis performed at the 98.6% peak efficiency condition. The baseline values for the inputs and outputs are provided as the first row of results, followed by results of fourteen additional model runs as each parameter was systematically varied according to the procedure just described. In each case, the resulting effect on PR, TR and efficiency are provided in Table 5 - 2, summarized by input parameter as "% total

85

Table 5 - 2 Results from parametric sensitivity analysis, 98.6% Nc, peak efficiency

HTSC Sensitivity Results at 100% Nc, Peak eff. (W = 150.45)

8-Jan-01

RunCounter	addlos	adddev	imnfac	hubloss	tipblkg	tiploss	blblkg	tratio	efficiency	pratio	Calculated difference from nominal (abs.val.) tratio	efficiency	pratio
1=baseline	0	-7.22	0.5	-0.8	1.2	4	0.021	1.6133	0.8377	4.2683	0	0	0
2	-0.01	-7.22	0.5	-0.8	1.2	4	0.021	1.6193	0.85346	4.4162	0.006	0.01576	0.1479
3	0.01	-7.22	0.5	-0.8	1.2	4	0.021	1.6051	0.81741	4.0823	0.0082	0.02029	0.186
4	0	-7.52	0.5	-0.8	1.2	4	0.021	1.623	0.84056	4.3673	0.0097	0.00286	0.099
5	0	-6.92	0.5	-0.8	1.2	4	0.021	1.6028	0.83348	4.1571	0.0105	0.00422	0.1112
6	0	-7.22	0.44	-0.8	1.2	4	0.021	1.6117	0.83471	4.2368	0.0016	0.00299	0.0315
7	0	-7.22	0.56	-0.8	1.2	4	0.021	1.6147	0.83964	4.2922	0.0014	0.00194	0.0239
8	0	-7.22	0.5	-0.95	1.2	4	0.021	1.6129	0.83797	4.2666	0.0004	0.00027	0.0017
9	0	-7.22	0.5	-0.65	1.2	4	0.021	1.6135	0.83747	4.2686	0.0002	0.00023	0.0003
10	0	-7.22	0.5	-0.8	1.14	4	0.021	1.6149	0.83871	4.2882	0.0016	0.00101	0.0199
11	0	-7.22	0.5	-0.8	1.26	4	0.021	1.6115	0.83653	4.2465	0.0018	0.00117	0.0218
12	0	-7.22	0.5	-0.8	1.2	3.85	0.021	1.6138	0.83855	4.278	0.0005	0.00085	0.0097
13	0	-7.22	0.5	-0.8	1.2	4.15	0.021	1.6127	0.8368	4.2578	0.0006	0.0009	0.0105
14	0	-7.22	0.5	-0.8	1.2	4	0.018	1.6093	0.83161	4.1991	0.004	0.00609	0.0692
15	0	-7.22	0.5	-0.8	1.2	4	0.024	1.622	0.84915	4.4125	0.0087	0.01145	0.1442
										Diff. Sums	0.0552	0.07003	0.8768

% total effect calc. by iSIGHT

	tratio	efficiency	pratio
addlos	0.257	0.515	0.381
adddev	0.366	0.101	0.240
imnfac	0.054	0.070	0.063
hubloss	0.011	0.007	0.002
tipblkg	0.062	0.031	0.048
tiploss	0.020	0.025	0.023
blblkg	0.230	0.250	0.243
Sums	1.000	1.000	1.000

NOTE: Changes to input paramters based on 3% of maximum values

Para:	Max
addlos	0.35
adddev	10 deg
imnfac	2.0
hubloss	5.0
tipblkg	2.0
tiploss	5.0
blblkg	0.1

Sample calculation of % total effect of addlos on tratio:
(0.006+0.0082)/0.0552
which equals 0.257 or 25.7%
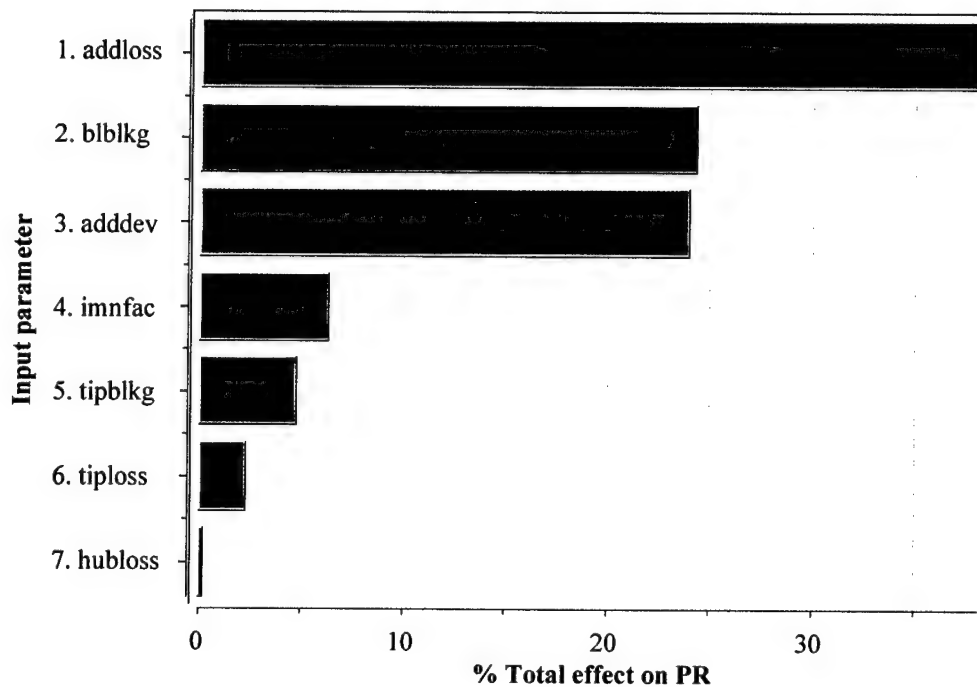
Figure 5 - 16 SLCC input parameter sensitivity analysis on overall total pressure ratio (PR), 98.6% Nc, PE
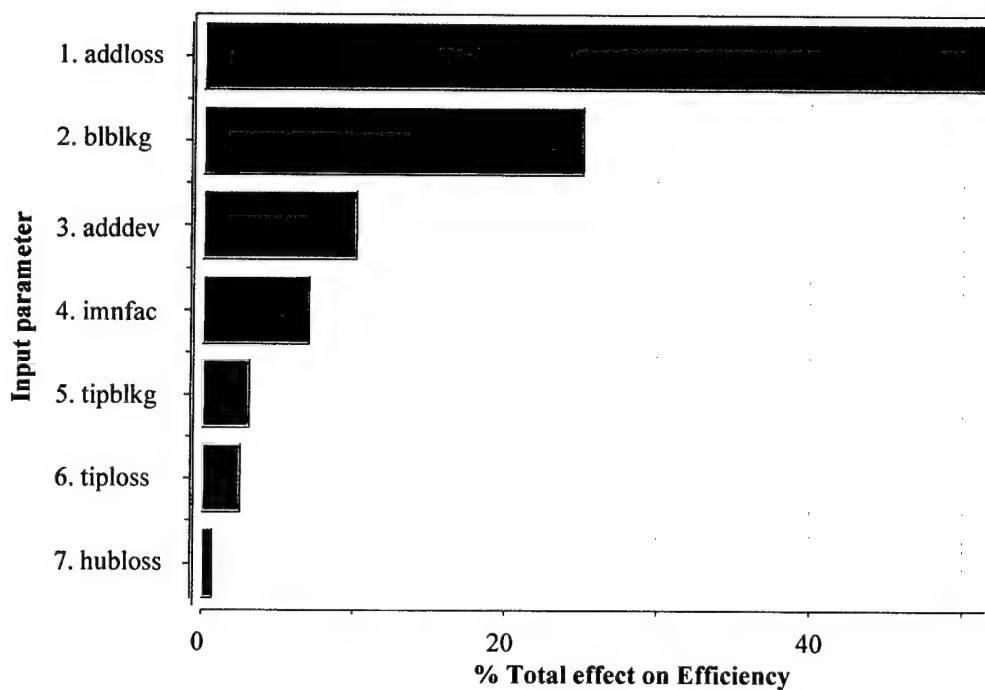
Figure 5 - 17 SLCC input parameter sensitivity analysis on overall adiabatic efficiency, 98.6% Nc, PE
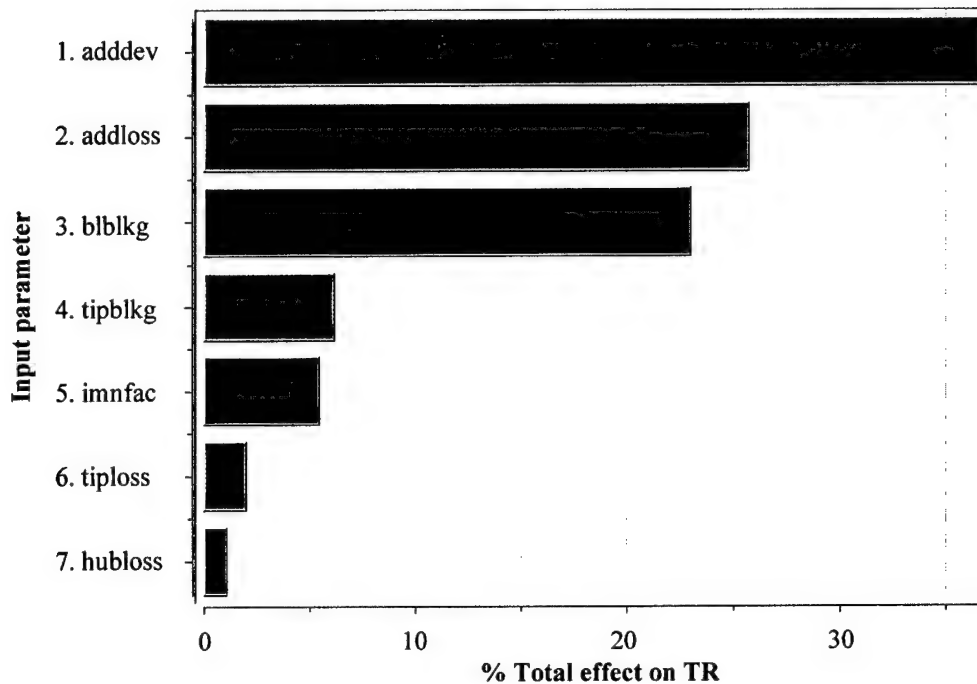
Figure 5 - 18 SLCC input parameter sensitivity analysis on overall total temperature ratio (TR), 98.6% Nc, PE

effect" on output parameter (in the green highlighted area). This is an iSIGHT™ representation, discussed in more detail below. In addition, a sample calculation is provided in Table 5 - 2. Graphical results for the analysis of Table 5 - 2 are provided in Figures 5-16 – 5-18. Results from all the analyses were complied and are presented graphically in Figures 5-19 – 5-21, one for each of the three selected output parameters.

Not surprising, results from the study confirmed that loss, deviation, and boundary layer blockage are all key parameters for obtaining accurate performance predictions. More important, however, is that the results provide a *quantitative* measure of sensitivity and the degree of accuracy required for parameter estimation. For example, improved loss estimation was a key focus area of the present work. For application to the CRF fan, results from Table 5 - 2 (indicative of all results) show that predicting overall pressure rise and efficiency to about +/- 3.0% and +/-2.0%, respectively, requires +/-0.010 accuracy of the loss coefficient. This result

a. 98.6% Nc

b. 85.0% Nc
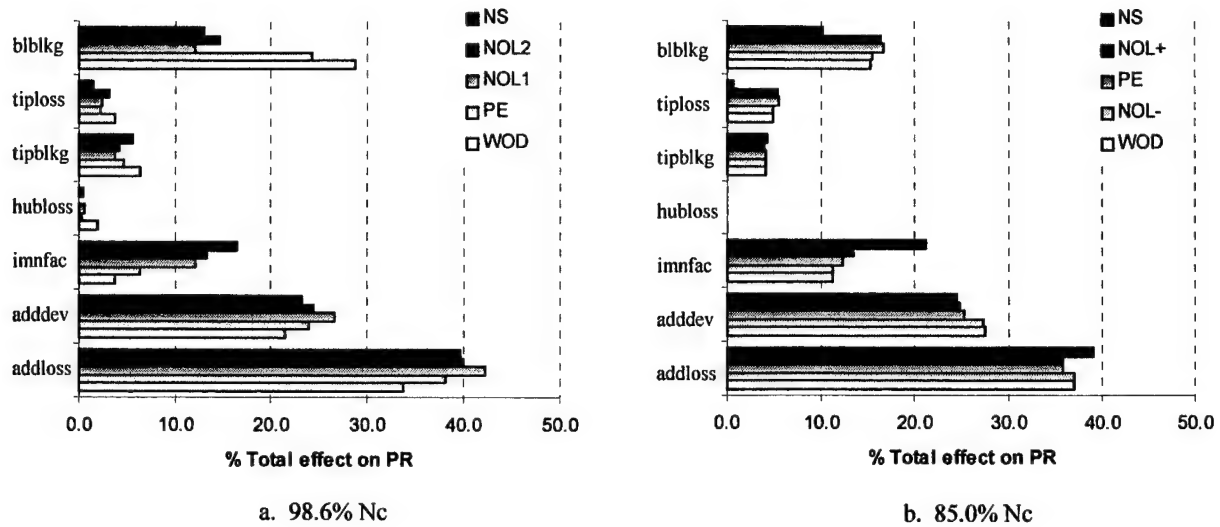
Figure 5 - 19 Summary results from sensitivity study – influence on overall total PR

a. 98.6% Nc

b. 85.0% Nc
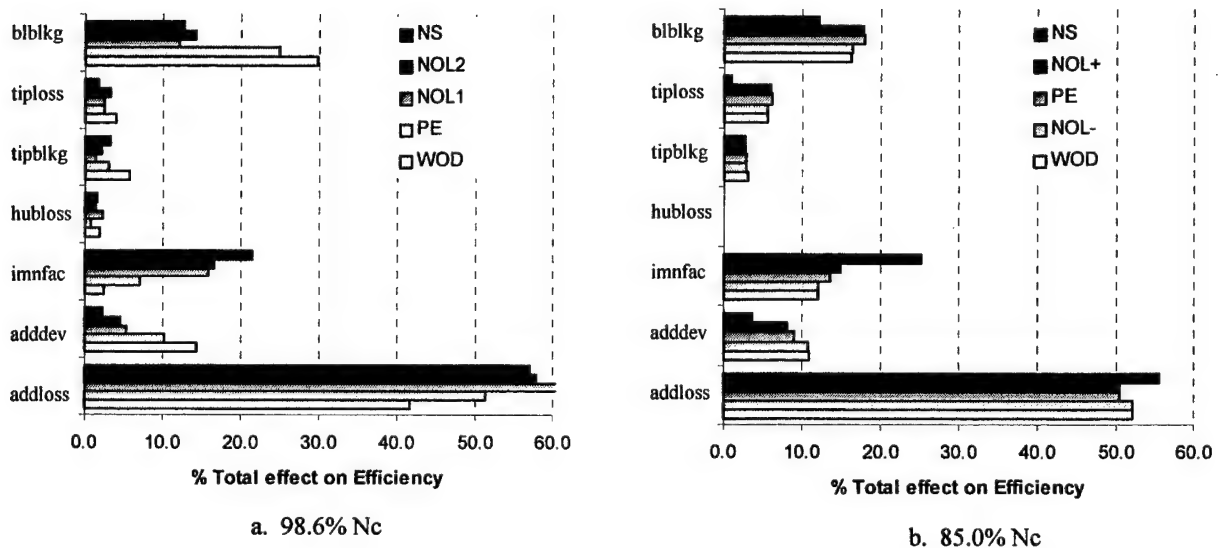
Figure 5 - 20 Summary results from sensitivity study – influence on overall efficiency

seems quite reasonable given the numbers noted by Bloch, et al., 1999 for a single rotor: +/-1-2% in pressure rise and +/-1% in efficiency for the same +/-0.010 accuracy in loss coefficient. The effect of inaccurate loss coefficient estimation would be magnified in a multistage application.
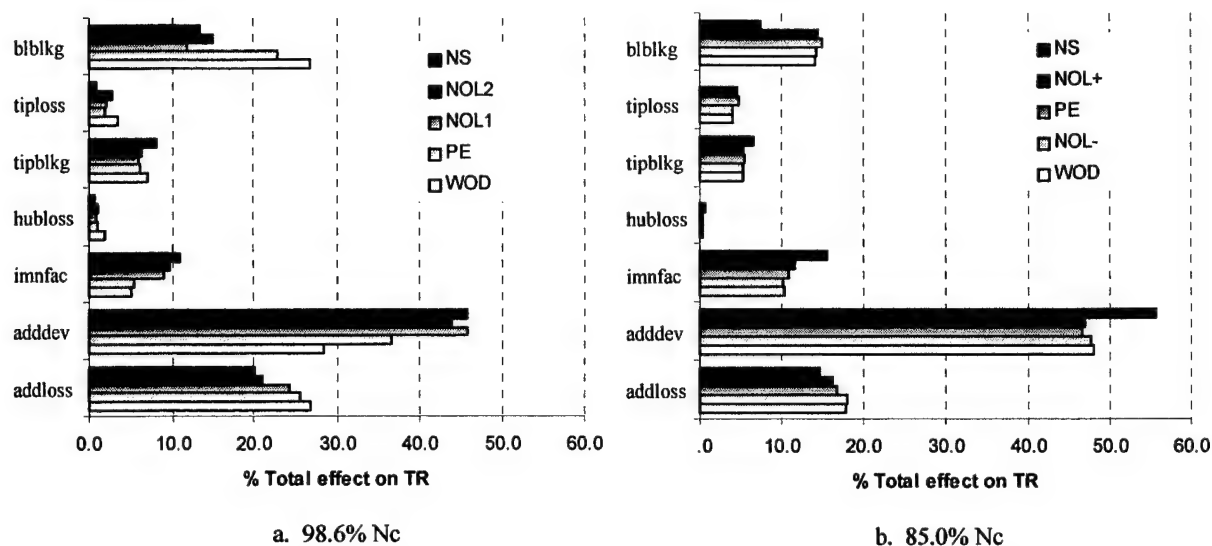
Figure 5 - 21 Summary results from sensitivity study – influence on overall total TR

Regarding the sensitivity results, the following points should be made:

- In the plots, results are displayed as "percent total effect" on each output parameter. As each input parameter is varied from its nominal value, iSIGHT™ takes the difference (absolute value) between the output parameter value and its nominal value. These differences from each input parameter's +/- variation are summed, then divided by the overall sum of the differences to get each parameter's percent total effect. While this tends to hide any nonlinear behavior within the region of interest, it does provide a reasonable quantitative measure of sensitivity. Also, note from Table 5 - 2 that the only significant nonlinearity occurs with the "blblkg" variation. A sample "% total effect" calculation is provided in the table.

- Blue bars in Figures 5-16 – 5-18 (iSIGHT™ plots) indicate a positive or direct correlation between the input and output parameters, while red indicates a negative or inverse correlation. For example, in Figure 5 - 18, the first red bar indicates that an *increase* in

90

deviation angle would produce a *decrease* in overall TR, a result that would certainly be expected.

- The importance of accurate loss estimation, especially regarding total pressure rise and hence, efficiency prediction, is clearly demonstrated. Again, improved loss estimation was a focus of the present work.

- As mentioned previously, an accurate prediction of i_{min}, the incidence at which minimum loss occurs, is another key to successful SLC application. As shown in all the figures, the influence of the "imnfac" parameter ("factor" in Equation 3-4) on all of the global output parameters is on a par with that of inlet boundary layer blockage ("blblkg"). Note also that the influence increased with loading (turning) in all cases, most notably on pressure rise and efficiency. This was not surprising, given the parabolic nature of the section loss characteristic.

- Also discussed earlier was the relative importance of tip loss representation over the hub region. This is verified for the present application. The "hubloss" parameter showed negligible influence on all three output parameters.

- Figures 5-19 – 5-21 show that, in general, the sensitivity results were relatively independent of fan speed and operating condition. A notable exception is the influence of "blblkg" at 98.6% Nc on all three output parameters. As shown in Figures 5-19a, 5-20a, and 5-21a, inlet boundary layer blockage has a much larger influence at the two lower operating conditions – WOD and PE. This seems logical, given that at conditions around peak efficiency the loss "bucket" is relatively flat. Consequently, at peak efficiency conditions, the role of factors influencing loss estimation would be reduced, while the influence of boundary layer blockage would be magnified. Indeed, this is confirmed by the behavior of the "imnfac" and

91

"addloss" factors in Figures 5-19a and 5-20a (and to a lesser degree in Figures 5-19b and 5-20b at 85% Nc).

- The influence on overall temperature rise (Figure 5 - 21a) requires an additional explanation. At low aerodynamic load operating conditions, less flow turning is involved. Thus, as indicated in Figure 5 - 21a, the influence on TR as the aerodynamic loading increases is essentially a tradeoff between "blblkg" and deviation angle ("adddev").

6. Performance Prediction and Comparison with Experimental and CFD Results

The procedure used to calibrate the modified SLCC to the two-stage CRF fan was described in the previous chapter (Section 5.3). Here, results from the calibrated model are presented for two fan speeds – 98.6% and 85% Nc – over a range of operating conditions from near-choke (or wide-open discharge) to near-stall. Performance predictions were compared to those determined from experimental measurements and a CFD solver. The CRF data (Section 5.1) provided the basis for experimental comparison.

The CFD results were from a 3-D, steady, RANS model applied across the *first rotor* only. The numerical solution was based on a high-order, upwinding relaxation scheme, and a modified (for low Reynolds number effects) k-ε, two-equation turbulence model was used to provide the Reynolds' stress terms. As discussed by Hah and Wennerstrom, 1991, an I-grid was used to provide good resolution near the blade as well as at the far field. Slightly different grid sizes were used at the two speeds examined here – these will be presented below. Additional details of the CFD approach can be found in Hah and Wennerstrom, 1991, and Hah, 1987. Further, it should be noted that the Hah model has been used previously to represent the flow field through the first rotor of the CRF fan. Hah, et al., 1998 performed both a steady and unsteady, 3-D, viscous flow analysis on two R1 flow passages with and without 8/rev inlet total pressure distortion (two passages covered the distortion period). Rabe, et al., 1999, extended that work by examining the full annulus flow field across R1.

6.1 Overall and Radial Performance – Design Speed Results

As presented in Section 5.3, a detailed radial adjustment of deviation angle was required at the design point (98.6% Nc, peak efficiency) to obtain reasonable performance estimates (see
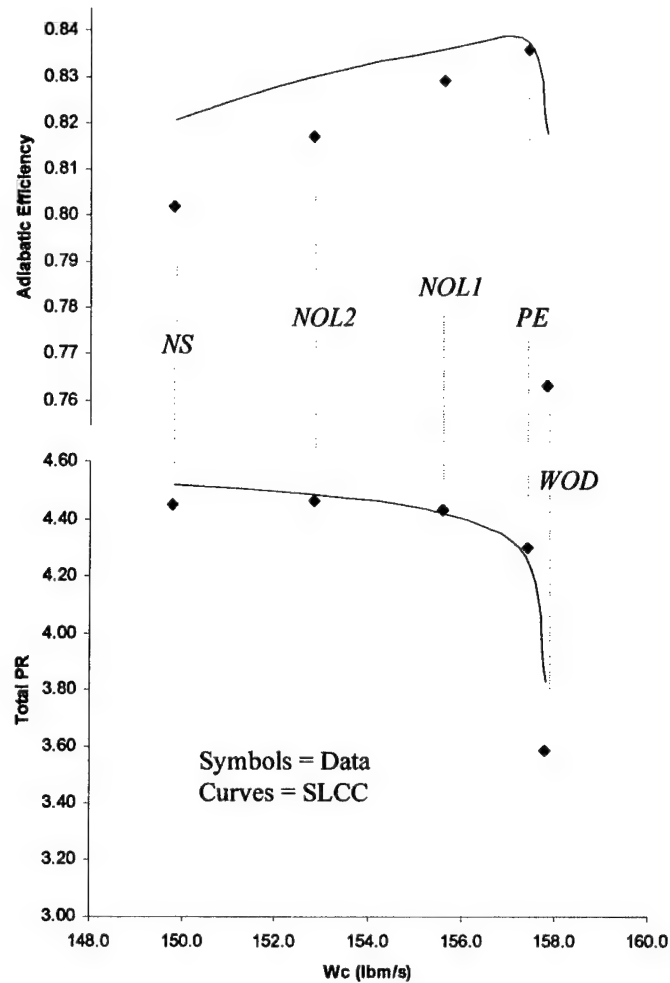
Figure 6 - 1 Overall performance comparison of CRF two-stage fan at 98.6% Nc

Figure 5 - 13, for example). This section shows results of model improvements and calibration

at this condition and four other operating conditions from low loading (wide-open discharge) to

high loading (near-stall). Both overall and radial performance results are presented.

Figure 6 - 1 shows the overall machine performance comparison at five operating

conditions. Radial comparisons of total pressure and temperature at the leading edge of both

stators are provided in Figures 6-2 – 6-6 for each of the operating conditions. The radial results

are most encouraging. Correct trends are captured for the right reasons – more of the physics is

modeled. Previous applications of the TEACC approach required specification of radial

distributions of deviation, loss, and blockage as functions of speed and mass flow rate to achieve

94

reasonable performance simulation – see Hale and O'Brien, 1998, and Hale, et al., 1999. Here, as was described in Section 5.3, radial distribution of *deviation at only one operating condition* was required. Only a global deviation adjustment at each condition was required to achieve the results shown. It appears that the modifications to the model have resulted in an improved, more physics-based representation.
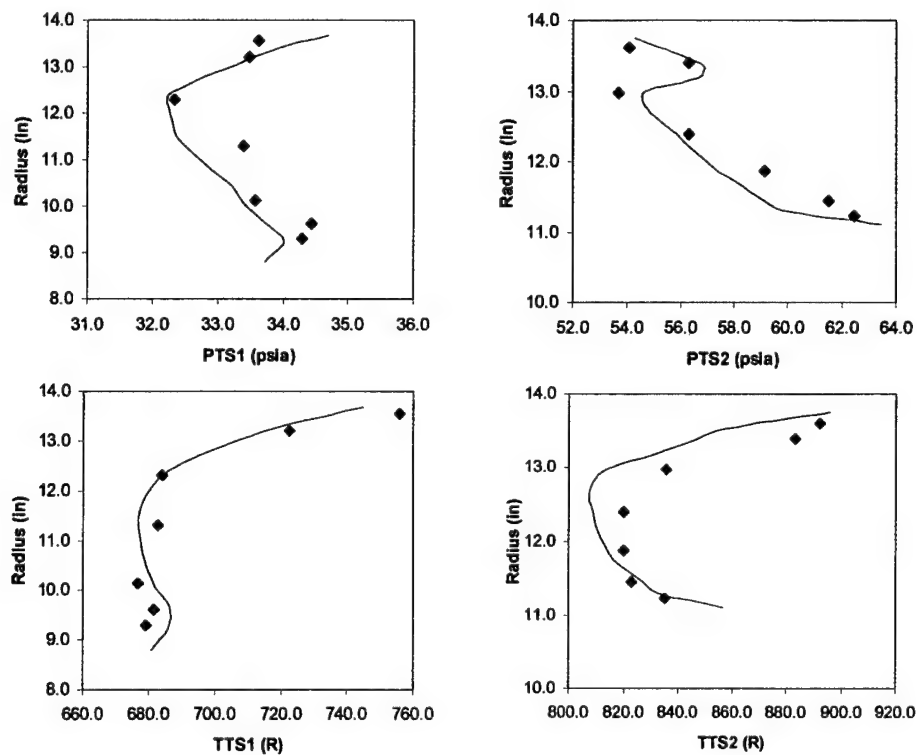
Figure 6 - 2 Radial comparison at 98.6% Nc, WOD (symbols = data)
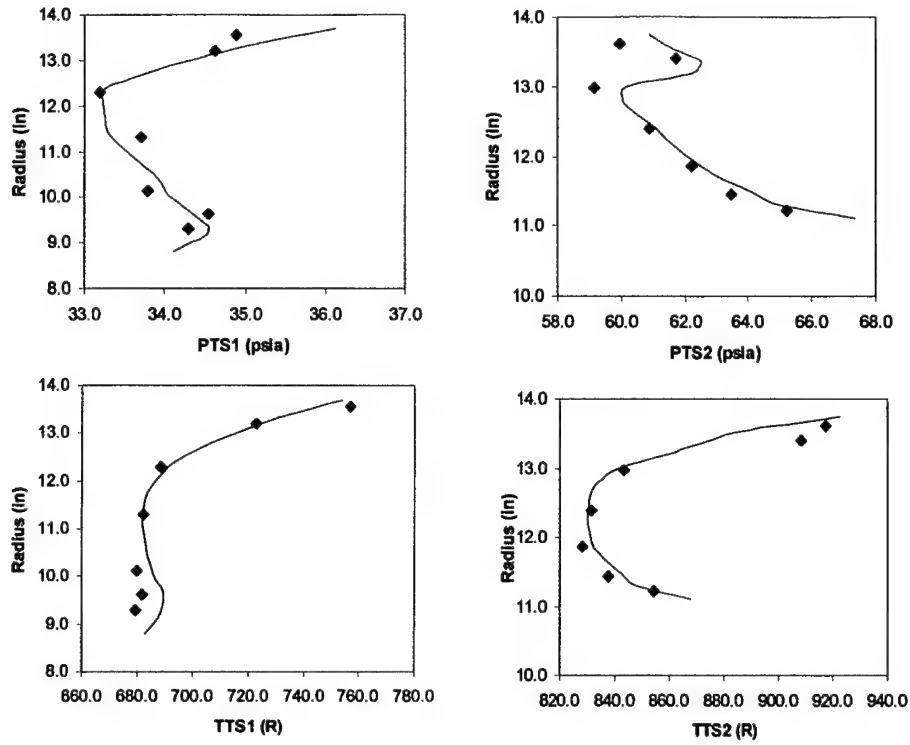
Figure 6 - 3 Radial comparison at 98.6% Nc, PE (symbols = data)
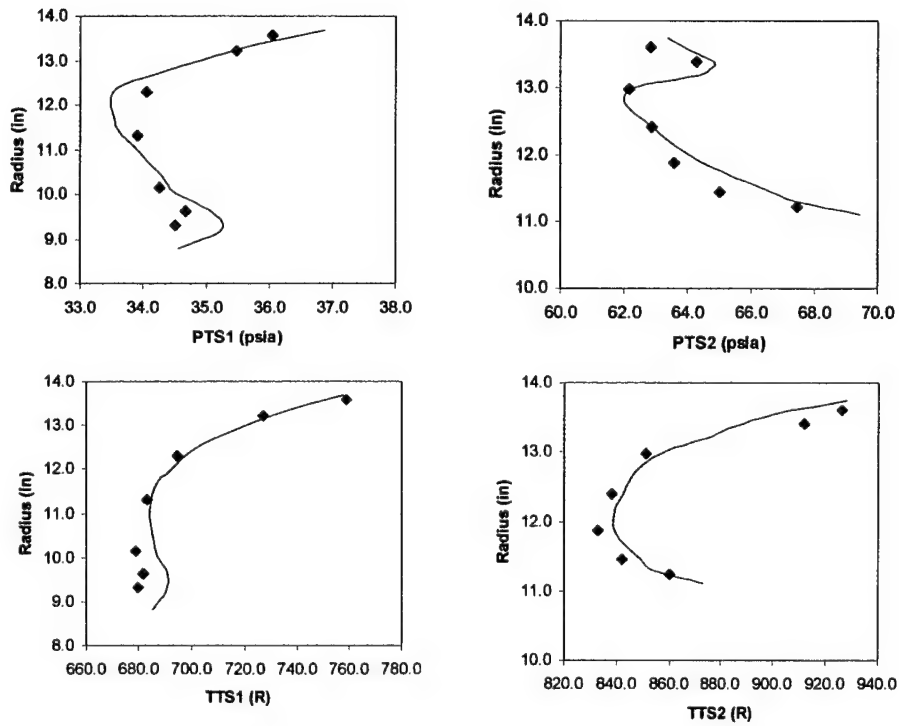
Figure 6 - 4 Radial comparison at 98.6% Nc, NOL1 (symbols = data)
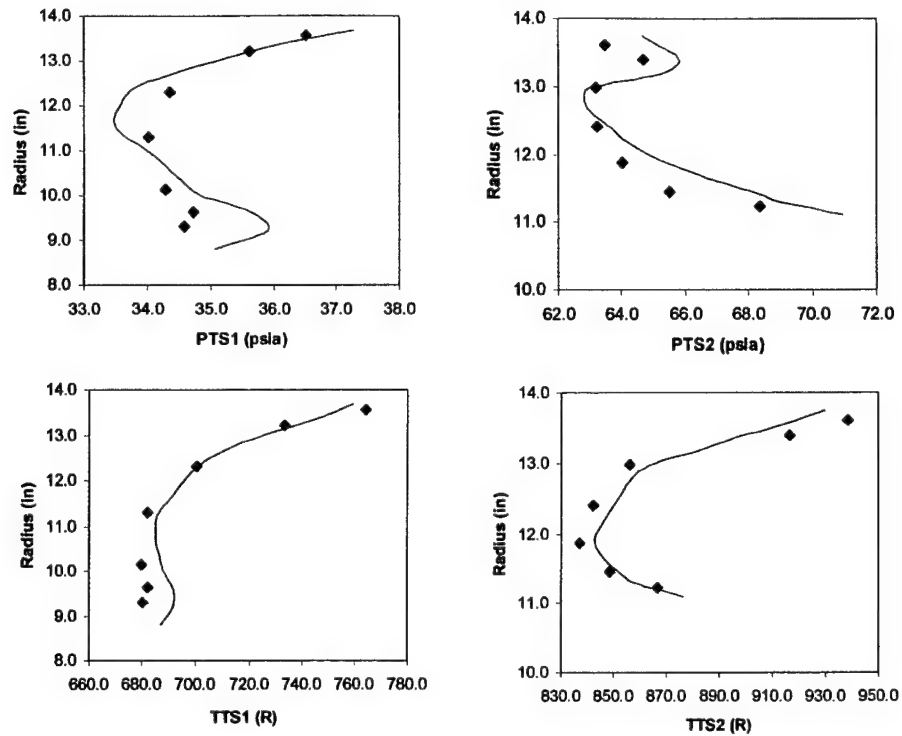
Figure 6 - 5 Radial comparison at 98.6% Nc, NOL2 (symbols = data)
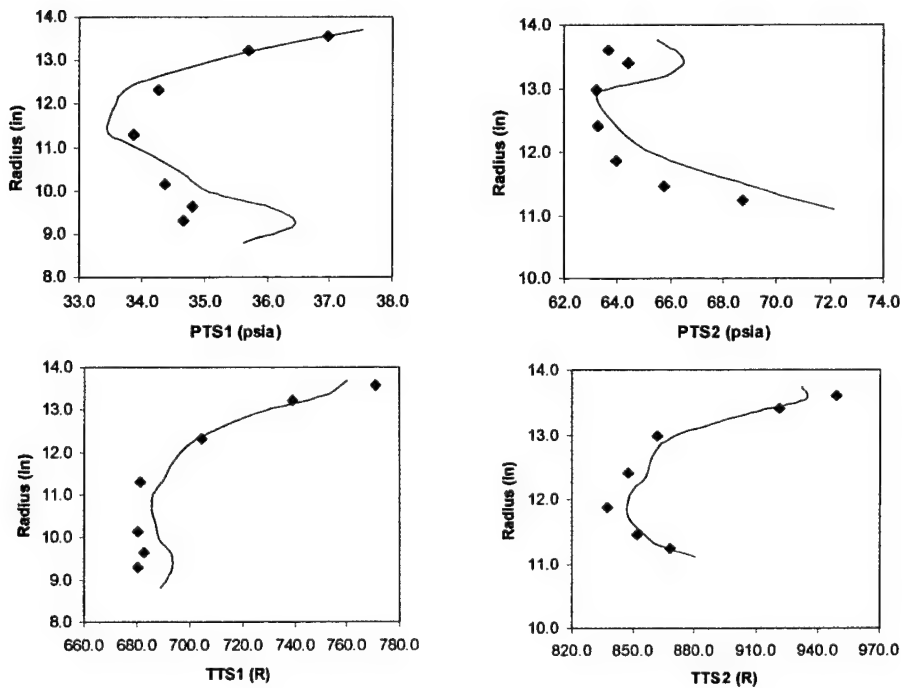
Figure 6 - 6 Radial comparison at 98.6% Nc, NS (symbols = data)

97

Since adiabatic efficiency is essentially a ratio of mass-averaged total pressure and total temperature, Figure 6 - 7 provides another interesting presentation of total properties across R1 at two operating conditions – peak efficiency and near-stall. This time, results from the before-mentioned RANS solution are included for additional comparison. The CFD results were obtained by mass-averaging across the blade pitch at each of 46 radial locations (grid was 152-axial by 46-radial by 49-blade-to-blade). The agreement shown in Figure 6 - 7 provides further evidence of the adequacy of the SLCC predictions.

a. 98.6% Nc, peak efficiency   b. 98.6% Nc, near stall
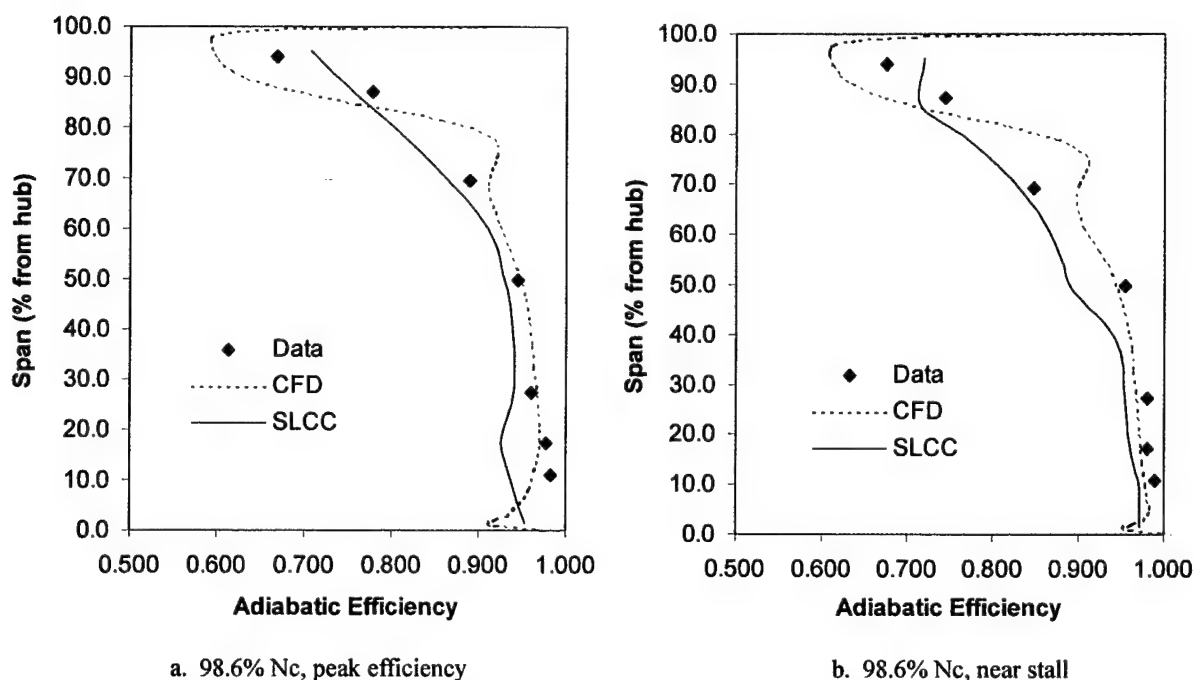
Figure 6 - 7 Spanwise distribution of efficiency across R1

While the total temperature and total pressure comparisons are favorable (Figures 6-1 –

6-7), they only tell part of the flow-field story. The two-stage fan data provided static pressure

information at the hub and tip casings only. Static pressure taps were located at several

circumferential positions at the LE and TE of both stators, and at 12 axial locations in the tip

casing through the first rotor (R1). Thus, the CFD results across R1 were most useful for

providing a basis to compare *radial predictions of static properties* from the SLCC.

Figures 6-8 and 6-9 show the axial variation in tip and hub casing static pressure,

respectively, at the peak efficiency condition predicted by all three methods – Data, CFD, and

SLCC. Again, as previously noted, the CFD predictions were only available across R1. Thus,

no CFD results are shown beyond the leading edge of S1. Note that much of the static pressure

rise in the first rotor occurs over the initial 30-40% chord due to the shock, as is seen from the tip

casing data (Figure 6 - 8). The streamline curvature method was *not* applied at axial locations

within any blade row and thus is shown only at the leading and trailing edges.

Axial static pressure comparisons at the casings were quite favorable at all operating

conditions (Figures 6-8 and 6-9 are representative). A notable exception occurred at the hub

entrance to S1 where the measured static pressure was 7-9 psia higher than that predicted by

either numerical simulation. It is possible that the measurement here included effects from a

vortex rolling up around the vane at this location, and hence measured some pressure between

static and total (total was 35-37 psia in this region – see Figures 6-3 and 6-6). If the

measurement is an accurate representation of the static pressure at the S1 LE, then neither

simulation correctly captured the effects of whatever phenomenon is taking place. Regardless,

results from the sensitivity study (Section 5.4) demonstrated that at least with respect to overall

global parameters, performance prediction in the hub region was far less critical than at any other

place in the machine.
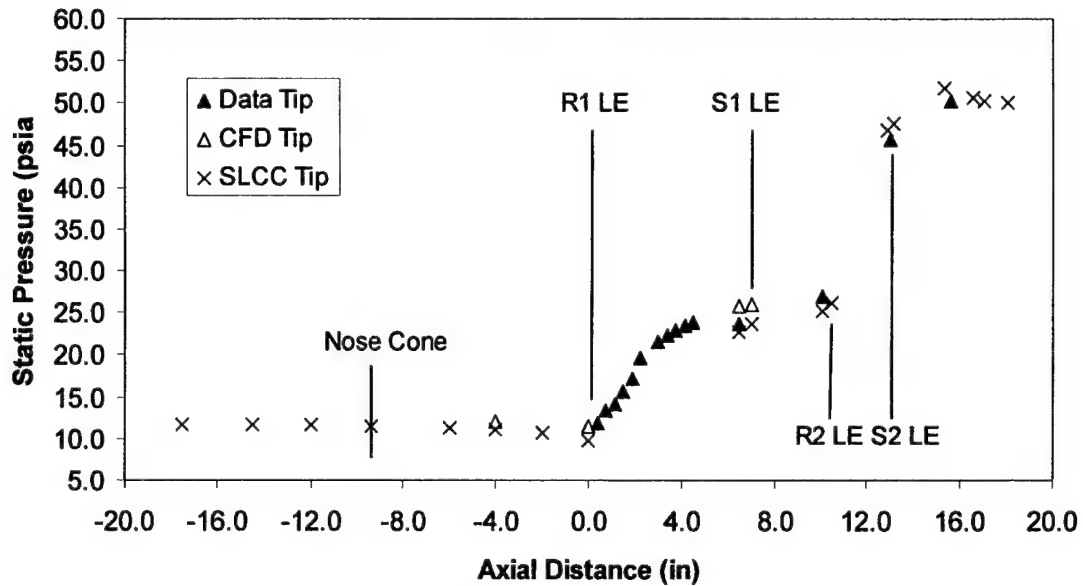
Figure 6 - 8 Axial variation in tip casing static pressure at peak efficiency, 98.6% Nc
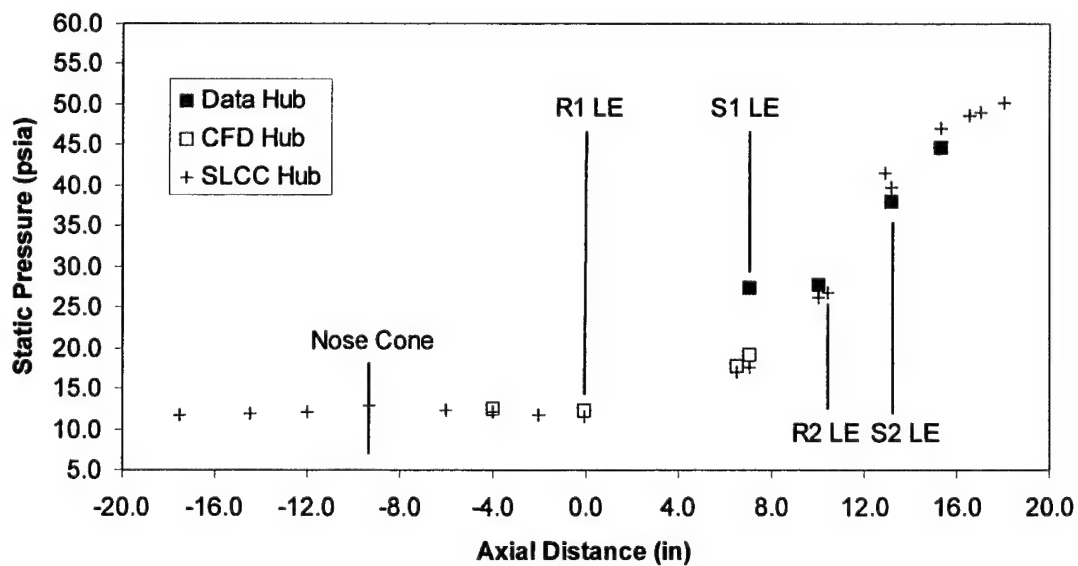
Figure 6 - 9 Axial variation in hub casing static pressure at peak efficiency, 98% Nc

To ensure reasonable fidelity of the radial velocity profile, SLCC predictions were compared to those from the CFD analyses (Hah, et al., 1998). Results showing meridional velocity comparisons across R1 at peak efficiency and near-stall are provided in Figures 6-10 and 6-11, respectively. As mentioned, the CFD results were obtained by mass-averaging across

a. R1 leading edge

b. R1 trailing edge
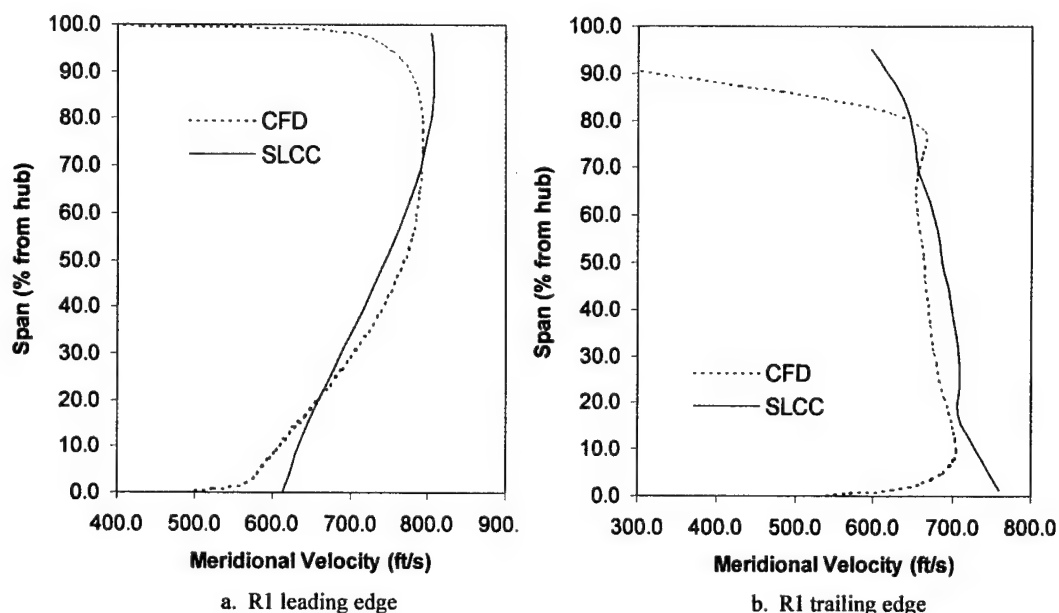
Figure 6 - 10 Radial variation of meridional velocity across R1 at peak efficiency, 98.6% Nc

a. R1 leading edge

b. R1 trailing edge
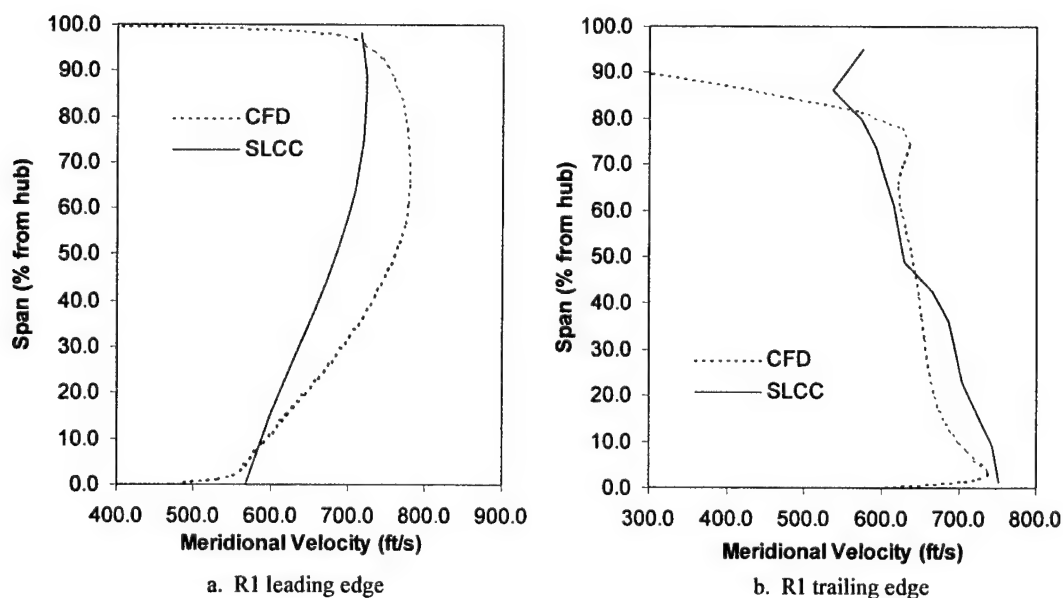
Figure 6 - 11 Radial variation of meridional velocity across R1 at near stall, 98.6% Nc

101

the blade pitch (49 stations) at each of 46 radial locations. While the SLCC captured the general velocity trends from hub to tip, the inadequacies of using an inviscid approach are apparent. The effects of the complex flow field, most notably endwall boundary layers, tip leakage vortex, and interactions with shocks, are not properly accounted for with the SLCC approach. It is not surprising that the CFD solutions show a more pronounced velocity profile at the R1 LE. At the trailing edge, the effects of the tip leakage vortex and endwall interactions are readily observed in the CFD solution. The simple endwall displacement thickness and blockage models of the SLCC are insufficient. These will be discussed further in Section 6.3.

6.2 Overall and Radial Performance – 85% Speed Results

One of the objectives of the present work was the incorporation of physics-based loss models to improve the general applicability of the SLCC to modern fan designs. Consequently, an expected result of the improvements was the elimination of much of the manual calibration of model parameters. Previous applications of the unmodified SLCC within the TEACC required radial specification of loss, deviation, and blockage parameters at each operating condition to achieve satisfactory results (Hale, et al., 1999, and Hale and O'Brien, 1998).

The results shown in the previous section, achieved with a much reduced level of model calibration (described in Section 5.3), clearly demonstrate the effectiveness of the improvements. To illustrate further, parameter adjustments at the 85% speed conditions were limited to those presented below. The following steps outline the procedure used at 85.0% Nc to obtain all the results presented in this section:

- The developing inlet boundary layer (up to the R1 entrance) was analyzed similar to that described in Section 5.2 using an inlet velocity of 437 ft/s (from station 10 measurements).

102

The analysis revealed negligible changes to the results presented in Section 5.2. Hence, *no changes were made to the blockage estimates up to the R1 LE* (SLCC stations 1 – 9).

- The remainder of the blockage estimates were decreased as follows:

  ➤ Annulus wall blockage through the machine was decreased 0.02 from their design values at each location (stations 10 – 19). Design values were provided by Steenken, 2000.

  ➤ Tip leakage blockage, also discussed in Section 5.2, was halved from the values used at the design condition. Thus, resulting area reductions in the outermost streamtube were 30%, 25%, and 15% at the exits of R1, S1, and R2, respectively.

- The R1 and R2 tip loss parameters (see Equation 3-3) were adjusted to provide increments of tip loss coefficients slightly less than, but comparable to, the values at 98.6% Nc.

- The global "adddev" parameter was adjusted to match overall mass-averaged total temperature ratio at each of five operating conditions.

It is emphasized that "adddev" was the only parameter adjusted at each operating condition to achieve the results presented below. The blockage and tip loss adjustments were made at peak efficiency and left unchanged throughout the operating range at 85.0% Nc. This represents a significant reduction in the calibration process from that previously required.

As with the design speed, both overall and radial results are presented below for 85.0% Nc at five operating conditions ranging from near-choke to near-stall. Overall performance comparison is provided in Figure 6 - 12, which also indicates the five operating conditions. The figures presented in this section parallel those presented at design speed, Figures 6-2 – 6-11. In general, performance predictions compare quite favorably with the estimates obtained from CFD and the experimental data. Note that the CFD grid was slightly different at 85.0%

103

(150-axial by 40-radial by 49-blade-to-blade). A more detailed analysis and discussion of results

follows in Section 6.3.
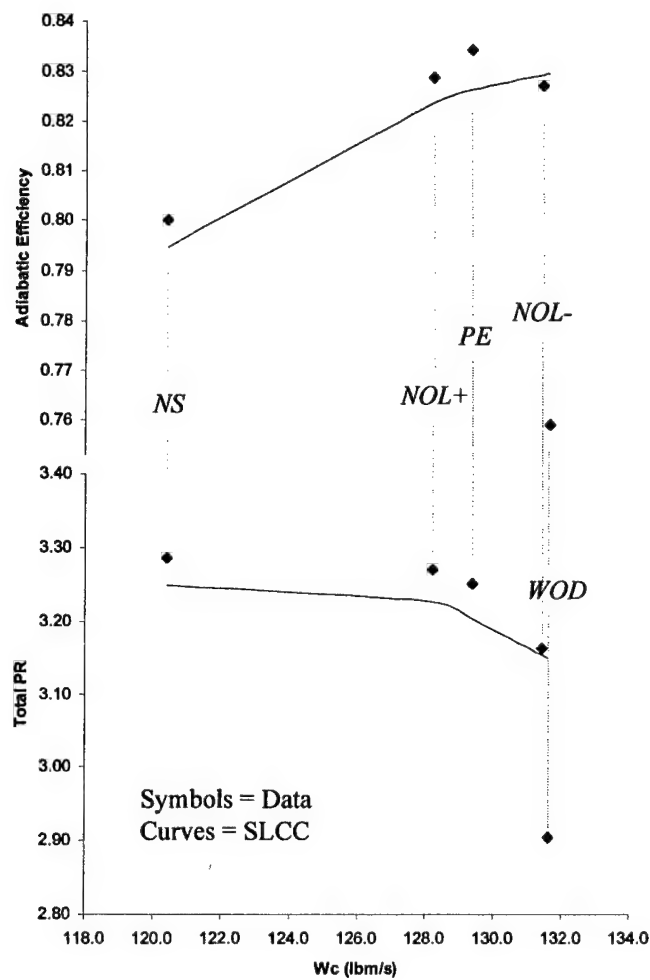
Figure 6 - 12 Overall performance comparison of CRF two-stage fan at 85.0% Nc
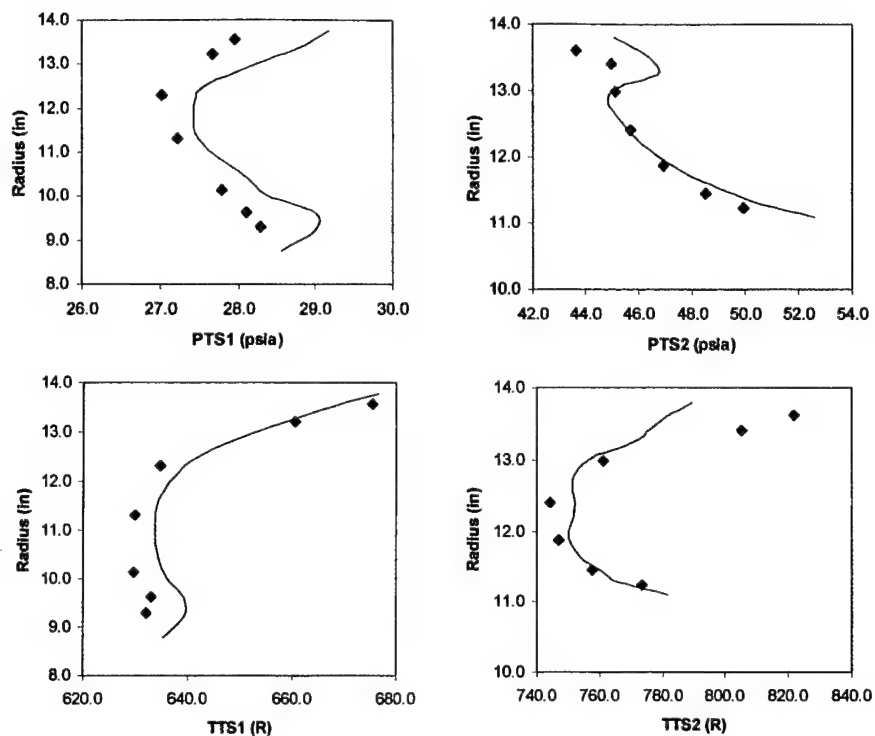
Figure 6 - 13 Radial comparison at 85.0% Nc, WOD (symbols = data)
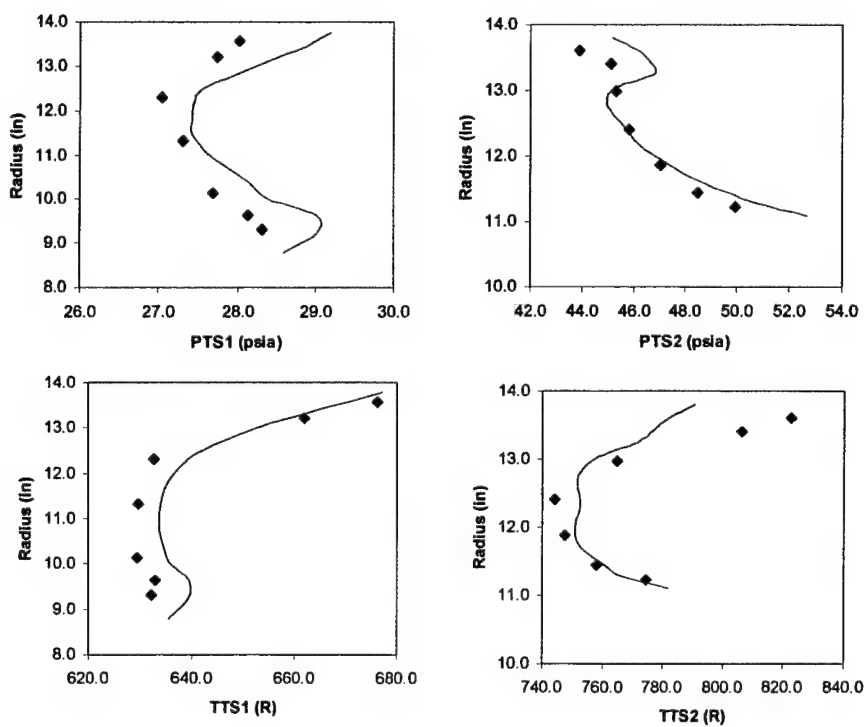
Figure 6 - 14 Radial comparison at 85.0% Nc, NOL- (symbols = data)

105
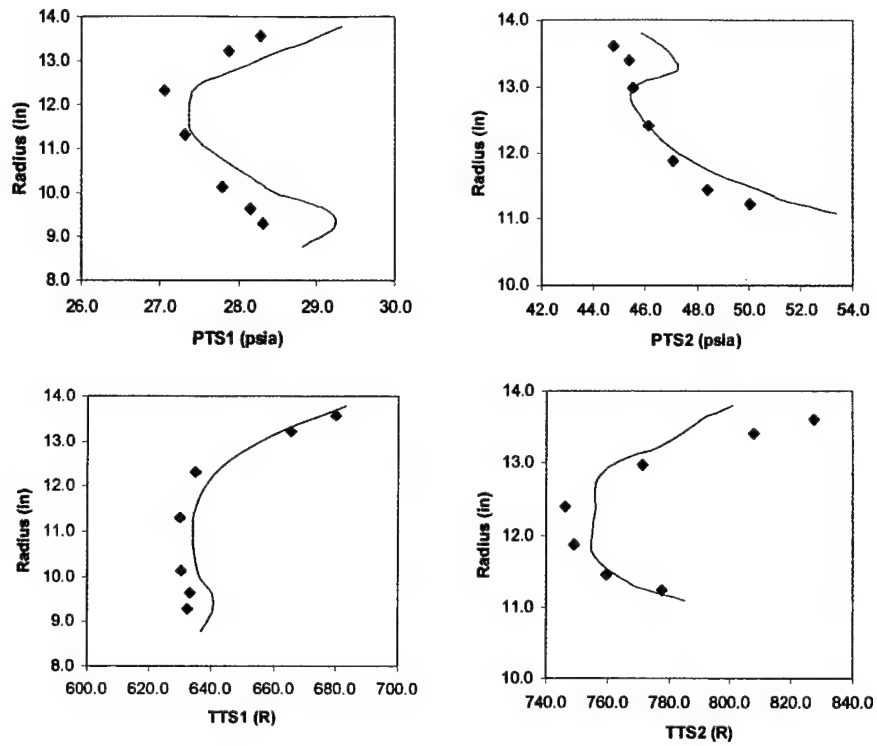
Figure 6 - 15 Radial comparison at 85.0% Nc, PE (symbols = data)
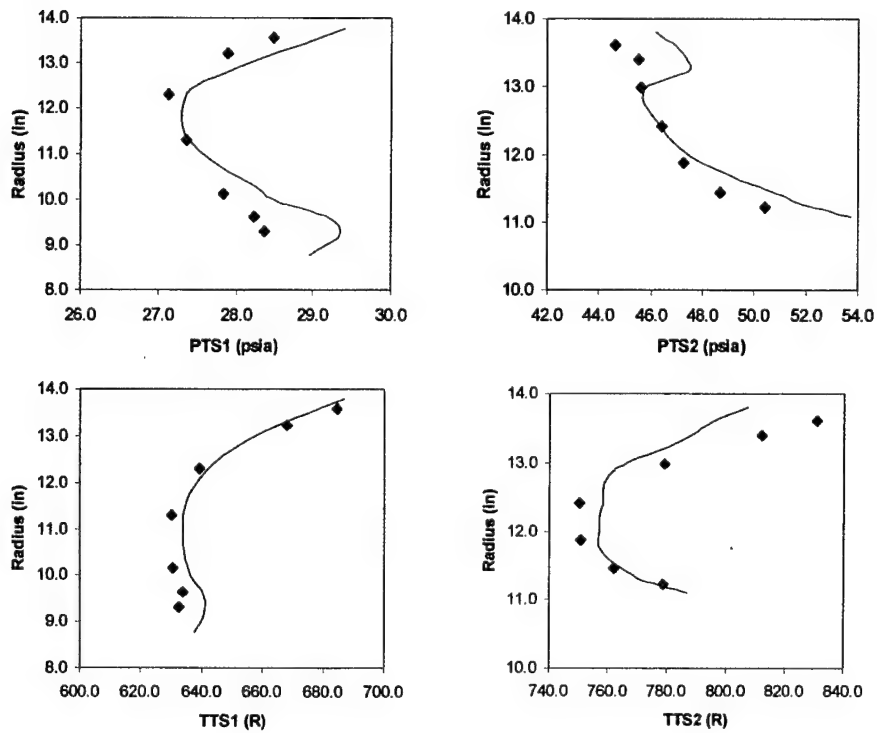
Figure 6 - 16 Radial comparison at 85.0% Nc, NOL+ (symbols = data)

106
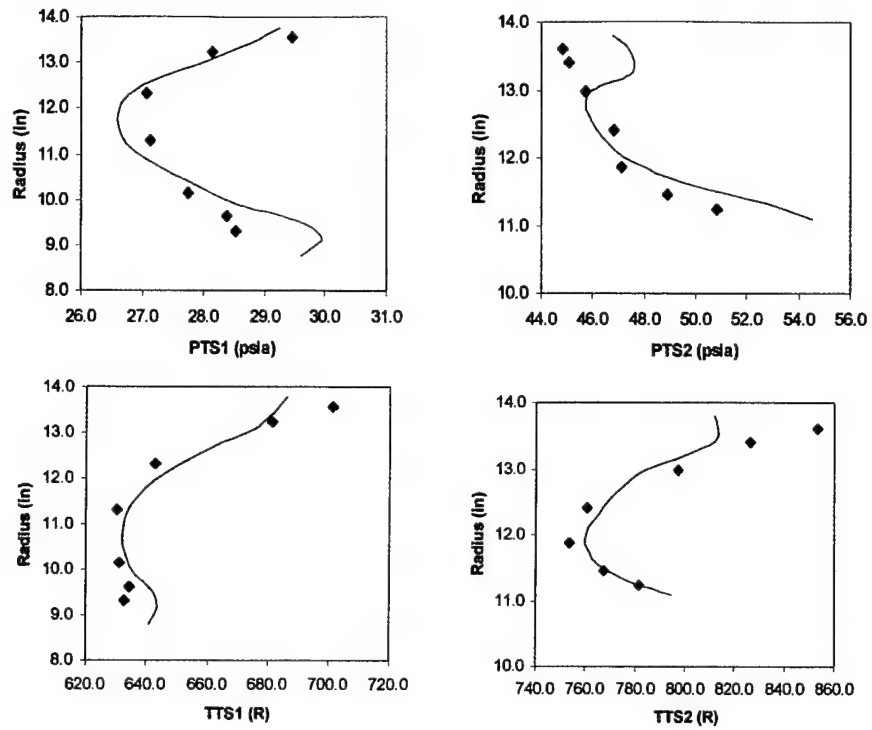
Figure 6 - 17 Radial comparison at 85.0% Nc, NS (symbols = data)

a. 85.0% Nc, peak efficiency

b. 85.0% Nc, near stall
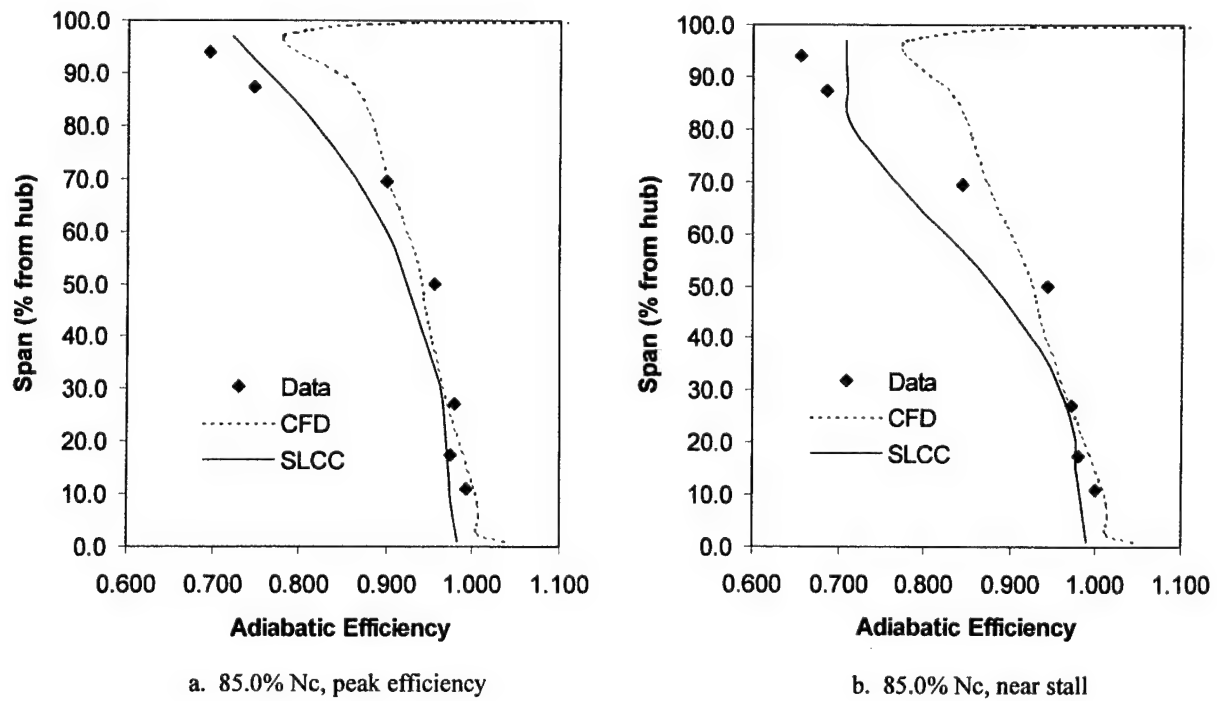
Figure 6 - 18 Spanwise distribution of efficiency across R1

107
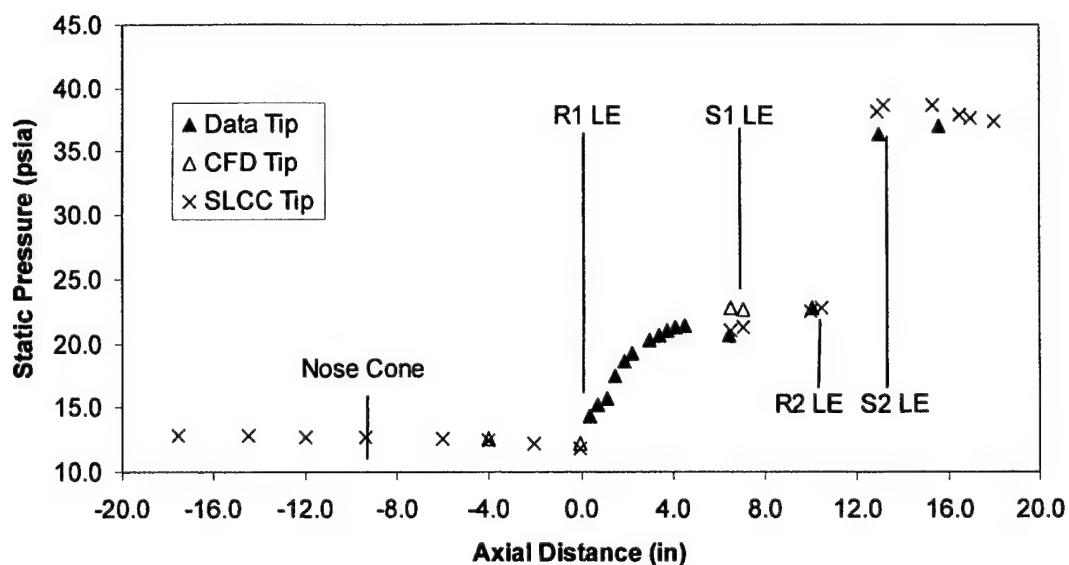
Figure 6 - 19 Axial variation in tip casing static pressure at peak efficiency, 85.0% Nc
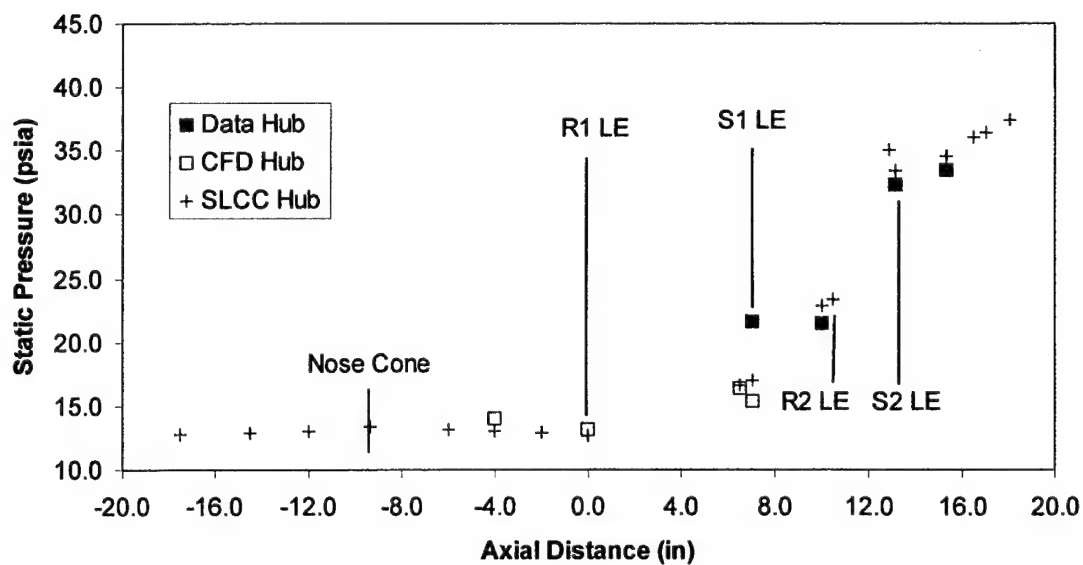
Figure 6 - 20 Axial variation in hub casing static pressure at peak efficiency, 85.0% Nc

a. R1 leading edge

b. R1 trailing edge
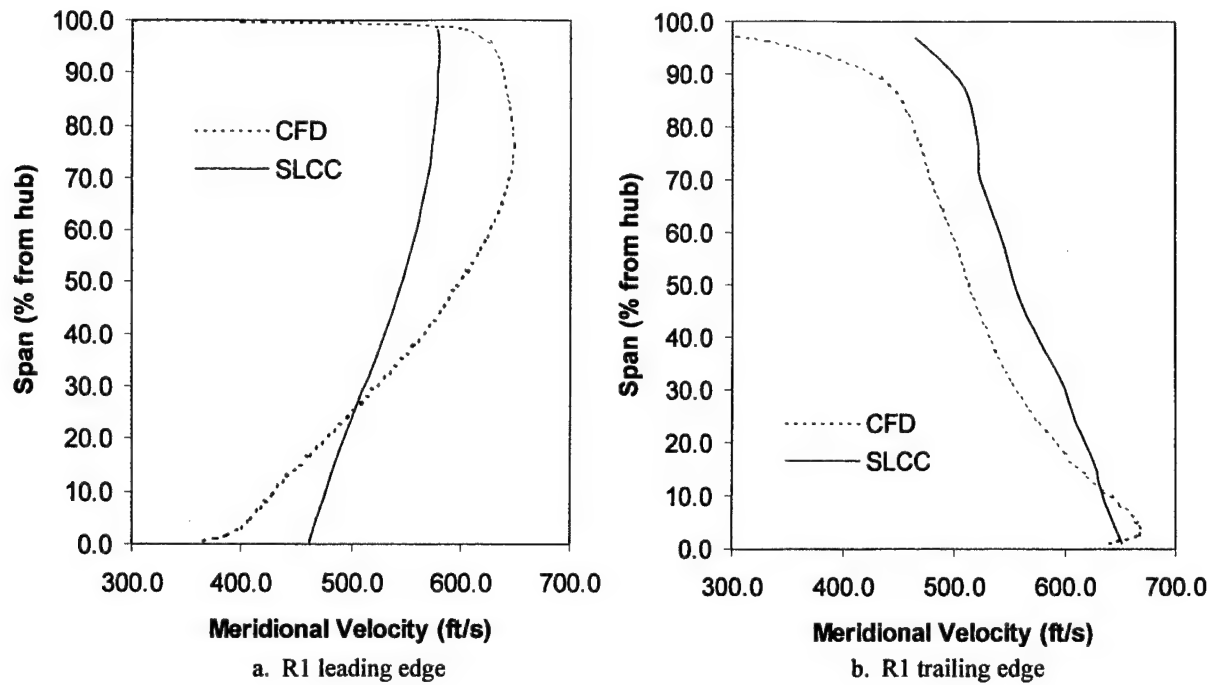
Figure 6 - 21 Radial variation of meridional velocity across R1 at peak efficiency, 85.0% Nc

a. R1 leading edge

b. R1 trailing edge
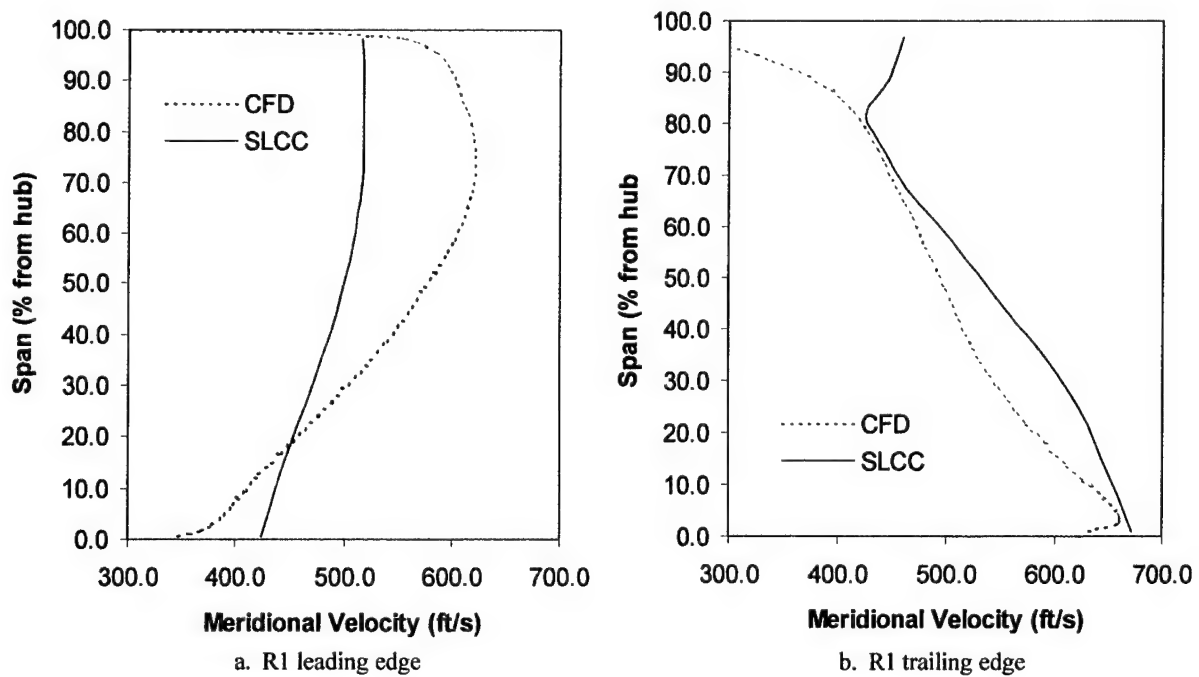
Figure 6 - 22 Radial variation of meridional velocity across R1 at near stall, 85.0% Nc

109

6.3 Analysis and Discussion of Results

Since improvement of loss modeling was key to the present work, the first part of this section deals with results relative to loss estimation. Figure 6 - 23 shows the predicted loss characteristics at three *blade sections* of R1 and R2 – near-hub, mid-span, and near-tip – at both speeds examined here. Recall that the operating conditions indicated on the plots are for *overall*, mass-averaged machine performance. The abscissa of each of the four plots is presented as $(i - i_{min})$ which provides a good indicator of section loading (flow turning). The following observations are made:

- At both speeds, the tip region of R1 is more highly loaded than the rest of the span, and not surprisingly, has the highest losses (due to strong shocks, secondary losses, and interactions).

- For R2, the loading is shifted more towards the mid-span region, especially at 85.0% speed.

- In all cases, the hub sections of both rotors are relatively unloaded, consistent with the high throughflow velocities in this region (see Figures 6-10 and 6-11, 6-21 and 6-22).

- At 85.0% Nc, both rotors are subjected to higher incidence angles at the given overall operating conditions. For R1, this is not surprising since the fan contained no inlet guide vanes. The simple velocity triangle relationships shown in Figure 6 - 24 at the near-stall operating condition indicate increases in β_1 (inlet relative flow angle) of about 4.0 degrees over the entire span, consistent with the top two plots in Figure 6 - 23. For R2, the increased incidence at part-speed was not necessarily expected given the upstream influence of R1 and S1. Indeed, relative to R1, the increase in incidence was small.

To further verify the loss model improvements (from that demonstrated in Chapter 4), Figures 6-25 and 6-26 are provided. These figures show the components of the near-tip loss characteristics of both rotors, both speeds shown in Figure 6 - 23. The three components

110
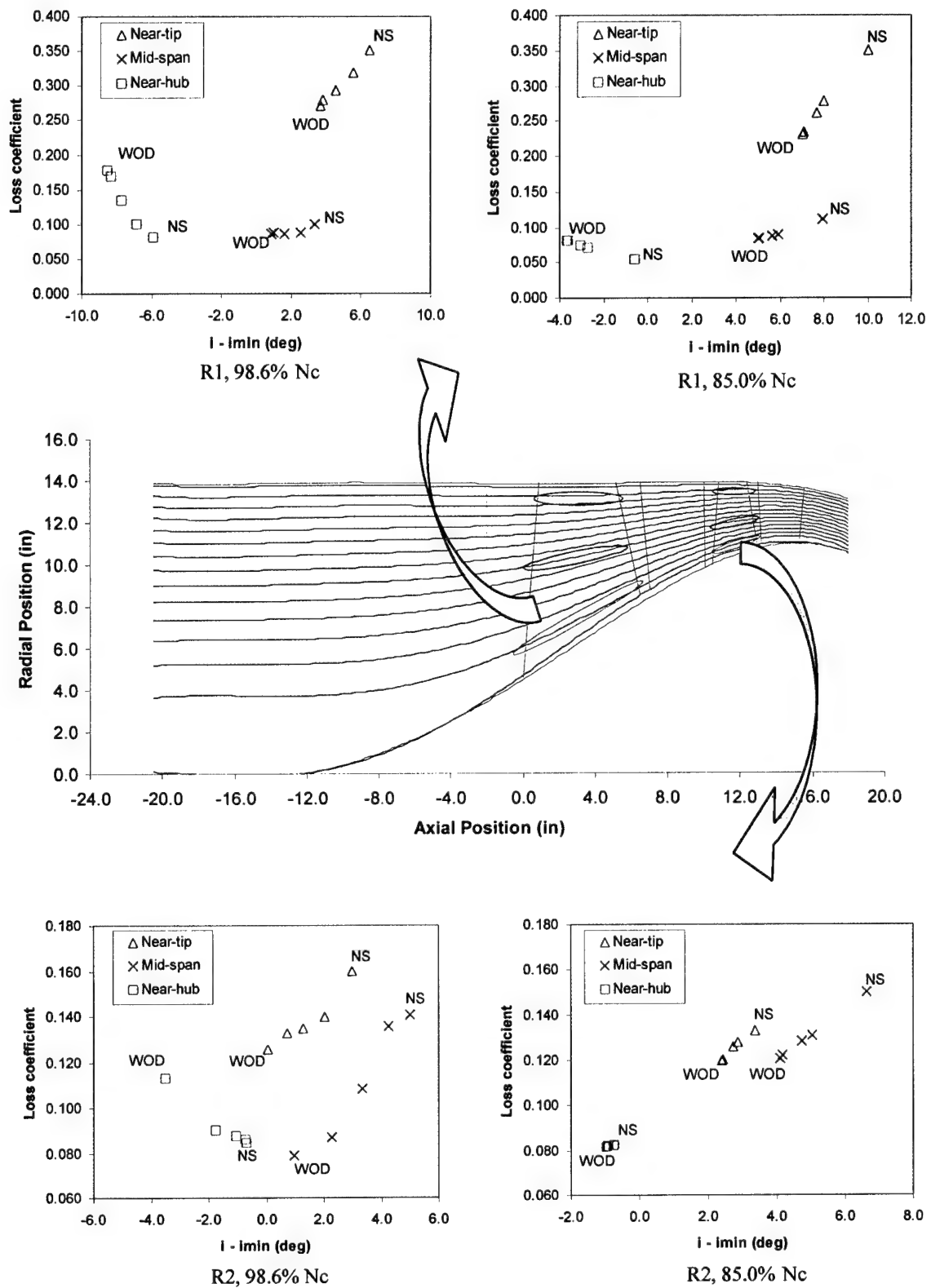
Figure 6 - 23 Predicted R1 and R2 blade section loss characteristics

111

	98.6% Nc			85.0 % Nc		
	Vm1 (ft/s)	U1/Vm1	B1 (deg)	Vm1 (ft/s)	U1/Vm1	B1 (deg)
near-tip:	719.42	2.129	64.84	516.70	2.539	68.50
mid-span:	698.83	1.635	58.55	507.77	1.926	62.56
near-hub:	599.63	1.153	49.08	446.32	1.329	53.03

Inlet velocity triangles at R1 near-tip (drawn to scale)

$$\beta_1 = Tan^{-1}\left(\frac{U_1}{V_{m1}}\right)$$

———— 98.6% Nc. Near-tip

- - - - - - 85.0% Nc. Near-tip
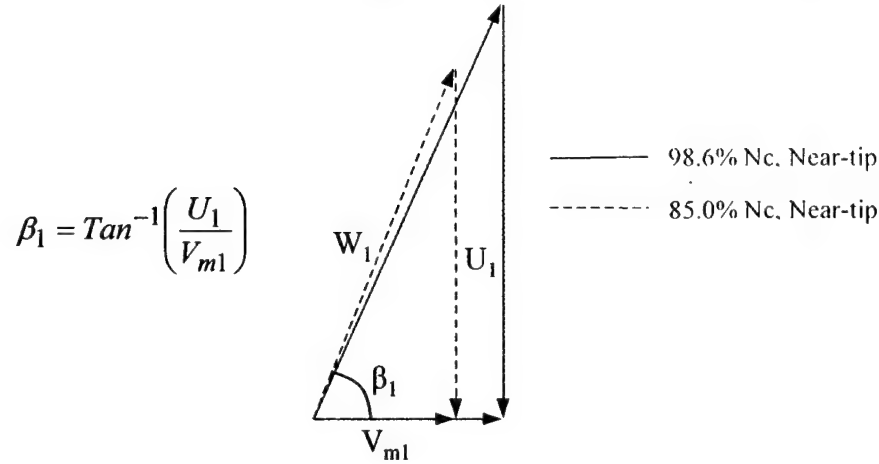
Figure 6 - 24 Near-stall inlet velocity triangle relationships at three R1 blade sections (same as Figure 6 - 23)

indicated in Figures 6-25 and 6-26 are the same as those used in Figure 3 - 2. For reference, the range of relative Mach number at the shock system entrance, M_{elev}, is also shown on each plot. Again, the following observations are made:

- In all cases, the profile loss of each rotor was independent of loading. This seems reasonable given the low-turning, precompression tip sections of both rotors, and the recent results of Konig, et al., 1996 and Bloch, et al., 1999 (presented in Section 2.1). Consequently, the section overall loss characteristic (and hence, efficiency) is defined by the shock loss and secondary loss.
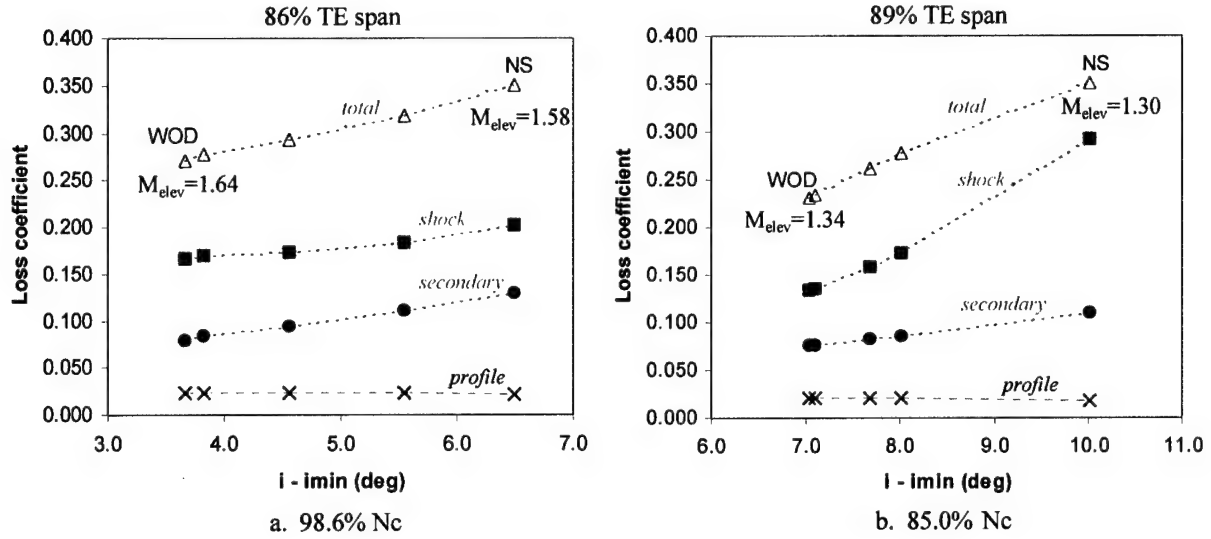
Figure 6 - 25 Loss components across R1 near-tip section (same as Figure 6 - 23)
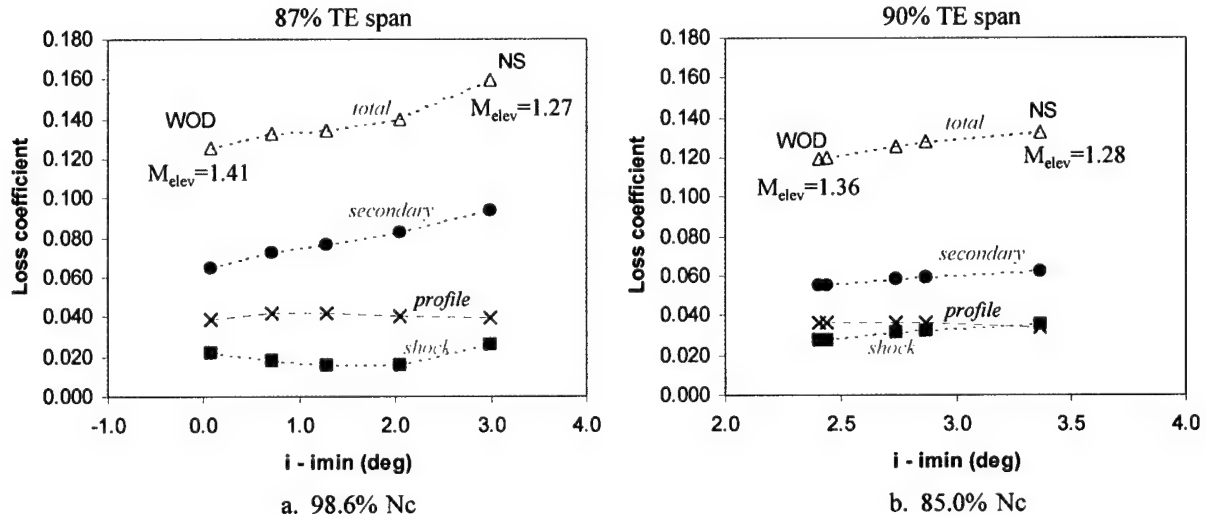
Figure 6 - 26 Loss components across R2 near-tip section (same as Figure 6 - 23)

- With the possible exception of the R1 near-stall (NS) shock loss coefficient at 85.0% Nc (Figure 6 - 25b, discussed below), the magnitudes of the loss components appear to be quite reasonable. Most important for purposes of the present work, the trends are accurate.

- Improvements resulting from the simple modification made to the tip loss secondary model, Equation (3-3), are evident. The tip loss increases with loading as would be expected, and

113

appears quite reasonable relative to the CFD results. Those results showed a strong tip leakage influence down about 20% from the tip at design speed (Figures 6 – 10b and 6 – 11b) and about 15% from the tip at 85.0% speed (Figures 6 – 21b and 6 – 22b).

- Table 6 - 1 provides a comparison of the predicted near-tip shock loss coefficients (same locations as those in Figures 6-25 and 6-26) at WOD and NS to those that would result from a normal, attached shock assumption (original MLH model) at the same Mach number.

  ➤ The R1 tip section is highly loaded at both speeds (Figure 6 - 25), even when the overall machine is operating at near-choke (WOD). Because the new model includes detached bow shock loss due to LE bluntness, the R1 predicted shock loss from the modified model was greater than that predicted by the original.

  ➤ For R1, 85.0% Nc (Figure 6 - 25b), the predicted loss from the modified model is somewhat suspect (especially at the NS condition), due predominantly to the simplified bow shock model (Equation 4-9). At near-stall, the predicted bow shock loss was 0.258, approximately 88% of the shock loss. While the high section loadings would drive the shock towards increased detachment distance (and hence, increased bow shock loss), the magnitude of that loss would likely be less than that predicted, especially given the thin, precompression airfoil at the tip section (Figure 5 - 3).

  ➤ The loading at the R2 tip section, for both speeds (Figure 6 - 26), is significantly lower than that for R1. For example, note in Figure 6 - 26a that the tip region of R2 operates at the i_{min} for the 98.6% Nc, WOD condition. Consequently, the predicted shock loss from the new model is about half what it would be for a normal shock (consistent with Figure 4 - 5a). As the section loads up, the new model predicts an ϖ_{shock} increase of 0.004, while the estimate from the original model drops significantly (from 0.044 to 0.016). While

114

Table 6 - 1 Comparison of near-tip shock loss coefficient from modified and original models

Rotor, Speed	Overall Operating Condition	Melev	$\varpi_{shock,\,mod}$ (Boyer)	$\varpi_{shock,\,org}$ (MLH)	Difference (Boyer – MLH)
R1, 98.6%	WOD	1.64	0.166	0.120	0.046
	NS	1.58	0.202	0.097	0.105
R1, 85.0%	WOD	1.34	0.134	0.028	0.106
	NS	1.30	0.292	0.021	0.271
R2, 98.6%	WOD	1.41	0.022	0.044	-0.022
	NS	1.27	0.026	0.016	0.010
R2, 85.0%	WOD	1.36	0.028	0.032	-0.004
	NS	1.28	0.036	0.017	0.019

non-physical, this result is expected from a single, normal, attached shock assumption (see discussion, Section 4.4.1).

Finally, Figure 6 - 27 is provided to demonstrate the dominance of the shock loss in this high-performance fan, even at part-speed (85.0% Nc). The figure was obtained from the SLCC predictions by integrating the individual, mass-weighted, loss components (profile, shock, and secondary) from hub to tip. As is evidenced in Figure 6 - 27, and discussed throughout this report, shock loss is the major contributor to overall loss in highly transonic fans.

6.3.1   Overall Results

With the exception of the near-choke operating condition (WOD), most notably at 85.0% (Figure 6 - 12), overall machine, mass-averaged results compared quite favorably to those determined experimentally. Surely, the correct trends were well represented, not only from a total property standpoint (Figures 6-1 and 6-12), but also for the hub and tip casing axial static pressure distribution shown in Figures 6-8, 6-9 and 6-19, 6-20.
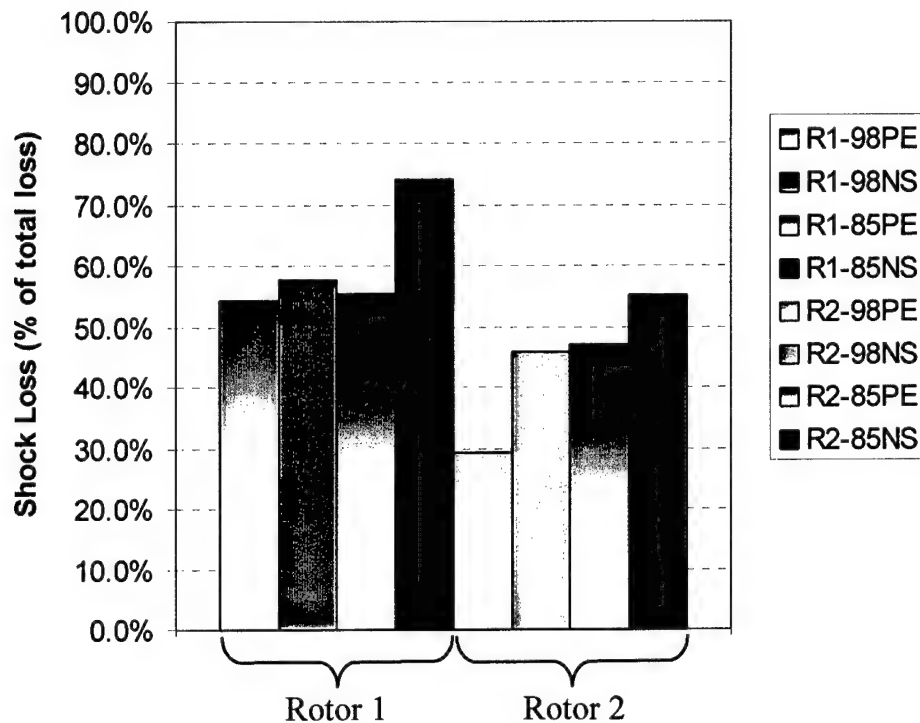
Figure 6 - 27 SLCC-predicted mass-averaged shock loss of both rotors of CRF fan at different speeds and operating conditions

At the design speed, the overall peak efficiency condition was clearly captured, evidenced by Figure 6 - 1. As the fan approached stall at this speed, the data show a more pronounced drop in efficiency than do the SLCC results, but regardless, the proper trending is encouraging. The trending is also very good at 85.0% Nc, although a slight discrepancy occurred relative to the location of the peak efficiency condition (Figure 6 - 12). Clearly, the model did not capture the WOD condition at 85.0% speed, indicative of misrepresenting the choking incidence. This will be discussed further as part of the conclusions and recommendations.

6.3.2   Radial Results

The real proof of the adequacy of the present approach lies in the radial performance comparisons. Since the streamline curvature approach relied on accurate incidence angle determination (for the models and correlations), faithful representation of the radial inlet velocity profile was essential. Thus, the following points discuss the radial comparisons, starting with the inlet profiles and working through the machine.

- At 98.6% Nc, within the limitations of the SLC method, the predicted radial velocity at the R1 inlet was reasonable, evidenced in Figures 6-10 and 6-11 through comparison with the CFD results. At peak efficiency, the maximum difference between the two methods was approximately 100 ft/s and occurred in a small region at the tip (Figure 6 - 10), while at near-stall, the maximum difference was about 80 ft/s near mid-span (Figure 6 - 11). The discrepancies between the SLCC and CFD results at 85.0% Nc (Figures 6-21 and 6-22) are similar to those at design speed. The maximum difference was about 80 ft/s at PE and 100 ft/s at NS – both occurred at approximately 70% of the R1 blade span.

- With the exception of the near-tip region (discussed below), and despite the discrepancies in R1 inlet velocity just noted, the R1 exit velocity profiles predicted by the two methods agreed remarkably well (again, Figures 6-10, 6-11 and 6-21, 6-22). Additionally, the spanwise efficiency comparisons (data, CFD, and SLCC) shown in Figure 6 - 7 for 98.6% and Figure 6 - 18 for 85.0% were also quite favorable. Hence, the blockage, loss, and deviation estimates based on incidence must be reasonably accurate at the R1 exit station. This seems to indicate that the SLCC method is somewhat robust in tolerating LE incidence discrepancies. From the discussion presented at the beginning of Section 3.4, missing the inlet velocity by 100 ft/s

117

would result in a misrepresentation of the incidence angle by about three degrees. It appears that the calibration process accounted for inaccuracies in incidence angle determination.

- Also quite evident in the R1 exit velocity profiles is the inability of the SLCC to correctly capture the tip leakage vortex effects. Most notably, at the design speed (Figures 6-10b and 6-11b), the CFD results show the influence of tip leakage some 20% into the R1 span from the tip. Further, the tip leakage influence upstream is clearly demonstrated in the CFD results presented at the R1 leading edge (Figures 6-10, 6-11 and 6-21, 6-22). The total properties agree quite well (see for example, Figures 6-3 and 6-6 for 98.6% Nc) in the near tip region. This suggests that a blockage model offers potential, but must be more sophisticated than the present one. Suggestions for improvement are presented in Chapter 9, Recommendations.

- Figures 6-28 and 6-29 are provided to help summarize the interstage radial SLCC-data comparisons. The figures compare the S1-R2 spanwise efficiency as determined from the CRF measurements and the SLCC predictions. The comparisons are made on the basis of measurements/SLCC calculations at the leading edges of S1 and S2. The ordinate of the plots is % S2 span from hub. Not surprising, the biggest discrepancies occur in the near-tip regions (most notably at 85.0% speed). As seen in Figures 6-13 – 6-17, the total temperature in the tip region (and hence, turning) is underpredicted, while the total pressure is overpredicted at all operating conditions for 85.0% Nc. This seems to indicate that the predicted R2 near-tip loading (Figure 6 - 23) might be low; i.e., the actual incidence angle is greater than that predicted. Again, this would be consistent with overpredicted velocity estimates in this region due to the inadequacy of the tip secondary flow representation just discussed.

118

a. 98.6% Nc, peak efficiency

b. 98.6% Nc, near stall
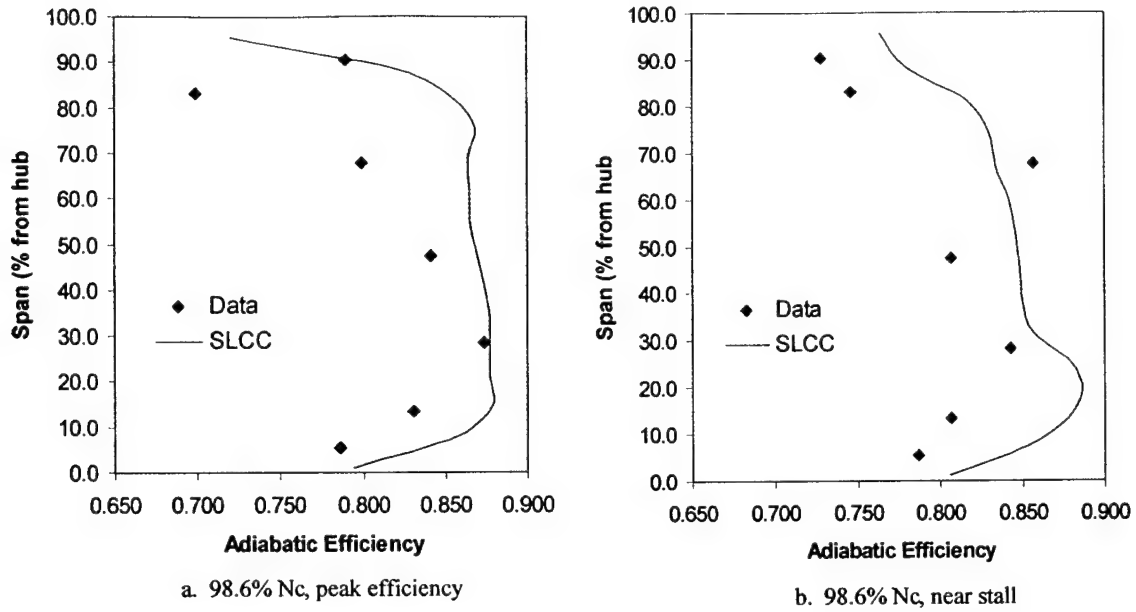
Figure 6 - 28 Spanwise distribution of efficiency across S1-R2, 98.6% Nc

a. 85.0% Nc, peak efficiency

b. 85.0% Nc, near stall
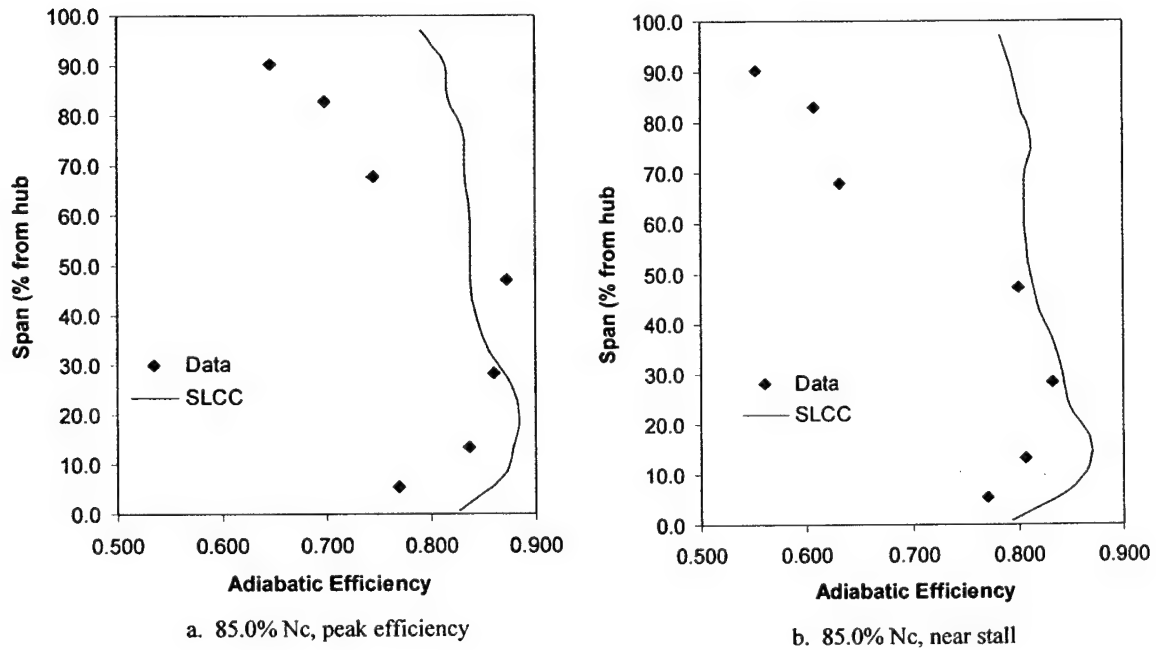
Figure 6 - 29 Spanwise distribution of efficiency across S1-R2, 85.0% Nc

119

7. Proposed Application of Improved SLCC

7.1 Overview

Hale, et al., 1994, and Hale, 1996, developed a modeling approach that involved novel application of the streamline curvature method used in the present work. They modified a general-purpose, 3-D, CFD flow solver (Bush, et al., 1998) to accept turbomachinery source terms estimated from the SLCC. The grid used by WIND (the flow solver) is fixed, while the SLCC grid is updated each timestep as a function of the local flow conditions across each blade row. The resulting Turbine Engine Analysis Compressor Code (TEACC), shown schematically in Figure 7 - 1, can be used to analyze steady and time-varying inlet distortion through solution of the compressible, time-dependent, three-dimensional Euler equations. The SLCC-provided source terms represent the effects of the blades/vanes. The TEACC has been applied to numerous single- and multi-stage compression systems for distortion analyses (Hale, et al., 1999; Hale and O'Brien, 1998).

The SLCC modified in the present work was selected largely on the basis of its application in the TEACC. Hale developed the TEACC specifically as an alternative numerical approximation to address complex engine inlet-integration issues. As presented in Chapter 2, full turbomachinery CFD schemes have practical limitations in terms of required computational resources and turbulence and transition modeling. This chapter provides a brief overview and assessment of the overall TEACC approach. Emphasis is placed on source term determination via the SLCC. A discussion is presented regarding improvements to the TEACC approach relative to the lessons learned from the present work.

3D Flow Solver

NPARC or WIND

Source Terms: Forces and Shaftwork

SLCC

Dynamic Distortion Analysis

3D Compression System Model
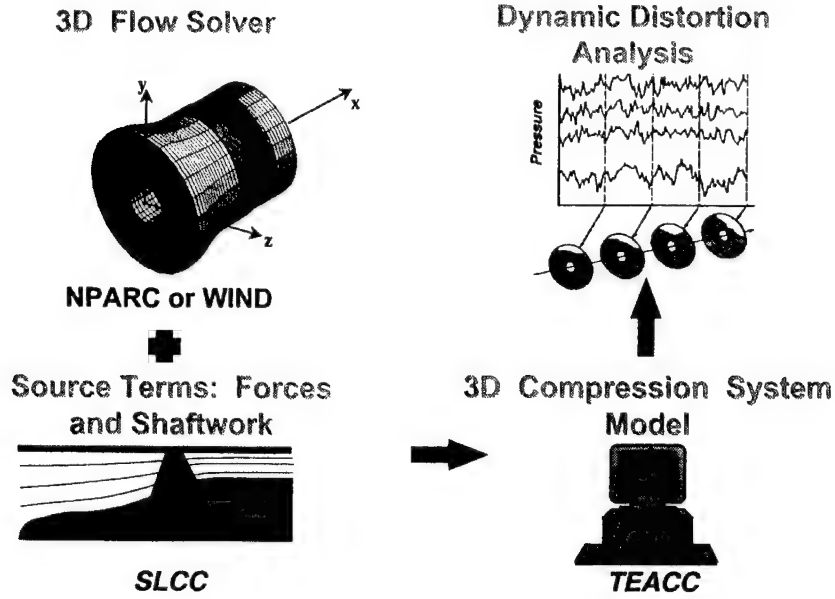
TEACC

Figure 7 - 1 Overall TEACC methodology (Hale, et al., 1999)

7.2 Overall Approach

The simplified governing equations – assuming inviscid flow and thermally and calorically perfect gas – are presented below in Cartesian coordinates:

$$\frac{\partial \bar{Q}}{\partial t} + \frac{\partial \bar{E}}{\partial x} + \frac{\partial \bar{F}}{\partial y} + \frac{\partial \bar{G}}{\partial z} = \bar{S} \qquad (7-1)$$

where :

$$\bar{Q} \equiv \begin{bmatrix} \rho \\ \rho u \\ \rho v \\ \rho w \\ \rho e \end{bmatrix} \qquad \bar{E} \equiv \begin{bmatrix} \rho u \\ \rho u^2 + P \\ \rho uv \\ \rho uw \\ (\rho e + P)u \end{bmatrix} \qquad \bar{F} \equiv \begin{bmatrix} \rho v \\ \rho vu \\ \rho v^2 + P \\ \rho vw \\ (\rho e + P)v \end{bmatrix} \qquad \bar{G} \equiv \begin{bmatrix} \rho w \\ \rho wu \\ \rho wv \\ \rho w^2 + P \\ (\rho e + P)w \end{bmatrix} \qquad \bar{S} \equiv \begin{bmatrix} S_m \\ S_{Fx} \\ S_{Fy} \\ S_{Fz} \\ S_{SW} \end{bmatrix}$$

and :

$$e \equiv \hat{u} + \frac{u^2 + v^2 + w^2}{2}$$

The TEACC solves for the conservation variables, $\bar{Q}$, at each grid point. Note that the grid extends into and through each blade row (illustrated in Figure 7 - 2). The volumetric

121

turbomachinery source terms, $\bar{S}$, are bleed flow rates, forces in the x, y, and z directions, and rates of shaft work. The technique for determining the source terms is described in the next section.

Solution of Equation (7-1) requires a full set of boundary conditions, as well as initial conditions. Initial conditions are provided by the streamline curvature code operating on a grid that extends to the boundaries of the 3-D, fixed TEACC grid. The inflow boundary condition (BC) is based on reference plane characteristics requiring specification of inlet total pressure and temperature. Inlet flow directions are assumed to be normal to the boundary because the grid is constructed so that the inlet plane is normal to the machine centerline. The exit BC is either overall mass flow rate or a variable exit static pressure (single value is specified at one exit node and the profile just upstream is imposed) – both support the exit profile of strong swirl. Wall boundary conditions are assumed to be slip walls – normal velocity components are set equal to zero at solid walls. In the circumferential direction, a periodic (wrap-around) BC is used, where the seam of the grid is overlapped by one circumferential segment.

The grid (or mesh) and numerical scheme are both important aspects of any CFD application. Dunham, 1998, provides a useful summary of various strategies in his "Review of Turbomachinery CFD," Chapter 1.0 of AGARD-AR-355. The TEACC uses a fixed, O-type grid constructed along the physical interior boundaries of the turbomachinery inner and outer casing. Figure 7 - 2 provides a typical TEACC grid for a single blade row – 69 axial x 26 circumferential x 13 radial for Rotor 1B (Hale and O'Brien, 1998). The mesh must map the leading and trailing edges of each blade row. To help minimize numerical losses caused by strong axial gradients, the grid is packed through the bladed region (Figure 7 - 2). Each circumferential segment is equally spaced. Note that for "clean" inlet (no distortion) simulations, the grid spans only part of the

circumferential direction (axisymmetric assumption) and rotationally cyclic boundary conditions are used.
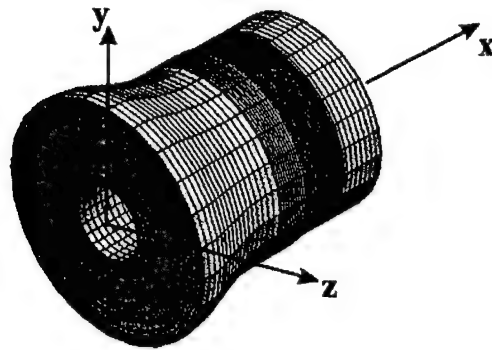
a. Three-dimensional view of grid
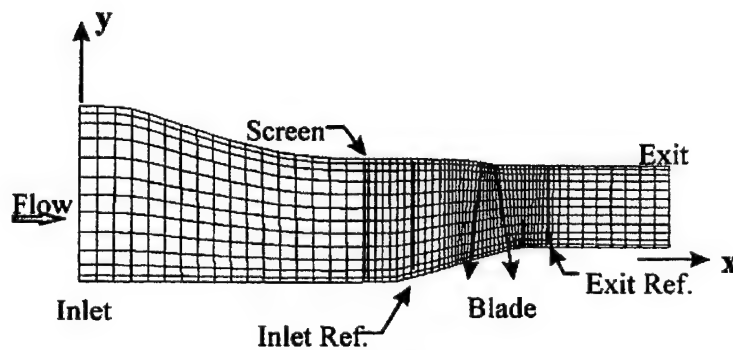
b. Circumferential slice
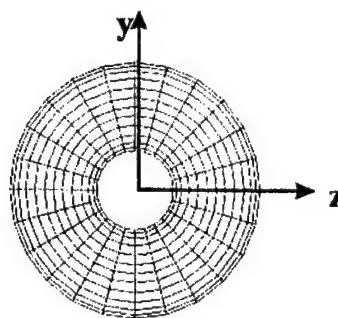
c. Axial slice

Figure 7 - 2 Grid used by TEACC for turbomachinery blade row with axial grid packed through the blades and equally spaced circumferential segments (Hale, 1996)

123

The TEACC solution procedure is flow charted in Figure 7 - 3. As discussed by Hale and O'Brien, 1998, the governing equations are discretized with central differences. The Beam and Warming implicit algorithm is incorporated to diagonalize the matrices, requiring a penta-diagonal solver. Artificial dissipation is required for stability – TEACC uses Jameson-style dissipation, quite popular for turbomachinery applications, as discussed by Dunham, 1998. Two criteria are used to verify convergence to a steady-state solution: (a) the L2 norm of the residual[1] is monitored to ensure a 3rd- to 4th-order drop in magnitude, and (b) key parameters (i.e.; mass flow rate) are monitored to verify a useful engineering solution (mass flow changes less than 0.01 as the TEACC continues to iterate).

7.3 Turbomachinery Source Terms

At the heart of the TEACC methodology is the determination of source terms (blade forces, shaft work, bleed flows) from the streamline curvature model and their distribution within the fixed-grid framework of the CFD solver. Hale, 1996, incorporated the following features to ensure the system fidelity and responsiveness needed to adequately represent complex, time-variant engine-inlet integration issues:

- The SLCC is called at *each* circumferential segment across *each* blade row.

- The 3-D solver provides boundary conditions for the SLCC at locations just upstream and downstream of each blade row. Consequently, radii of curvature must be supplied as discussed in the following paragraph.

- While the CFD grid is fixed, the SLCC grid "floats" as a function of local conditions provided by the TEACC flow field.

---

[1] A residual is the explicit portion of the discretized conservation equation - all but the time-dependent terms of Equation (7-1). The residual approaches zero at steady-state. The L2 norm of the residual is the root-mean-square of the components of the residual vector at each node.
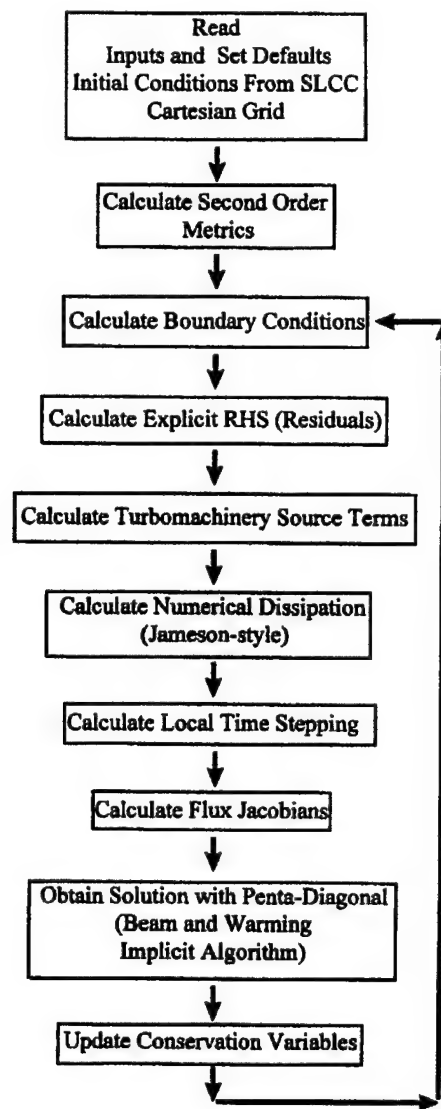
Figure 7 - 3 TEACC solution procedure flow chart (Hale, 1996)

Hale and O'Brien, 1998, 1994, modified the traditional application of boundary

conditions (Figure A - 4) to the SLCC to allow the TEACC simulation to be highly responsive

and capable of representing time-variant behavior. Figure 7 - 4a illustrates necessary

modifications for the TEACC application. To provide a convenient means of comparison,

Figure A - 4 is repeated here as Figure 7 - 4b. To assure TEACC simulation fidelity, the method

Inlet Boundary Conditions

P_T

T_T Curv

V_θ

Mass Flow = Constant

Flow

Exit Boundary Condition

Curv
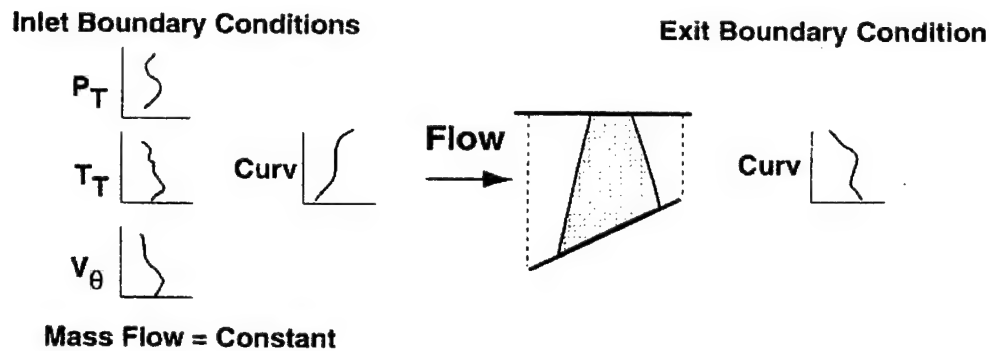
a. Modifications to SLCC for TEACC - boundaries just before and after blade row
(Hale and O'Brien, 1998)

**Inlet Boundary
Conditions**

P_T

T_T

V_θ

**Mass Flow = Constant
Curvature = 0**

Flow

Axial Computational Grid

**Exit Boundary
Condition**

Curvature = 0

Rotor Blade
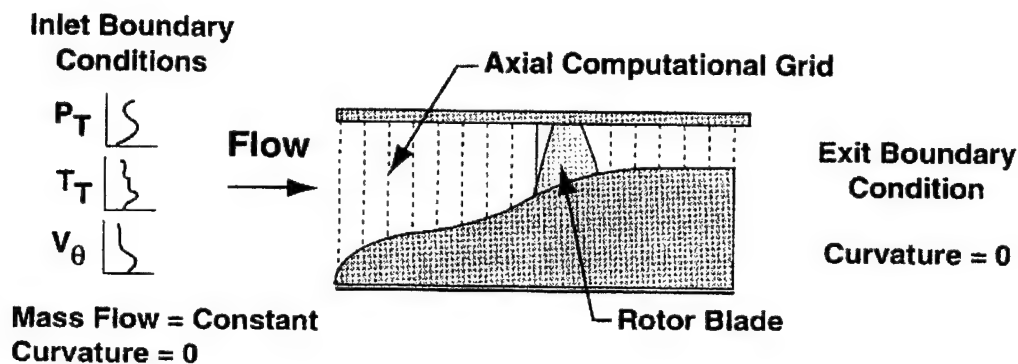
b. Traditional SLCC application - boundaries far upstream and downstream of blade row
(Hale and O'Brien, 1998)

Figure 7 - 4 Boundary condition specification for streamline curvature applications

was restricted to a small axial region on either side of a blade row; thus, specification of inlet and

exit flow curvature was required (Figure 7 - 4a). Within the TEACC, the time-dependent, 3-D

WIND flow solver determines all boundary conditions. More details on the modifications are

provided by Hale and O'Brien, 1998.

Source terms are calculated across each blade row using a control volume analysis after

the SLCC converges to a steady solution (at each time step). Essentially, with the SLC

approach, blade rows are represented as a series of radially segmented semi-actuator disks. The

SLCC solves for streamline locations (see Appendix A), which provide the basis for defining

126

control volumes. Axial, radial, and circumferential forces, and rate of shaft work are determined by applying integral conservation laws across each volume. These source terms must then be distributed throughout the overall 3-D (TEACC) grid structure (within a bladed region). The following paragraphs briefly describe the control volume definition, source term determination, and distribution. Details can be found in Hale, 1996.

The SLCC control volumes were constructed using a Cartesian right-handed coordinate system to be consistent with TEACC (Hale, 1996). As indicated in Figure 7 - 5, a streamline
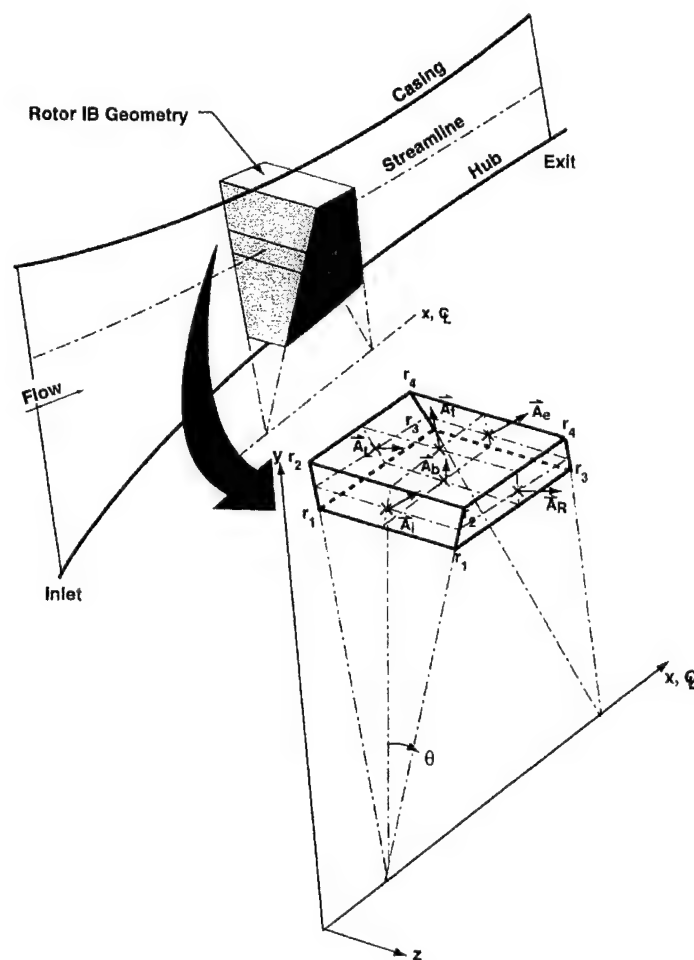
Figure 7 - 5 Cartesian control volumes defined by Rotor 1B's geometry and streamline solution (Hale, 1996)

127

passes through the center of each individual control volume. Blade geometry specifications (chord, leading and trailing edge lean and sweep) and the desired number of streamlines define each control volume, resulting in a collection of radial volumes, one above the other. To provide reasonable geometric fidelity, surface areas and volumes were determined using a circumferential segment of $\theta = 0.5$ degrees.

Steady-state control volume analysis provides the source terms. Since flow solutions are known only at streamline-axial station intersections (center axial face of each control volume), Hale, 1996, used the following assumptions:

- Top and bottom of control volume are streamsurfaces; thus, no mass, momentum, or energy transfer.

- Uniform properties across the primarily axial (inlet and exit) faces.

- Pressure on faces in the y-direction (top and bottom) calculated as an average of the four pressures on the inlet and exit faces of two adjacent radial volumes.

- Pressure on faces in the z-direction (left and right) calculated as an average of the inlet and exit face pressure of that volume.

- No net momentum contribution in the circumferential direction due to axisymmetric solution nature of the SLC approach.

With these assumptions, turbomachinery source terms can be calculated from the simplified integral momentum and energy control volume equations below:

$$x-momentum: \quad F_x = P_e A_{xe} - P_i A_{xi} + P_t A_{xt} - P_b A_{xb} + \dot{m}(V_{xe} - V_{xi}) \tag{7-2a}$$

$$y-momentum: \quad F_y = P_e A_{ye} - P_i A_{yi} + P_t A_{yt} - P_b A_{yb} + 2P_r A_{yr} + \dot{m}(V_{ye} - V_{yi}) \tag{7-2b}$$

$$z-momentum: \quad F_z = \dot{m}(V_{ze} - V_{zi}) \tag{7-2c}$$

$$energy: \quad \dot{W}_s = \dot{m}c_p(T_{te} - T_{ti}) \tag{7-3}$$

The $\dot{m}$ in Equations (7-2) and (7-3) is the local mass flow rate through each control volume.

The sources are divided by local volume and distributed throughout the TEACC computational domain (grid points within a bladed region). Radial distribution is readily accomplished via the nature of the streamline curvature approach (see Figure 7 - 6). The TEACC radial sources are obtained by using a spline interpolation technique on the SLCC source terms. Note that each circumferential segment – from hub to tip – could have a different radial distribution for the general, non-axisymmetric case.

Circumferential distribution of sources is inherent in the TEACC technique. At the entrance to a blade row, the SLCC is called for each circumferential segment defined by the TEACC grid. Further, as discussed in Appendix A, since the SLCC acquires its boundary conditions immediately upstream and downstream of each blade row, it is very sensitive to a time-varying flow field.

Since the SLCC is only applied at the entrance and exit of a blade row (and nowhere in between), the distribution of axial sources presented the greatest challenge. Hale, 1996, established a weighting function and examined a variety of linear distribution shapes, each time ensuring conservation. He observed that: (a) the overall solution did not change noticeably for a distribution function that allowed convergence, and (b) a uniform distribution was best for a stable, robust solution. Thus, a uniform distribution of axial sources has been adopted.

129

Streamline Curvature Solution
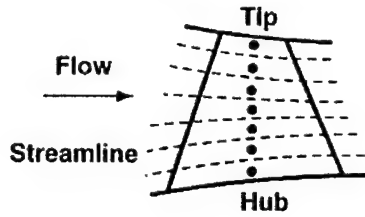
a. SLCC streamline grid system

b. SLCC volumetric distribution

TEACC Solution
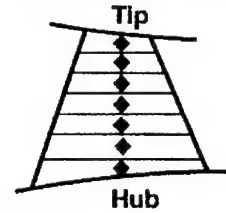
c. Source integration in 3D solver
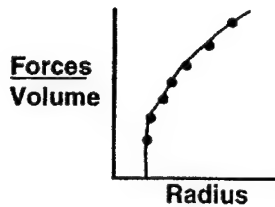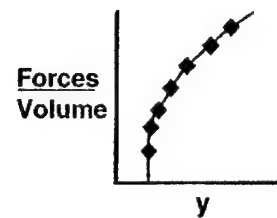
d. Interpolated volumetric distribution

Figure 7 - 6 Radial distribution of turbomachinery source terms defined at the centers of the SLCC control volumes and interpolated to the centers of TEACC's fixed grid control volumes

7.4 TEACC Assessment and Recommended Improvements

7.4.1 Assessment

As presented in Chapters 1 and 2, improved, physics-based analysis tools are needed to investigate complex, off-design compression system performance. The TEACC methodology described above offers promise for accurate investigation of flow phenomena within the limitations inherent in the approach. The accuracy of the method is largely dependent upon the source term estimation from the streamline curvature approximation, specifically, the loss and deviation correlations. This section provides an assessment of the overall TEACC approach, and recommends modifications based on the present work to improve simulation fidelity.

Table 7 - 1 Assessment of the TEACC overall approach

Strengths	Limitations
Full annulus representation - Investigation of complex engine-inlet integration issues, like inlet distortion	*Physics not fully represented* - Correlations not always physics-based - Uncertainty when applied to designs outside correlation database
Unsteady, 3-D formulation - Time-dependent analyses - "Potential-flow" interactions included	Wake and shock-boundary layer unsteadiness not included - Approximately 2-5% impact on efficiency (refer to Section 2.4)
Low-density grid (on order of 100,000 grid points for 3 stages) allows for "reasonable" run times for full-annulus, multistage compression systems, including upstream and downstream influences	Limits flow phenomena investigation to length scales on order of blade chord - Source terms from SLCC "artificially" distributed to enhance model robustness
Successful application to single- and multi-stage machines (Hale, 1999, 1998)	*Applications required radial specification (calibration) of loss, deviation, and blockage to match available data*

Table 7 - 1 provides an assessment of the TEACC. The two limitations in *italics* were focus areas of the present work. The SLCC changes presented in earlier chapters helped to (a) make the correlations more physics-based, (b) extend the application range of the correlations, and (c) reduce the required "calibration" and better explain it in physical terms.

7.4.2 Recommended Improvements

The following recommendations, if implemented, should enhance the fidelity of the TEACC flow field solutions:

- An improved SLCC is absolutely essential for more accurate flow field representation. Results from the present work show that the changes, most notably improvements in loss modeling, have indeed alleviated some of the concerns relative to the italicized issues in Table 7 - 1. As pointed out in earlier chapters, additional SLCC improvements are needed, especially in the representation of deviation and secondary flow effects. These will be

131

discussed in Chapter 9.

Recommendation: Implement the modified SLCC within the TEACC.

- The influence of annulus wall boundary layer (BL) development and interaction with blade row tip leakage flows must be included. As noted by Dunham, 1995, it is well known that the endwall regions of a compressor have a major influence on its performance. The sensitivity study performed in the present work clearly showed this influence through the parameters "blblkg," "tipblkg," and "tiploss" (refer to Table 5 - 2 and figures in Section 5.4). When executed "stand-alone," the SLCC makes some provision (while admittedly simplified) for including these effects (presented in Section 5.2 and Chapter 6). When run within the TEACC structure, effects from wall BL development and blockage from secondary flows are not included – an inviscid solver is used and no displacement thickness or any other provision is made. It is unlikely that the simple tip blockage approach used in the present work would provide the necessary fidelity or robustness. Like the general recommendation presented in Chapter 9 for the SLCC, the TEACC should implement a sophisticated approach to better capture the physics.

Recommendation: The flow solver (WIND) should approximate the flow field using a thin-layer, turbulent, viscous flux model. As presented by Bush, et al., 1998, WIND already includes the capability to solve the thin-layer Navier-Stokes (TLNS) equations. In keeping with the overall TEACC methodology, the model should be used in the radial direction only, and then evaluated. This would help keep the run times down while significantly increasing the simulation fidelity.

- Even if boundary layer and secondary flow models simpler than those recommended are used, additional grid packing in the endwall regions is likely to be required to account for

strong gradients in the source terms. Figure 7 - 7a, obtained from the present work, provides an excellent illustration of these gradients. The plot shows R1 tangential blade force distribution as predicted by the SLCC with the tip blockage model used throughout the present research (axes are shifted from earlier figures to be consistent with results shown in Figure 7 - 7b). Results are shown as tangential force per volume, consistent with how the source terms are supplied to the TEACC. Even with the simplified tip model, the general behavior of the tangential force distribution appears to be captured, evidenced by comparison with Figure 7 - 7b, from Gallimore, 1997. Note the very large gradients evident from about 88% span in Figure 7 - 7a and 80% span in Figure 7 - 7b.

Recommendation: The TEACC should incorporate additional grid packing in the endwall regions beyond that shown in Figure 7 - 2. This should help enhance numerical stability by distributing the strong source term gradients over more grid points.

a. SLCC-predicted tangential forces from R1 of CRF rig, 98.6% Nc, PE

b. Rotor tangential forces from Dring(1993), φ=0.45 (Gallimore, 1997)
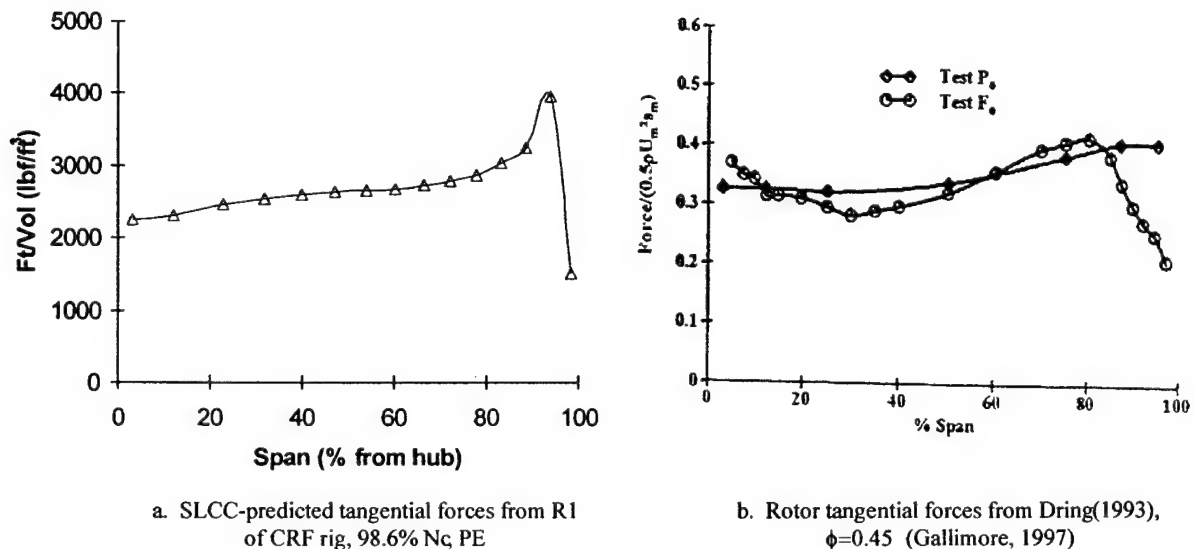
Figure 7 - 7 Comparison of radial distribution of tangential forces – SLCC and Gallimore, 1997

8. Summary and Conclusions

8.1 Summary

Despite the impressive advances made in CFD, specifically, modeling and solution of the steady and unsteady, Reynolds-averaged Navier-Stokes (RANS) equations, the turbomachinery community is still in need of reliable and robust off-design performance prediction. The present work was undertaken to examine and improve a streamline curvature method for use in off-design, system analysis of highly transonic fans typical of military fighter applications. The specific SLCC used here was chosen largely based on its use in a novel numerical approach – the Turbine Engine Analysis Compressor Code (TEACC). With the improved SLCC and additional recommendations presented in Chapter 7, the TEACC method offers the potential for accurate analysis of complex, engine-inlet integration issues (like those presented in Chapter 1).

The following summarizes the work presented in the preceding chapters:

- A review of the literature (Chapter 2) focused on recent advancements in the well-established streamline curvature modeling approach, as well as turbomachinery RANS approximations. While the SLC method is limited by loss, deviation, and blockage representation, the RANS approach has its own limitations, most notably in the mesh size required to resolve flow details (resulting in large computational requirements), and modeling issues associated with turbulence and transition. While fully 3-D, unsteady, RANS approximations offer the greatest potential for faithfully representing flow details at the smallest length scales, simpler approaches with physics-based models are needed to examine issues such as time-variant and inlet swirl distortion effects.

- The existing models/correlations used in the SLCC were assessed relative to key transonic flow field phenomena. The assessment provided the basis for model improvements

134

(Chapters 3 and 4), central to which was the incorporation of a physics-based shock loss model (summarized in Section 4.3). Shock loss is now estimated as a function of M_{1rel}, blade section loading (turning), solidity, leading edge radius, and suction surface profile. Other SLCC improvements were summarized in Section 3.5. These included incorporation of loading effects on the tip secondary loss model, use of radial blockage factors to model tip leakage effects, and an improved estimate of the blade section incidence at which minimum loss occurs.

- Data from a single-stage, isolated rotor (Rotor 1B) and a two-stage, advanced-design (low aspect ratio, high solidity) fan provided the basis for experimental comparisons. Rotor 1B was used exclusively to verify shock model improvements (Section 4.4). The application to the two-stage CRF fan further verified the SLCC improvements and provided the results presented in Chapter 6.

- A quantitative analysis regarding the sensitivity of overall fan performance – total pressure ratio, total temperature ratio, and adiabatic efficiency – on key model parameters was presented in Chapter 5.

- Results from a 3-D, steady, RANS model (for R1 only) were also used as a basis for comparing predicted performance from the SLCC (Chapter 6). The CFD results were valuable in providing flow properties that could not be determined from experimental data; i.e., radial distributions of static properties.

- The TEACC methodology was reviewed and assessed (Chapter 7). Proposed recommendations for improving simulation fidelity included incorporation of the modified SLCC, additional grid packing in the endwall regions, and using the thin-layer Navier-Stokes

135

equations in the radial direction to better approximate the effects of boundary layer/blade row interactions.

8.2 Conclusions

The fundamental goal of the present work was the development of an improved numerical approximation for understanding important flow phenomena in modern compression systems subjected to off-design operating conditions. Relative to this goal and the specific objectives listed in Section 1.3, the following conclusions are offered:

- The modifications to the SLCC have resulted in an improved approximation for representing compressor flow fields in highly transonic ($M_{1rel} > 1.4$) fans. The improved tool can be used for the design and/or analysis of high-performance, single-stage or multi-stage machines. Most significantly, incorporation of the shock model based upon the Bloch-Moeckel approach (Appendix B) has produced a unique numerical throughflow analysis tool in its thorough, physics-based treatment of shock losses. The implemented model accounts for local shock geometry changes (and hence, associated total pressure loss changes) with blade section operating condition, making it most suitable for off-design performance prediction.

- The importance of properly accounting for shock changes with operating conditions was clearly demonstrated. The majority of the increased total pressure loss with incidence across the R1 tip region was the result of increased shock loss, even at 85.0% Nc (Figure 6 - 25). A simple normal shock assumption, as is often used, produces a decreased shock loss prediction with incidence as a result of decreased Mach number (Table 6 - 1).

- In general, the effects of important flow phenomena relative to the off-design performance of the CRF fan were adequately captured (within the length scales imposed by the method), evidenced by the results presented in Chapter 6. Not including the wide-open discharge

(WOD) operating condition, discussed further below, the biggest discrepancy between model-predicted and data-determined performance was less than two points in overall efficiency (98.6% Nc, NS – Figure 6 - 1) and less than 2% in overall PR (85.0% Nc, PE, NOL+ - Figure 6 - 12). Thus, from the analysis presented in Section 5.4, the overall, mass-averaged, total pressure loss coefficient predicted by the improved method was *accurate to within +/-0.010 for all operating conditions (except WOD)*. The overall and spanwise comparisons demonstrated that the improved model gives reasonable performance trending and generally accurate results (accuracy comparable to that from a 3-D, steady, RANS solver). This indicates that the physical understanding of the blade effects and the flow physics that underlie the loss model improvements are realistic.

- Results from the parameter sensitivity study presented in Section 5.4 indicate that the level of accuracy of loss prediction should be *at least equal to* that of deviation (contrary to the first conclusion offered by Cetin, et al., 1987), most clearly seen in overall efficiency estimation, Figure 5 - 20. While deviation has a large influence on overall PR and of course, TR (Euler turbine equation), Figure 5 - 20 shows that it has a relatively small influence on efficiency prediction. This is because the PR and TR changes resulting from different estimates for deviation are largely in proportion to the ratio of $(PR^{\gamma-1/\gamma}-1)/(TR-1)$, the widely recognized formulation for determining adiabatic efficiency.

- The improved numerical approximation can be used to provide robust, timely, and accurate flow field solutions, noteworthy for exploring flow parameters not easily measured. For example, Small and O'Brien, 2001, used results from the modified SLCC, to derive digital filter characteristics needed for the prediction of blade row response to and propagation of total pressure inlet distortion. This new method relies on frequency domain transformations

137

and digital filter concepts to capture the effects of a blade row on distortion. Filter characteristics are related to fundamental flow phenomena.

Specifically, SLCC predictions for radial variation of axial velocity and elevated Mach number at the entrance of the rotor shock system were used. Figure 8 - 1 provides a convenient way to show the three additional speeds used to support the Small and O'Brien work. As indicated on the figure, the data for the three speeds were obtained with inlet total pressure distortion (produced by 3/rev or 8/rev screens). The 85.0% and 98.6% speedlines used in the present work are shown to provide a more complete picture for generalizing the results. As with all fan maps presented in this report, the speedlines were run from
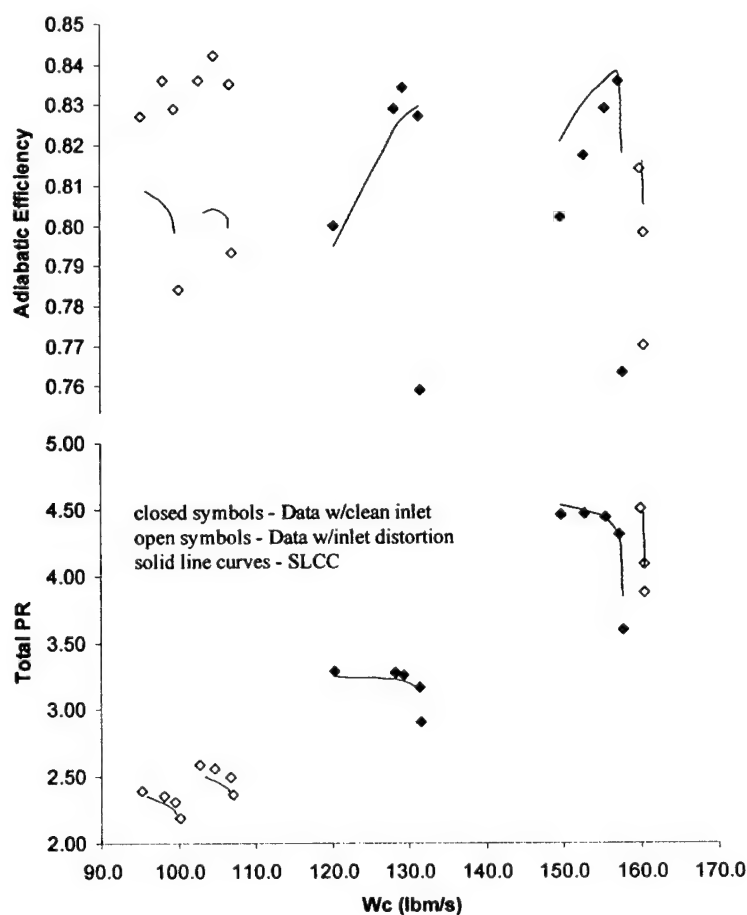
Figure 8 - 1 CRF fan map comparison of SLCC predictions and data

wide-open discharge to near-stall operating conditions. The same calibration process was used; namely, global additional deviation was adjusted until model, mass-averaged overall TR matched that determined from the data. Further, it should be noted that a transonic flow field was present even at the lowest speed (70.6% Nc).

- As noted by others and quantified relative to the present work (Section 5.4), accurate estimation of the blade section incidence at which minimum loss occurs, i_{min}, is a key factor for high fidelity performance prediction. It appears that the simple change implemented here (Equation 3-4) allowed for reasonable estimates of i_{min} based upon the faithful representation of overall machine peak efficiency operating conditions (see Figure 8 - 1). At all speeds except 70.6%, the peak efficiency was reasonably captured.

- The SLCC models and correlations represent the range of section incidence angles between *peak efficiency and stall* quite well (Figure 8 - 1). The incidence range between peak efficiency and choke is too large, evidenced by the WOD comparisons at the three high speeds shown in Figure 8 - 1. In all cases, the model overpredicts the performance. The loss bucket needs to be "squeezed" more between PE and WOD (Chapter 9 recommendations).

- While the simple improvement to the tip loss secondary model (Equation 3-3) and the use of rotor exit tip blockage factors better accounted for the physical behavior, a more sophisticated approach to secondary flow modeling is required. The importance of accurate representation of the tip regions relative to the hub regions was shown in the results from Section 5.4. Again, a recommendation is provided in the next chapter.

- Results appear to confirm the calibration process used throughout the present work. Inevitably, all numerical approximations require some level of calibration as a result of modeling limitations. To establish a reasonable level of confidence in the SLCC predicted

139

performance, certain "data" (either experimental or from another numerical approximation) are required to calibrate the model for a specific application. At a minimum, these data include overall, mass-averaged total temperature ratio at each speed of interest and a radial distribution of TR across each rotor row at the machine design point. Thus, the level of calibration (amount of information) needed to achieve reasonable performance estimates was significantly reduced, one of the key objectives of this research. Fundamentally, of course, the incorporation of physics-based models, as was done here, is the most desired solution. As a result of the loss model improvements, the calibration process assumed accurate total pressure loss estimation. Solution results and comparison to those obtained from data and CFD confirm the process. Further, the process produces robust solutions. As discussed in Section 6.3.2, despite misrepresenting the inlet velocity profile by possibly as much as 100 ft/s, flow solutions at the R1 exit were quite satisfactory, which is extremely important for setting up proper conditions for downstream blade rows in multistage applications.

9. Recommendations

Recommendations relative to results from the present research are provided in this chapter. In Section 7.4, suggestions specific to improving the TEACC, a logical extension of the present work, were provided. Additionally, the fact that the model faithfully represented *interstage* flow fields (as demonstrated in Chapter 6) allows for another potential extension. The approach could be used to provide boundary condition information for higher fidelity models (like unsteady, 3-D, RANS solvers) needed to explore phenomena of much smaller length scale – shock unsteadiness, unsteady pressure loadings, etc.

As noted throughout this report, additional work is required to further improve the SLCC. Physics-based models should be sought to further enhance the general applicability of the approach and reduce the calibration required for a specific application. In general, improved blade exit flow angle prediction (through deviation representation) and secondary loss modeling are two key areas needing attention. Specific recommendations are provided below:

- An improved method for estimating deviation angle is needed. Deviation prediction is especially difficult because it is such a *local* phenomenon. Hence, unlike losses, which are conveniently categorized and averaged, deviation prediction is not as amenable to an "increment" approach (like that used here by Hearsey, 1994, based largely on the NASA-SP-36 development). Thus, the technique should treat deviation as a whole, with maybe an increment of deviation due to secondary effects (like tip leakage flows). A good starting point would be the work of Cetin, et al., 1987. Other data sources incorporating modern blade designs are needed. The work reported by Law and Puterbaugh, 1988, is one potential source. Further, development of the correlation/model should also be based on results from RANS solvers which have been successfully applied to these geometries.

141

- An accounting for the effects of turning due to oblique shocks is needed. As a consequence of not including this turning, the deviation estimation resulted in negative total deviation angles at the R1 tip regions (last four streamlines, see Table 3 - 1). Although non-physical, this result was not surprising. The model was in essence compensating for the "lost turning." A potential solution is an "effective" camber approach. The concept uses a portion of the flow turning calculated from oblique shock theory to determine an "effective" blade section camber that is used in applicable SLCC models and correlations. The improved shock model is quite amenable to this approach. A simple application was implemented to demonstrate the idea. Figure 9 - 1a was obtained using 50% of the flow turning predicted from oblique shock theory. The result, provided in Figure 9 - 1b, was encouraging. The deviation predictions are much more realistic, most notably in the tip region of R1. While the calculation of flow turning from oblique shock theory is straightforward, the determination of "effective" turning is quite complex (due to blockage, shock-boundary layer interaction, potential for downstream normal shock, unsteadiness, etc.). Indeed, pursuit of this recommendation should focus on a physical-based (ideally, physics-based) representation.

- A more fundamental approach for including the effects of spanwise mixing, secondary flows, and annulus wall boundary layer should be implemented. As noted several times in this report, the treatment of these by the present method is overly simplified. The approaches of Dunham, 1995, 1996, and Gallimore, 1997, should be reviewed and assessed for use in the present application. While some problems occurred when applied to high-speed compressors (boundary layer predicted too thick), Dunham's work produced an *analytically based* endwall model using both annulus wall boundary layer theory (including blade defect forces) and secondary flow theory. Gallimore's work focused on the development of a novel

a. Spanwise camber/effective camber distribution   b. Spanwise deviation distribution
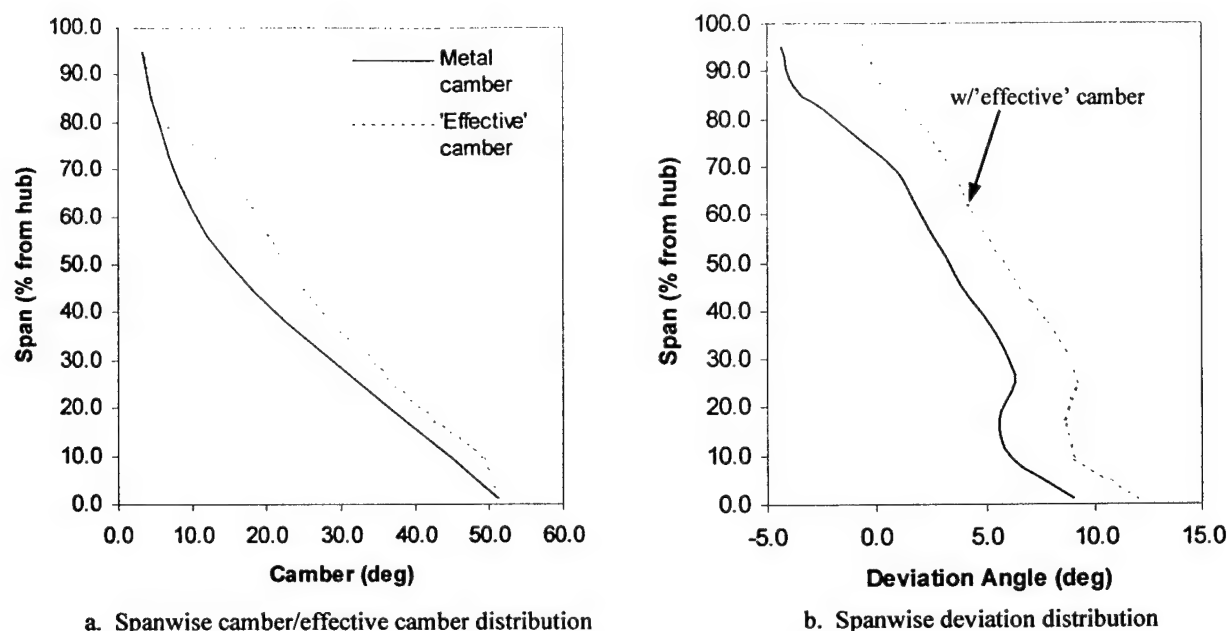
Figure 9 - 1 Demonstration of "effective" camber concept – R1, PE condition

approach using tangential blade forces in the endwall regions of his "viscous throughflow" model. While somewhat more empirical than Dunham, Gallimore's model showed very good agreement with both data and RANS predictions for low-speed and high-speed compressors.

- The model's representation of the incidence range between peak efficiency and choke needs improving. Specifically, the correlation used to estimate the choking incidence is not applicable to high-speed designs, resulting in an incidence range that is too large (as noted in the previous chapter). By examining the results shown by Cetin, et al., 1987 (eight different DCA and MCA transonic designs) and Law and Puterbaugh, 1988 (single design incorporating CDA and precompression airfoil with $M_{1rel} = 1.60$), the following simple correlation was developed:

143

$$i_{choke} - i_{min} = 2.5M_{elev} - 5.0 \text{ (deg)} \tag{9-1}$$

A quick check revealed that Equation (9 – 1) would indeed reduce the incidence range between peak efficiency and choke. Thus, Equation (9 – 1) should be implemented within the present model as a reasonable initial starting point for improving the choking incidence prediction.

- The approximation used to predict the increment of detached bow shock loss with incidence angle (Equation 4-9) needs further assessment. It was developed and implemented based on limited information. Given that this loss can become quite significant at high blade section loadings, it seems reasonable to explore the development of a more fundamentally based relation. The work of Bloch, 1996, should be the starting point; however, results from RANS solvers probably are the key to any significant improvement in this area.

- The SLCC should be modified to provide for the specification of blade lean and sweep as functions of radius. As noted in Section 5.2, currently, the code only allows input of a single value at each axial location. Modern fan designs incorporate significant radial variations in sweep and lean angles. These should be represented faithfully to ensure that: (a) the correct incidence angles to the blade rows are established, and (b) accurate control volume geometries are calculated for source term determination in the TEACC application.

Bibliography

Adamczyk, J.J., "Numerical Simulation of Multi-Stage Turbomachinery Flows," Design Principles and Methods for Aircraft Gas Turbine Engines, RTO-MP-8, March 1999, pp. 21-1–21-25.

Adamczyk, J.J., Celestina, M.L. and Greitzer, E.M., "The Role of Tip Clearance in High-Speed Fan Stall," ASME Paper No. 91-GT-83, International Gas Turbine and Aeroengine Congress and Exposition, Orlando, FL, June 3-6, 1991.

AFRL-PR-WP-TM-1998-2148, *High Cycle Fatigue (HCF) Science and Technology Program 1998 Annual Report*, prepared by Universal Technology Corporation, Dayton, OH, January 1999.

AGARD-AR-355, *CFD Validation for Propulsion System Components*, edited by Dunham, J., May 1998.

AGARD-CP-571, *Loss Mechanisms and Unsteady Flows in Turbomachines*, January 1996.

Billet, G., Huard, J., Chevalier, P. and Laval, P., "Experimental and Numerical Study of the Response of an Axial Compressor to Distorted Inlet Flow," *Transactions of the ASME, Journal of Fluids Engineering*, Vol. 110, December 1988, pp. 355-360.

Bloch, G. S., "Flow Losses in Supersonic Compressor Cascades," Ph.D. Dissertation, Mechanical Engineering Dept., Virginia Polytechnic Institute and State University, Blacksburg, VA, July 1996.

Bloch, G. S., Copenhaver, W. W. and O'Brien, W. F., "A Shock Loss Model for Supersonic Compressor Cascades," *Transactions of the ASME, Journal of Turbomachinery*, Vol. 121, January 1999, pp. 28-35.

Bloch, G. S., Copenhaver, W. W. and O'Brien, W. F., "Development of an Off-Design Loss Model for Transonic Compressor Design," AGARD-CP-571, January 1996, pp. 16-1–16-14.

Boller, S. and O'Brien, W.F., "One Dimensional Dynamic Wake Response in an Isolated Rotor Due to Inlet Pressure Distortion," AIAA Paper No. 99-2676, 35th AIAA/ASME/SAE/ASEE Joint Propulsion Conference and Exhibit, Los Angeles, CA, June 20-24, 1999.

Bush, R.H., Power, G.D. and Towne, C.E., "WIND: The Production Flow Solver of the NPARC Alliance," AIAA-98-0935, 36th Aerospace Sciences Meeting & Exhibit, Reno, NV, January 12 – 15, 1998.

Casey, M.V., "Computational Methods for Preliminary Design and Geometry Definition in Turbomachinery," AGARD-LS-195, *Turbomachinery Design Using CFD*, May 1994.

Çetin, M., Üçer, A. Ş., Hirsch, CH. And Serovy, G. K., *Application of Modified Loss and Deviation Correlations to Transonic Axial Compressors*, AGARD-R-745, 1987.

Copenhaver, W.W., Hah, C. and Puterbaugh, S.L., "Three-Dimensional Flow Phenomena in a Transonic, High-Throughflow, Axial-Flow Compressor Stage," *Transactions of the ASME, Journal of Turbomachinery*, Vol. 115, April 1993, pp. 240-248.

Cousins, W.T. and O'Brien, W.F., "Axial-Flow Compressor Stage Post-Stall Analysis," AIAA Paper No. 85-1349, 1985.

Creveling, H.F. and Carmody, "Axial-Flow Compressor Computer Program for Calculating Off-Design Performance," NASA-CR-72472, 1968.

Cumpsty, N.F., Compressor Aerodynamics, Department of Engineering, University of Cambridge, Longman Scientific & Technical, Longman Group UK, Limited Essex CM20 2JE, England, co-published in the United States with John Wiley & Sons, Inc., 605 Third Avenue, New York, NY, 1989.

Davis, M.W., Jr., Hale, A.A. and Beale, D., "An Argument for Enhancement of the Current Inlet Distortion Ground Test Practice for Aircraft Gas Turbine Engines," ASME 2001-GT-0507, to be presented at the ASME Turbo Expo 2001, New Orleans, LA, June 2001.

Davis, M.W., Jr. and O'Brien, W.F., "Stage-by-Stage Post-Stall Compression System Modeling Technique," AIAA *Journal of Propulsion and Power*, Vol. 7, No. 6, November-December 1991, pp. 997-1005.

Denton, J.D., "Loss Mechanisms in Turbomachines," The 1993 IGTI Scholar Lecture, *Transactions of the ASME, Journal of Turbomachinery*, Vol. 115, October 1993, pp. 621-656.

Denton, J. D. and Dawes, W. N., "Computational fluid dynamics for turbomachinery design," *Proceedings of the Institution of Mechanical Engineers, Journal of Mechanical Engineering Science, Part C*, Vol. 213, No. C2, 1999.

Dorney, D. J. and Sharma, O. P., "Evaluation of Flow Field Approximations for Transonic Compressor Stages," *Transactions of the ASME, Journal of Turbomachinery*, Vol. 119, July 1997, pp. 445-451.

Dunham, J., "Aerodynamic losses in turbomachines," AGARD-CP-571, Keynote address, pp. K-1 – K-13, January 1996.

Dunham, J., "Compressor Off-Design Performance Prediction Using an Endwall Model," ASME Paper No. 96-GT-62, presented at the International Gas Turbine and Aeroengine Congress & Exhibition, Birmingham, UK – June 10-13, 1996.

Dunham, J., "A New Endwall Model for Axial Compressor Throughflow Calculations," *Transactions of the ASME, Journal of Turbomachinery*, Vol. 117, October 1995, pp. 533-540.

Fan, S. and Lakshminarayana, B., "Computation and Simulation of Wake-Generated Unsteady Pressure and Boundary Layers in Cascades," ASME Papers 94-GT-140 and 94-GT-141, 1994.

Freeman, C. and Cumpsty, N.A., "A Method for the Prediction of Supersonic Compressor Blade Performance," ASME Paper No. 89-GT-326, 1989.

Gallimore, S.J., "Viscous Throughflow Modeling of Axial Compressor Bladerows using a Tangential Blade Force Hypothesis," ASME Paper No. 97-GT-415, presented at the International Gas Turbine and Aeroengine Congress & Exhibition, Orlando, FL – June 2-5, 1997.

Goldstein, S., edited by, Modern Developments in Fluid Dynamics An Account of Theory and Experiment Relating to Boundary Layers, Turbulent Motion and Wakes, Volume II, Dover Publications, Inc., 1965.

Hah, C., "Calculation of Three-Dimensional Viscous Flows in Turbomachinery with an Implicit Relaxation Method," *Journal of Propulsion*, AIAA, Vol. 3, No. 5, Sep - Oct 1987, pp. 415-422.

Hah, C., Rabe, D. C., Sullivan, T. J. and Wadia, A. R., "Effects of Inlet Distortion on the Flow Field in a Transonic Compressor Rotor," *Transactions of the ASME, Journal of Turbomachinery*, Vol. 120, April 1998, pp. 233-246.

Hah, C. and Wennerstrom, A. J., "Three-Dimensional Flowfields Inside a Transonic Compressor With Swept Blades," *Transactions of the ASME, Journal of Turbomachinery*, Vol. 113, April 1991, pp. 241-251.

Hale, A. A., "A 3D Turbine Engine Analysis Compressor Code (TEACC) for Steady-State Inlet Distortion," Ph.D. Dissertation, Mechanical Engineering Dept., Virginia Polytechnic Institute and State University, Blacksburg, VA, December 1996.

Hale, A., Chalk, J., Klepper, J. and Kneile, K., "Turbine Engine Analysis Compressor Code: TEACC – Part II: Multi-Stage Compressors and Inlet Distortion," AIAA-99-3214, 17th AIAA Applied Aerodynamics Conference, Norfolk, VA, June 28 – July 1, 1999.

Hale, A.A., Davis, M.W., Jr., and Kneile, K.R., "Turbine Engine Analysis Compressor Code: TEACC – Part I: Technical Approach and Steady Results," AIAA-94-0148, 32nd Aerospace Sciences Meeting, Reno, NV, January 1994.

Hale, A. and O'Brien, W., "A Three-Dimensional Turbine Engine Analysis Compressor Code (TEACC) for Steady-State Inlet Distortion," *Transactions of the ASME, Journal of Turbomachinery*, Vol. 120, July 1998, pp. 422-430.

Hearsey, R. M., "Program HT0300 NASA 1994 Version," Doc. No. D6-81569TN, Volumes 1 and 2, The Boeing Company, 1994.

Hill, P. and Peterson, C., Mechanics and Thermodynamics of Propulsion, 2nd ed., Addison-Wesley Publishing Co., Inc., 1992, pp. 275-355.

Howard, J.S., III, "Improved Methods for Modeling Dynamic Stage Characteristics," MS Thesis, Mechanical Engineering Dept., Virginia Polytechnic Institute and State University, Blacksburg, VA, April 1999.

Howard, M.A. and Gallimore, S.J., "Viscous Throughflow Modeling for Multistage Compressor Design," *Transactions of the ASME, Journal of Turbomachinery*, Vol. 115, April 1993, pp. 296-304.

Horlock, J.H., Axial Flow Compressors, Fluid Mechanics and Thermodynamics, Robert E. Krieger Publishing Co., 1982, p. 115.

Jennions, I.K., "Elements of a Modern Turbomachinery Design System," AGARD-LS-195, *Turbomachinery Design Using CFD*, May 1994, pp. 2-1 – 2-22.

John, J.E.A., Gas Dynamics, 2nd ed., Allyn and Bacon, Inc., 1984.

iSIGHT™ Guides, Engineous Software, Inc., Document Version 1.0, November 1998.

Kays, W.M. and Crawford, M.E., Convective Heat and Mass Transfer, 2nd ed., McGraw-Hill Book Company, 1980.

Klepper, J., "Technique to Predict Stage-By-Stage, Pre-Stall Compressor Performance Characteristics Using a Streamline Curvature Code With Loss and Deviation Correlations," MS Thesis, University of Tennessee, Knoxville, TN, August 1998.

Koch, C.C., "Technical Evaluation Report," *Loss Mechanisms and Unsteady Flows in Turbomachines*, AGARD-CP-571, January 1996, pp. T-1–T-6.

Koch, C.C. and Smith, L.H., Jr., "Loss Sources and Magnitudes in Axial-Flow Compressors," *Transactions of the ASME, Journal of Engineering for Power*, July 1976, pp. 411-424.

König, W. M., Hennecke, D. K. and Fottner, L., "Improved Blade Profile Loss and Deviation Angel Models for Advanced Transonic Compressor Bladings: Part I—A Model for Subsonic Flow," *Transactions of the ASME, Journal of Turbomachinery*, Vol. 117, January 1996, pp. 73-80.

König, W. M., Hennecke, D. K. and Fottner, L., "Improved Blade Profile Loss and Deviation Angel Models for Advanced Transonic Compressor Bladings: Part II—A Model for Supersonic Flow," *Transactions of the ASME, Journal of Turbomachinery*, Vol. 117, January 1996, pp. 81-87.

Lakshminarayana, B., Sitaram, N. and Zhang, J., "End-Wall and Profile Losses in a Low-Speed Axial Flow Compressor Rotor," ASME Paper No. 85-GT-174, 1985.

Law, C.H. and Puterbaugh, S.L., "Parametric Blade Study Test Report Rotor Configuration No. 4," AFWAL-TR-88-2110, Wright-Patterson AFB, OH, November 1988.

LeJambre, C.R., Zacharias, R.M., Biederman, B.P., Gleixner, A.J. and Yetka, C.J., "Development and Application of a Multistage Navier-Stokes Solver: Part II— Application to a High-Pressure Compressor Design," *Transactions of the ASME, Journal of Turbomachinery*, Vol. 120, April 1998, pp. 215-223.

Liepmann, H.W. and Roshko, A., Elements of GasDynamics, Galcit Aeronautical Series, John Wiley & Sons, Inc., Eighth printing, May 1967.

Longley, J.P. and Greitzer, E.M., "Inlet Distortion Effects in Aircraft Propulsion System Integration," AGARD-LS-183, *Steady and Transient Performance Prediction of Gas Turbine Engines*, May 1992, pp. 7-1 – 7-19.

Manwaring, S. R., Rabe, D. C., Lorence, C. B. and Wadia, A. R., "Inlet Distortion Generated Forced Response of a Low-Aspect-Ratio Transonic Fan," *Transactions of the ASME, Journal of Turbomachinery*, Vol. 119, October 1997, pp. 665-676.

Mazzawy, R.S., and Banks, G.A., "Circumferential Distortion Modeling of the TF30-P-3 Compression System," NASA-CR-135124, January 1977.

Mazzawy, R.S., and Banks, G.A., "Modeling and Analysis of the TF30-P-3 Compressor System with Inlet Pressure Distortion," NASA-CR-134996, April 1976.

Metais, O., "Direct and Large-Eddy Simulations of Coherent Vortices in Three-Dimensional Turbulence: Geophysical and Industrial Applications," Eddy Structure ID, edited by J.P. Bonnet, Springer-Verlag, NY, 1996, pp. 333-364.

Mikolajczak, A.A. and Pfeffer, A.M., "Methods to Increase Engine Stability and Tolerance to Distortion," AGARD-LS-72, Section 7, 1974.

Miller, G. R., Lewis, G. W., Jr. and Hartmann, M. J., "Shock Losses in Transonic Compressor Blade Rows," *Transactions of the ASME, Journal of Engineering for Power*, July 1961, pp. 235-242.

Moeckel, W.E., "Approximate Method for Predicting Form and Location of Detached Shock Waves Ahead of Plane or Axially Symmetric Bodies," NACA TN 1921, 1949.

NASA SP-36, *Aerodynamic Design of Axial-Flow Compressors*, edited by Johnsen, I.A. and Bullock, R.O., 1965.

Ng, W.F. and Epstein, A.H., "Unsteady Losses in Transonic Compressors," *Transactions of the ASME, Journal of Engineering for Gas Turbines and Power*, Vol. 107, April 1985, pp. 345-353.

Novack, R.A., "Streamline Curvature Computing Procedures for Fluid-Flow Problems," *Transactions of the ASME, Journal of Engineering for Power*, October 1967, pp. 478-490.

Novack, R.A. and Hearsey, R.M., "A Nearly Three-Dimensional Intrablade Computing System for Turbomachinery," *ASME Journal of Fluids Engineering*, Vol. 99, 1977, pp. 154-166.

Parker, D.E. and Simonson, M.R., "Transonic Fan/Compressor Rotor Design Study," Vol. V, AFWAL-TR-82-2017, Wright-Patterson AFB, OH, February 1982.

Rabe, D.C., "Shock Wave End Wall Boundary Layer Interaction in a Transonic Compressor Rotor," Ph.D. Dissertation, Mechanical Engineering Dept., Virginia Polytechnic Institute and State University, Blacksburg, VA, May 1987.

Rabe, D., Bolcs, A. and Russler, P., "Influence of Inlet Distortion on Transonic Compressor Blade Loading," AIAA Paper No. 95-2461, 31st AIAA/ASME/SAE/ASEE Joint Propulsion Conference, San Diego, CA, 1995.

Rabe, D.C., Wennerstrom, A.J. and O'Brien, W.F., Jr., "Characterization of Shock Wave End Wall Boundary Layer Interactions in a Transonic Compressor Rotor," ASME 87-GT-166 (paper accepted for publication in the *Transactions of the ASME*, 1987.

Rabe, D.C., Williams, C. and Hah, C., "Inlet Flow Distortion and Unsteady Blade Response in a Transonic Axial-Compressor Rotor," ISABE Paper No. 99-7287, 1999.

Reid, C., "The Response of Axial Flow Compressors to Intake Flow Distortion," ASME Paper No. 69-GT-29, 1969.

Rhie, C.M., Gleixner, A.J., Spear, D.A., Fischberg, C.J. and Zacharias, R.M., "Development and Application of a Multistage Navier-Stokes Solver: Part I—Multistage Modeling Using Bodyforces and Deterministic Stresses," *Transactions of the ASME, Journal of Turbomachinery*, Vol. 120, April 1998, pp. 205-214.

SAE S-16 Committee, AIR 1419, "Inlet Total Pressure Distortion Considerations for Gas Turbine Engines," Society of Automotive Engineers, May 1983.

SAE S-16 Committee, ARD50015, "A Current Assessment of the Inlet/Engine Temperature Distortion Problem," Society of Automotive Engineers, January 1991.

SAE S-16 Committee, ARD50026, "A Current Assessment of Planar Waves," Society of Automotive Engineers, September 1995.

SAE S-16 Committee, ARDxxxxx, "Intake Flow Angularity: A Current Assessment of the Inlet/Engine Swirl Distortion Problem," Society of Automotive Engineers, DRAFT, August 1999.

SAE S-16 Committee, ARP 1420, "Gas Turbine Engine Inlet Flow Distortion Guidelines," Society of Automotive Engineers, March 1978.

Schwartz, J.R., "An Experimental and Analytical Investigation of Dynamic Flow Response of a Fan Rotor with Distorted Inlet Flow," MS Thesis, Mechanical Engineering Dept., Virginia Polytechnic Institute and State University, Blacksburg, VA, August 1999.

Sexton, M.R. and O'Brien, W.F.,Jr., "A Model for Dynamic Loss Response in Axial-Flow Compressors," ASME Paper No. 81-GT-154, 1981.

Seyler, D.R. and Gestolow, J.P., "Single Stage Experimental Evaluation of High Mach Number Compressor Rotor Blading Part 2 – Performance of Rotor 1B," NASA-CR-54582, September 1967.

Shah, R.K., "A Correlation for Laminar Hydrodynamic Entry Length Solutions for Circular and Noncircular Ducts," *Transactions of the ASME, Journal of Fluids Engineering*, Vol. 100, June 1978, pp. 177-179.

Simpson, R.L., Course notes for AOE 6154, "Turbulent Shear Flow," Virginia Polytechnic Institute and State University, Blacksburg, VA, Spring 2000.

Small, M.D., O'Brien, W.F. and Rabe, D.C., "A Digital Filter Method to Predict the Propagation of Total Pressure Distortion Through Blade Rows," presented at the 6th National HCF Conference, Jacksonville, FL, March 3-6, 2001.

Steenken, W.G., personal correspondence, February 2000.

Tennekes, H. and Lumley, J.L., A First Course in Turbulence, The MIT Press, Seventeeth printing, 1999, Cambridge, MA, 1972.

Thompson, D.W., King, P.I. and Rabe, D.C., "Experimental Investigation of Stepped Tip Gap Effects on the Performance of a Transonic Axial-Flow Compressor Rotor," *Transactions of the ASME, Journal of Turbomachinery*, Vol. 120, July 1998, pp. 477-486.

Tweedt, D.L., Schreiber, H.A. and Starken, H., "Experimental Investigation of the Performance of a Supersonic Compressor Cascade," *Transactions of the ASME, Journal of Turbomachinery*, Vol. 110, October 1988, pp. 456-466.

VKI LS 1996-05, *Unsteady Flows in Turbomachines*, von Karman Institute for Fluid Dynamics, March 11-15, 1996.

Weingold, H.D., Neubert, R.J., Behlke, R.F. and Potter, G.E. "Reduction of Compressor Stator Endwall Losses Through the Use of Bowed Stators," ASME Paper No. 95-GT-380, June 1995.

White, F.M., <u>Viscous Fluid Flow</u>, 2nd ed., McGraw-Hill, Inc., 1991.

Wisler, D.C., "Advanced Compressor and Fan Systems," lecture notes from UTSI short course *Aeropropulsion*, Dayton, OH, December 7-11, 1987.

Wu, C.H., "A General Through-Flow Theory of Fluid Flow with Subsonic or Supersonic Velocity in Turbomachines of Arbitrary Hub and Casing Shapes," NACA TN 2302, 1951.

Appendix A. Streamline Curvature Approach

An existing streamline curvature (SLC) technique was modified and used in the present work. The SLC approach to turbomachinery on an S2 surface (i.e., in the meridional plane) resolves streamline locations through iterative solution of radial equilibrium and continuity and correlations needed to represent blade effects. The SLC technique based on the general theory proposed by Wu, 1951, is well documented (see for example, Novack, 1967; Novack and Hearsey, 1977) and still in wide use today (Dunham, keynote address, AGARD-CP-571, 1996; Denton and Dawes, 1999). Cumpsty, 1989, provides an entire chapter (Chapter 3) on throughflow calculations, focusing on the SLC method. The governing equations and required closure relations of the *general* SLC method are briefly presented. The correlations used in the *specific* SLC approach chosen for the present work (Hearsey, 1994) are described in more detail.

A1.1 Streamline Curvature Approach

Assumptions involved in application of the basic SLC method are steady, adiabatic, axisymmetric, inviscid flow, with negligible body forces. The resulting governing equations are the well-known Euler equations, provided below in cylindrical coordinates:

$$\text{Continuity:} \qquad \frac{\partial(\rho r \lambda V_r)}{\partial r} + \frac{\partial(\rho r \lambda V_z)}{\partial z} = 0 \qquad\qquad (A-1)$$

$$\text{Axial Momentum:} \qquad V_r \frac{\partial V_z}{\partial r} + V_z \frac{\partial V_z}{\partial z} = -\frac{1}{\rho}\frac{\partial p}{\partial z} \qquad\qquad (A-2)$$

$$\text{Radial Momentum:} \qquad V_r \frac{\partial V_r}{\partial r} + V_z \frac{\partial V_r}{\partial z} - \frac{V_\theta^2}{r} = -\frac{1}{\rho}\frac{\partial p}{\partial r} \qquad\qquad (A-3)$$

$$\text{Circumferential Momentum:} \qquad V_r \frac{\partial V_\theta}{\partial r} + V_z \frac{\partial V_\theta}{\partial z} + \frac{V_r V_\theta}{r} = 0 \qquad\qquad (A-4)$$
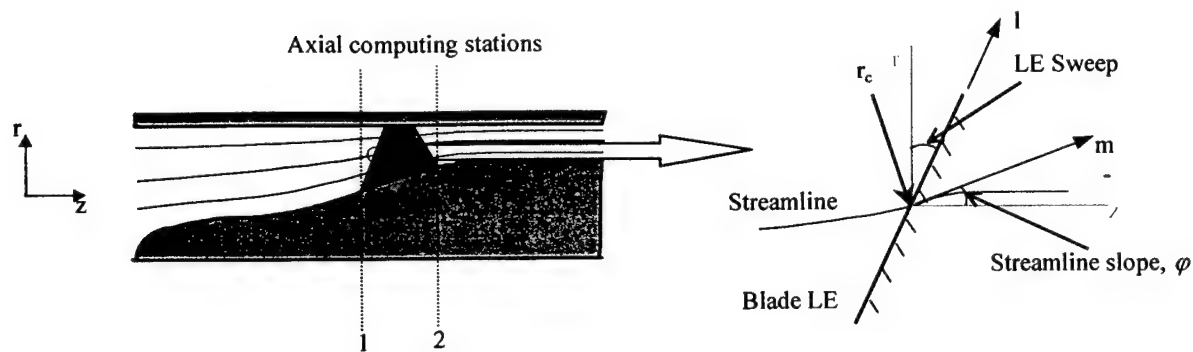
Figure A - 1 Meridional projection of streamline curvature computing station

Through algebraic manipulation, the momentum equations can be rearranged to include the vorticity components ($\bar{\nabla} \times \bar{V}$), combined with the thermodynamic equation of state, and mapped into a meridional projection of the flow field. Figure A - 1 shows the *m*-direction, defined by the projection of any streamline in the r-z plane. Changes in entropy and enthalpy must be specified, directly (for design) or indirectly through models/correlations within the code (for analysis), to represent the *external* effects of turbomachinery blade rows. Note that this does not violate the Euler equations, developed with the basic assumption that no mechanism *internal* to the fluid causes changes to the entropy and enthalpy. As a consequence of the assumptions and mapping into the meridional plane, the following first-order, nonlinear, governing equation is provided (Novak, 1967):

$$\frac{\partial \left(V_m^2\right)}{\partial r} + f_1(r)V_m^2 = f_2(r) \qquad (A - 5)$$

where:

$$f_1(r) = 2\sin^2\beta\left[\frac{-\sin\varphi}{V_m}\frac{\partial V_m}{\partial m} + \frac{\cos\varphi}{r_c} + \frac{\csc^2\beta}{2}\left(\frac{1}{Q}\frac{\partial Q}{\partial r}\right) + \frac{1}{2}\frac{\partial(\cot^2\beta)}{\partial r} + \frac{\cot^2\beta}{r} + \frac{2\omega}{V_m}\cot\beta\right]$$

$$f_2(r) = 2\sin^2\beta\left[\frac{1}{Q}\frac{\partial(IQ)}{\partial r} + \frac{(r\omega)^2}{2}\left(\frac{1}{Q}\frac{\partial Q}{\partial r}\right)\right]$$

and :

$$Q \equiv e^{\frac{-\Delta s}{c_p}} = \frac{\left(\frac{P_t}{P_i}\right)^{\frac{\gamma-1}{\gamma}}}{\frac{T_t}{T_i}} \qquad (i = upstream\ reference\ station)$$

$$I = relative\ stagnation\ enthalpy\ (rothalpy) = H - r\omega V_\theta$$

Across each blade row, three closure relations must be specified for each streamline to account for changes in angular momentum, enthalpy, and entropy. The closure relations take the form provided below. From velocity triangles and deviation correlations, the absolute tangential velocity at the blade row exit can be specified:

$$V_{\theta 2} = V_{m2}\tan\beta_2\cos\phi_2 + U_2 \tag{A-6}$$

The exit absolute total temperature is determined by using the Euler turbine and ideal gas thermodynamic relations:

$$T_{t2} = T_{t1} + \frac{U_2}{c_p}\left(V_{\theta 2} - \frac{r_1}{r_2}V_{\theta 1}\right) \tag{A-7}$$

From compressible and isentropic flow relations, definition of the relative total pressure loss coefficient, and constant rothalpy, the exit absolute total pressure can be determined from:

$$P_{t2} = P_{t1}\left(\frac{T_{t2}}{T_{t1}}\right)^{\frac{\gamma}{\gamma-1}}\left\{1 - \left(\frac{P_{t1,rel}}{P_{t2,rel}}\right)_{ideal} \varpi \left[1 - \left(\frac{1}{1+\frac{\gamma-1}{\gamma}M_{1,rel}^2}\right)^{\frac{\gamma}{\gamma-1}}\right]\right\} \qquad (A-8)$$
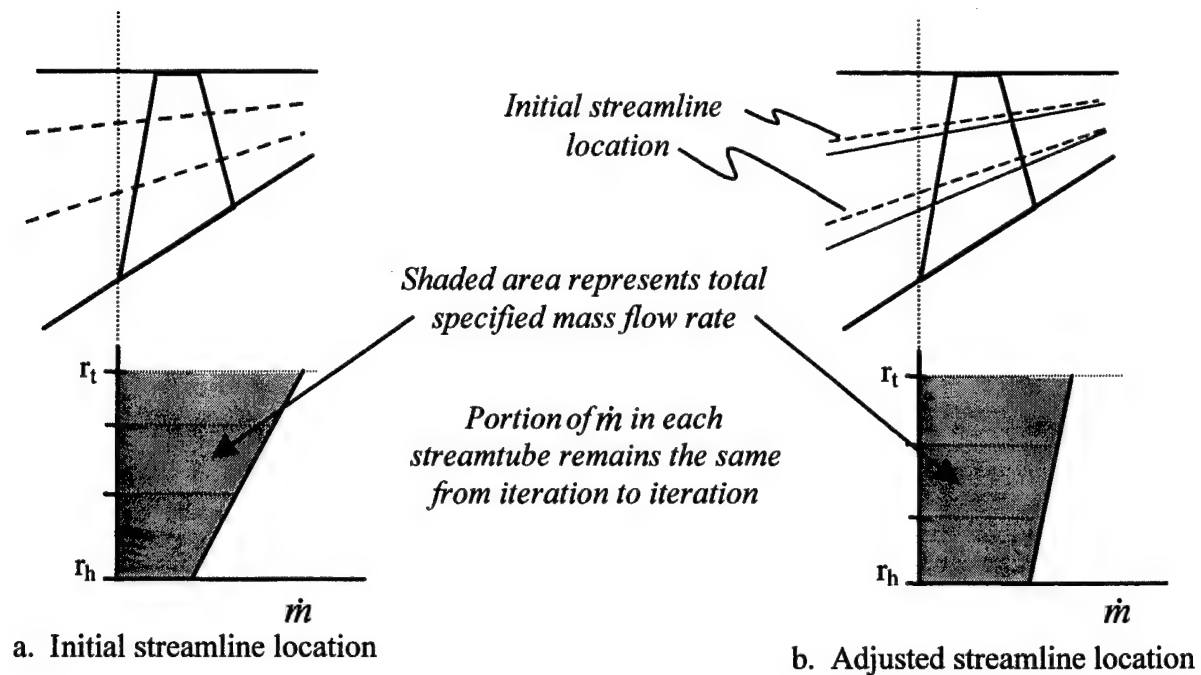
where:

$$\varpi \equiv \frac{\left(P_{t2,ideal} - P_{t2}\right)_{rel}}{P_{t1,rel} - P_1}$$

$$\left(\frac{P_{t1,rel}}{P_{t2,rel}}\right)_{ideal} = \left\{1 + \frac{\gamma-1}{2}M_{1,tan}^2\left[\left(\frac{r_2}{r_1}\right)^2 - 1\right]\right\}$$

$$and \qquad M_{1,tan}^2 \equiv \frac{U_1^2}{\gamma R T_{t1,rel}}$$

With closure obtained, solution of the governing equations via the streamline curvature method proceeds as illustrated in Figure A - 2 and Figure A - 3. At the inlet boundary condition (BC) plane, streamline locations are selected with equal annulus area between them (in the present method) based on the specified number of streamlines and actual annulus geometry. The specification of overall mass flow rate and total pressure and temperature at the inlet BC allows for calculation of streamline slope, φ, and radius of curvature, r_c. The blade row exit absolute meridional velocity, V_{m2}, is computed from current conditions and iterated upon radially (inner loop of Figure A - 3) until the overall calculated mass flow rate equals that specified. Streamlines are then adjusted radially (Figure A - 2b) so that each streamtube contains the portion of mass flow originally calculated. The process is repeated until V_m, φ, and r_c changes are within a desired tolerance (outer loop of Figure A - 3).

Initial streamline location

Initial streamline location

Shaded area represents total specified mass flow rate

Portion of $\dot{m}$ in each streamtube remains the same from iteration to iteration

r_t

r_h

$\dot{m}$

a. Initial streamline location

r_t

r_h

$\dot{m}$

b. Adjusted streamline location

Figure A - 2 Illustration of streamline curvature solution approach

Boundary conditions for a traditional SLC application are shown in Figure A - 4. Typically, the grid extends far upstream and downstream so that the specification of inlet and exit curvature is not needed (curvatures are zero). Note that for the present application, inlet total pressure and total temperature were uniform from hub to tip, and there was no pre-swirl (inlet $V_\theta = 0$).
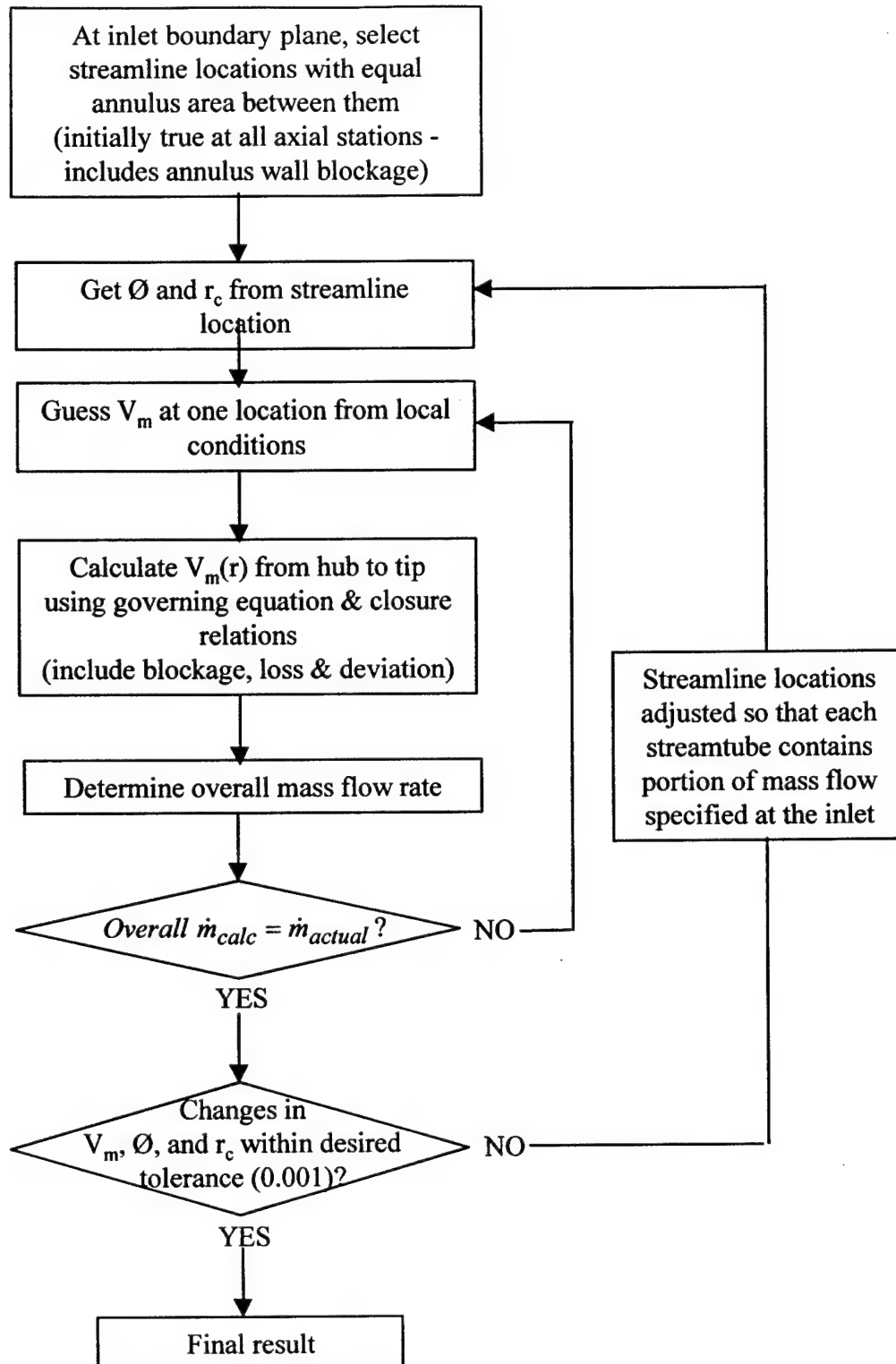
Figure A - 3 Streamline curvature solution procedure flow chart
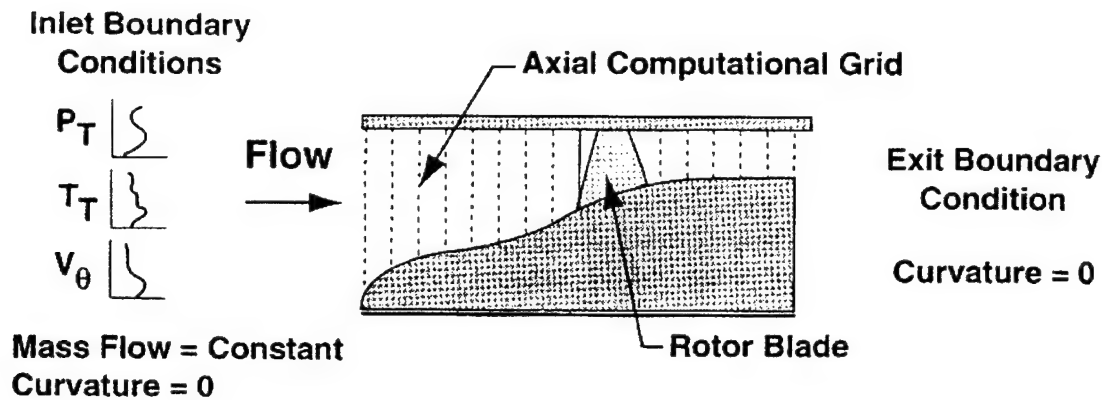
Figure A - 4 Traditional SLCC application – boundaries far upstream and downstream (Hale and O'Brien, 1998)

A2.1 Specific Correlations used to Obtain Closure Relations

The streamline curvature method necessitates the use of empirical/semi-empirical correlations to obtain closure, Equations (A-6) – (A-8). This section reviews the particular correlations used by the SLCC in the present work. Hearsey, 1994 and Klepper, 1998 describe the approach in detail. As implied by the closure equations and indicated in Figure A - 5, the correlations seek to define blade/vane section deviation angles and relative total pressure loss.

The SLC approach used here was developed by Hearsey, 1994, and involves three elements:

- Interpolation of blade definition on each streamline to determine cascade specifications.

- Interpolation of empirical cascade data to determine "reference" conditions.

- "Corrections" to these data to provide a total pressure loss coefficient and exit flow angle at each streamline section.

Blade definition includes blade row inlet and exit metal angles, blade sweep angles (as viewed in the r-z plane – see Figure A - 1), and lean angles (away from the radial direction
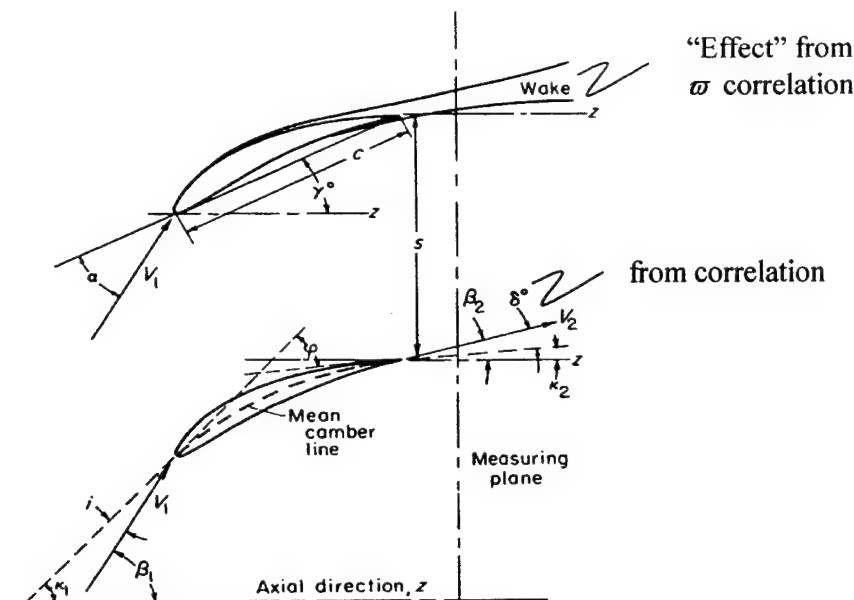
Figure A - 5 Blade section geometry specification with quantities obtained from correlations as indicated (NASA SP-36)

as viewed along the axis of the machine), solidity, maximum thickness, and location of maximum camber. The sweep and lean angles allow for the calculation of actual streamsurface sections (twisted) as opposed to cylindrical (or more correctly, conical) sections typically assumed.

In general, the correlations are based on low-speed, two-dimensional, cascade data from NACA 65-(A_{10})-series profiles (NASA SP-36, 1965). As noted by Dunham, 1996, the SP36 correlations are among the most widely known. These 2-D correlations provide low-speed, minimum-loss, *reference* conditions which are "corrected" to account for other blade profiles, 3-D, Mach number, and streamtube contraction effects, as well as operation at actual incidence. The 3-D effects are largely due to secondary and tip gap flows and their interactions with the throughflow.

Determination of a minimum-loss air inlet flow angle, β_{1ref}, is key to describing the low-speed reference conditions.

$$\beta_{1,ref} = \beta_{1,bl} + i_{ref}$$ (A - 9)

In Equation (A-9), $\beta_{1,bl}$ is the inlet metal angle, and i_{ref} represents the low-speed, minimum-loss reference incidence based on a 10% thick (t/c) NACA-65 cascade with corrections for other shape and thickness distributions and a linear variation of incidence angle with camber angle. This calculated $\beta_{1,ref}$ and other input geometry characteristics are the basis for many of the correlated curves used to determine the reference deviation and loss values. As mentioned, these are then corrected to account for 3-D effects, operation at actual incidence, etc.

Equations (A-10) and (A-11) show the final forms of the deviation and total pressure loss coefficient:

$$\delta = \delta_{ref} + \delta_{3D} + \delta_M + \delta_{va} + \delta_i$$ (A - 10)

where:

$$\delta_{ref} = \delta_0 + \frac{\theta}{\sigma^b}[m|_{\sigma=1.0} + 0.5(\frac{a}{c} - 0.5)]$$

$$\varpi = (\varpi_{min} + \varpi_M + \varpi_{tip} + \varpi_{hub})\left[1 + \left(\frac{i - i_{min}}{W}\right)^2\right]$$ (A - 11)

Equation (A-10) is recognized as a modification to the widely-used Carter's rule, $\delta = m\theta/\sigma^{0.5}$. The δ_0 represents the zero-camber, minimum-loss deviation for a 10% thick (t/c) NACA-65 cascade with corrections for other shape and thickness distributions. Parameter m is the slope of the variation in deviation with camber, θ, for a cascade of unity solidity. The solidity exponent b varies continuously from about 0.97 for axial inlet flow (β=0 deg) to 0.55 for β=70 degrees. As discussed by Cumpsty, 1989, pp. 170-171, the Lieblein correlation described

by δ_{ref}, Equation (A-10), typically predicts 1-2 degrees more deviation than Carter's rule, known to underpredict deviation by as much as two degrees.

The minimum relative total pressure loss coefficient, ϖ_{min} in Equation (A-11), provides an estimate of the blade profile loss (boundary layer and wake). As is common, the low-speed, minimum loss is correlated with diffusion factor, corrected for actual Reynolds number and trailing edge thickness (assuming fully turbulent boundary layer). The estimate is based on the work of Koch and Smith, 1976, still regarded as one of the more complete methods for treating profile loss (see for example, Casey, 1994; Cetin, et al, 1987).

The remainder of the terms in Equations (A-10) and (A-11) attempt to account for streamtube area change, 3-D, and Mach number effects, as well as operation at actual incidence. The polynomial term in Equation (A-11) is used to define the traditional "loss bucket" shape. In general, these corrections are empirical/semi-empirical formulations based upon data from NACA 65-series, British C-series, and DCA airfoil sections. An assessment of these formulations, as well as their applicability to modern blade profiles is provided in Chapter 3.

Appendix B. Bloch-Moeckel Shock Loss Model

The shock model implemented in the present work was based on the approach of Bloch, et al., 1999, 1996. They used the method of Moeckel, 1949, to develop a physics-based engineering shock loss model for *cascades* of arbitrary airfoil shape operating at design and off-design conditions. The model included an estimate for detached bow shock loss due to leading edge airfoil bluntness. This appendix briefly summarizes the method by highlighting some of the key features.

A fundamental difference in loss characteristics between a cascade and rotor is the smooth transition between "started" (choked) and "unstarted" (unchoked) operation for rotors. Figure B - 1 schematically shows this difference. Bloch suggests that for transonic designs, the mechanism for this smooth transition is downstream pressure information transmitted radially toward the hub through the casing boundary layer and region between the detached shock system and blade leading edge – both regions contain subsonic flow. Regardless of the mechanism, modeling this transition was not a problem for the present work as estimates for the minimum and choking incidences were already provided in the chosen streamline curvature method.

Transonic fan designs incorporate some finite leading edge radius for damage tolerance. Consequently, the bow shock is slightly detached and curved. Shown in Figure B - 2 is the approximation used by Moeckel, 1949. He assumed: (a) a hyperbolic shock which asymptotically approaches the freestream Mach lines, and (b) a straight sonic line between the shock and the body. With these assumptions, shock location (relative to the body sonic point, sb) becomes a single-valued function of upstream Mach number, with shock shape uniquely determined from blade LER and Mach number. In the present work, the following steps were

Figure B - 1 Cascade versus rotor loss characteristic (Bloch, 1996)

Figure B - 2 Moeckel method for detached shocks (Bloch, 1996)

164

taken to define the shock shape and location. Unless otherwise noted, equations were obtained from Bloch, 1996.

- The wedge angle for shock detachment, ε_{max}, was calculated from oblique shock theory (Equation B-2) using a closed-form relation to determine maximum shock angle, ψ_{max}, before detachment from the leading edge of a body (Equation B-1):

$$\cos 2\psi_{max} = \frac{1}{\gamma}\left[\left(\frac{\gamma+1}{2}-\cos 2\mu\right)-\sqrt{(\gamma+1)\left\{\left(\frac{\gamma+1}{2}-\cos 2\mu\right)^2+\frac{\gamma}{4}(3-\gamma)\right\}}\right] \qquad \text{(B-1)}$$

where:

$$\sin \mu = \frac{1}{\sqrt{M_{1s}}} \quad \text{and:} \quad M_{1s} \text{ is Mach number just upstream of shock}$$

$$\tan \varepsilon_{max} = 2\cot \psi_{max}\left[\frac{M_{1s}^2 \sin^2 \psi_{max}-1}{M_{1s}^2(\gamma+\cos 2\psi_{max})+2}\right] \qquad \text{(B-2)}$$

- Using Bloch's slight modification to Moeckel, the sonic point on the body, y_{sb}, was located at the tangency point for a wedge with half-angle one degree greater than ε_{max}.

$$y_{sb} = \frac{LER}{\cos\left(\varepsilon_{max}+1^\circ\right)} \qquad \text{(B-3)}$$

- The following closed-form, explicit relation was used to determine the shock angle which produces exactly sonic downstream flow:

$$\sin^2 \psi_s = \frac{1}{2\gamma}\left[\left(\frac{\gamma-3}{2M_{1s}^2}+\frac{\gamma+1}{2}\right)+\sqrt{\frac{4\gamma}{M_{1s}^4}+\left(\frac{\gamma-3}{2M_{1s}^2}+\frac{\gamma+1}{2}\right)^2}\right] \qquad \text{(B-4)}$$

- To locate the sonic point, s, on the shock, a simplified form of the continuity equation was applied on fluid passing between the vertex and s. Assuming the sonic line inclined at wedge angle, ε_s, and choosing the mass centroid of the flow as representative provided the following relation:

$$\frac{y_s}{y_{sb}} = \frac{1}{1 - \left(\dfrac{P_{01}}{P_{0s}}\right)_c \sigma \cos \varepsilon_s} \qquad (B - 5)$$

where:

-- the total pressure loss in (B-5) is computed from oblique shock theory (i.e., Equation (4-4) with SA=ψ_c). Note that the shock angle at the centroid, ψ_c, was found from:

$$\tan \psi_c = \frac{\sqrt{4\left(M_{1s}^2 - 1\right)\tan^2 \psi_s - 3}}{\sqrt{M_{1s}^2 - 1}} \qquad (B - 6)$$

Equation (B-6) was obtained through application of the assumed hyperbolic function given below on the centroid location, $y_s/2$, and slope of the shock wave, dy/dx:

$$y = \frac{\sqrt{x^2 - x_0^2}}{\sqrt{M_{1s}^2 - 1}} \qquad (B - 7)$$

-- σ is the area contraction ratio required to isentropically decelerate M_{1s} to sonic velocity. It was obtained from simple, compressible relations; i.e., A/A^*.

-- the wedge angle at the sonic point, ε_s, was calculated from Equation (B-2) with $\psi = \psi_s$.

- Finally, from the slope of the shock wave and hyperbolic form (B-7), the location of the shock vertex was given by:

$$\frac{x_0}{y_{sb}} = \sqrt{M_{1s}^2 - 1}\left(\frac{y_s}{y_{sb}}\right)\sqrt{\left(M_{1s}^2 - 1\right)\tan^2 \psi_s - 1} \qquad (B - 8)$$

166

With shock shape and location specified, an estimate for total pressure loss due to the detached bow portion of the shock was obtained, again following the approach of Bloch, 1996. Fluid entering a blade passage will cross an infinite number of bow waves from adjacent blades. As illustrated in Figure B - 3, property changes experienced by fluid crossing between points 1'' and 2''' are identical to those produced crossing between 1''' and 2''''. Thus, the loss produced by all the bow waves can be estimated by integrating the loss from a single wave between the stagnation point, B, and "infinity." The total pressure drop was estimated from:

$$\frac{P_{0A}}{P_{01}} = 1 - \frac{\int_0^\infty \left(1 - \frac{P_{02}}{P_{01}}\right) dy}{\int_0^s dy} \qquad \text{(B - 9}$$

where P_{02}/P_{01} was obtained from oblique shock theory (Equation 4-4) applied locally as the integration proceeds. The increment and upper bound of the numerical integration were selected so that the accuracy of the bow shock loss estimate was well within the accuracy of the overall shock loss prediction, discussed further in Chapters 4 and 5.
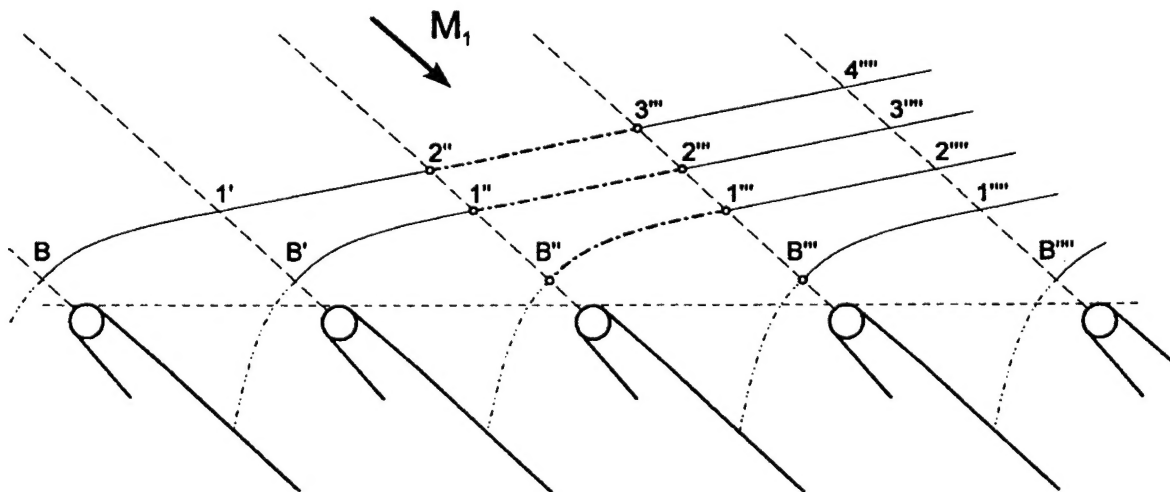
Figure B - 3 Wave pattern caused by blunt leading edges on an infinite cascade with subsonic axial velocity (Bloch, 1996)

Vita

Keith Michael Boyer was born in Utica, New York on February 21, 1961. He spent the first eighteen years of his life in Utica under the watchful eyes of his parents, Kenneth and Loretta Boyer. On August 21, 1979, he began his career in the United States Air Force (USAF) by arriving for boot camp at Lackland AFB, San Antonio, Texas. He spent five years as an electronic warfare (EW) systems specialist. While serving as an EW instructor at Keesler AFB, Mississippi, he was selected for the Airman Education and Commissioning Program in 1984. He graduated cum laude from the University of Florida in May 1987 with a bachelor's degree in Aerospace Engineering and was commissioned that same year through the Officer Training School (OTS). He was a distinguished graduate from the OTS and the Air Force Institute of Technology (AFIT), earning a master's degree in Aeronautical Engineering in 1992.

Major Boyer has fourteen years of propulsion-related experience as a test and analysis engineer, project manager, Assistant Professor of Aeronautics, and systems engineering and logistics manager. He is a Certified Acquisition Professional with Level II certification in Systems Planning, Research, Development and Engineering and Level I in Test and Evaluation and Program Management. His major awards include the Meritorious Service Medal, Air Force Commendation Medal (four times), Excellence in Technical Engineering & Management Award, Outstanding First Year Instructor (Department of Aeronautics, USAF Academy), Best Thesis-Fluid Dynamics, Best GPA (Department of Aeronautics, AFIT), and the Heron Award for most significant in-house research (Aero Propulsion and Power Directorate).

Major Boyer and his wife, Joyce, have two daughters, Jennifer, 16, and Kelly, 12. Upon completion of his Ph.D., he and his family will be returning to Colorado Springs, Colorado, where he will teach in the Department of Aeronautics at the USAF Academy.